Thermally Enhanced Paper Microfluidics for Photonic Crystal Biosensors in Amorphous Silicon

Joshua S. Male BSc

Master of Science by Research

University of York

Physics

September 2019

Abstract

Paper-based lateral flow devices (LFDs) are the technology behind low-cost, rapid, simple and portable point of care devices capable of displaying results within minutes. Targeted lateral flow devices are widely used for medical and environmental analyte detection but typically suffer in quantifying a detection. Paper-based LFDs are volume limited due to an upper-absorption limit but present a more environmentally friendly alternative to polydimethylsiloxane-based microfluidic alternatives. Photonic crystal biosensors are a valuable tool for label-free biosensing. Combining a paper-based lateral flow device with a photonic crystal biosensor allows for quantified analyte concentration measurements using guided-mode, or leaky-mode, resonance to measure a refractive index change at the photonic crystal's surface.

The primary challenge with any form of biosensor is the limit of detection. The photonic crystal biosensors reported in this work have a limit of detection of 10µg/mL. To reduce this limit of detection, without altering the performance of the sensor, we utilise two effects. Firstly, a thermal gradient across the paper LFD to accentuate a phenomenon known as the coffee-ring effect, which causes an outward flow of solute as a body of solution dries. Secondly, the physical design of the paper LFD and the resulting flow-manipulation of the analyte.

The system we propose consists of a paper-based lateral flow device acting as a power-free pumping system, in which a thermal gradient is created using a targeted heat source to increase analyte localisation to reduce the limit of detection of a photonic crystal biosensor. Through optical measurements in reflection with a temperature gradient of 30˚C, we were able to reduce the limit of detection of a 2D photonic crystal to 6ng/mL. This result is a factor 10^3 lower than previously reported detection limits.

Contents

List of Tables

List of Equations

List of Figures

Acknowledgements

Firstly, I would like to thank my supervisor, Professor Thomas Krauss, for the support and advice he has given me not just over the process of this work but for the last two years I have worked with him. There have been many ups and downs throughout this work and Thomas has always pushed me to be better and to keep going.

Other members of the photonic research group at the University of York requiring individual acknowledgements are: Dr Christopher Reardon and Dr Matthew Simmons for the opportunity to work on such a project and their advice and assistance, Dr Donato Conteduca for his work with nanohole arrays, Alex Drayton for assistance with 3D-printing techniques and George Duffett for advice with sputtering and other cleanroom-based fabrication steps.

Rarely does anyone achieve anything by themselves, some of the work in this thesis was conducted as part of a Bachelor of Science final-year project alongside Laurence Grant and Jamie Conway. I would like to thank both for their hard work throughout.

Just in case I have missed anyone, I would like to thank the remainder of the photonics research group at the University of York. The Masters by Research program has not been easy, and I would like to thank you all for any advice, thoughts or even just a distraction over a coffee.

Of course, I would also like to thank those who have helped throughout my education, particularly throughout my Bachelor of Science degree. My family and friends outside of the University also deserve a big thank you.

Ending the acknowledgements, I would like to thank my wonderful fiancé Tasha for her endless support through the tough times when an experiment fails or there appears to be nowhere to turn.

Author's Declaration

I, Joshua Male, declare that this thesis is a presentation of original work and I am the sole author. This work has not previously been presented for an award at this, or any other, University. All sources are acknowledged as References.

For the most part, the work in this thesis has not been previously submitted for a degree or any other qualification at this, or any other, University. There are aspects of Chapter 2 which have previously been worked on and, in some instances, included in the presentation of a Bachelor of Science dissertation. This includes any work completed on the microheaters and some of the paper-channel development covered in chapter 2. This thesis serves as an extension/development on achievements made on my Bachelor of Science degree at the University of York and it, therefore, seems relevant to include them as a development stage as there are no published records of these achievements.

Where I have included the published work of others, I have made it clear to give the relevant references to the correct referencing standard and all referenced work is listed in the Bibliography chapter of this thesis. Where I have collaborated with other researchers at the University of York, I have given acknowledgements either in the main body of the text or in the acknowledgements section of this thesis.

There are no relevant published papers or conference papers to include for this thesis.

The data is the data

1. Introduction

1.1 Background and Motivation

Rapid diagnosis of a disease early in its development is critical for providing effective treatment. The earlier the disease is in its development, the lower the concentration of relevant biomarkers that need to be detected. So far, very sensitive detection techniques are confined to the laboratory, which limits accessibility to patients, especially in resource-limited locations [1]. The development of simple devices to rapidly perform reliable diagnostic testing, known as point-of-care (POC) devices, provides a means of rapid initial screening in non-laboratory settings [2]. The need for such devices extends beyond rapid medical screening to food quality and environmental testing [3,4]. POC device development relies on simple operation and inexpensive consumer/development cost, but a key requirement is that they achieve high sensitivity. The purpose of this project is to investigate a simple paper-based method to increase the concentration of the analyte prior to the measurement, known as preconcentration of the analyte, with the goal of reducing the limit of detection of the sensor.

1.1.1 Microfluidics

Microfluidics refers to the engineered manipulation of fluids on the microscale level and more commonly refers to devices with dimensions less than 1mm. At the microscale, microfluidics benefits from rapid diffusion [5], laminar flow [6] and a large surface area to volume ratio [7]. Microfluidics more specifically refers to structures fabricated with soft lithography in polydimethylsiloxane (PDMS) [8]. Other fabrication techniques include the use of laminates, nanoimprint lithography and 3D printing [9].

Lateral flow devices (LFDs) are the technology behind low-cost, rapid, simple and portable devices, thus providing the ideal platform for a POC device. The LFD is a paper-based platform for the detection of analytes in solution. Samples are introduced to the LFD and results are typically displayed within minutes. Targeted lateral-flow-based assays are widely used for the quantitative and qualitative detection of analytes, such as antibodies [10], and can be used with a wide variety of samples, such as urine [11], saliva [12] and blood [13]. Lateral flow devices used with bio-recognition molecules are known at lateral flow assays. The principle behind LFAs is straightforward, a liquid sample containing an analyte of interest is introduced and moves without assistance from external forces, relying solely on capillary action. Bio-recognition molecules, attached to the substrate, can interact with the analyte and an appropriate response is given in a detection zone.

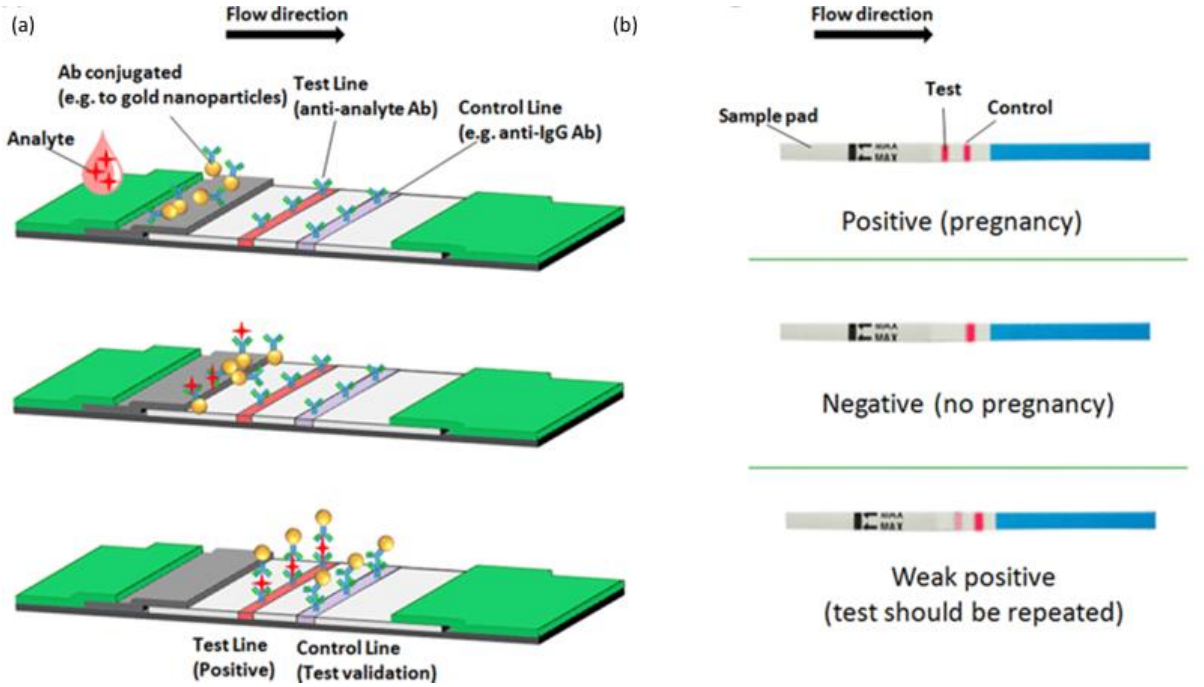

Figure 1.1: *Typical configuration and operation of a lateral flow immunoassay test strip.*

(a) Representation of the assay's mechanism. (b) Most commonly used LFA, the pregnancy test. [© Lifescience Dynamics]

A typical LFA, as shown in figure 1.1(a), consists of overlapping membranes mounted on a backing card for greater stability as is commonly found in a pregnancy test, shown in figure 1.1(b). The liquid sample is applied at one end of the strip, known as the sample pad, which ensures that the sample will be capable of binding to the capture reagents of conjugates and on the membrane. The sample then flows through the conjugate release pad, which contains antibodies specific to the target analyte. At this stage, it is common for the analytes to be conjugated to coloured or fluorescent particles. The sample and conjugated antibody bound to the target analyte flow to the detection zone, which contains specific biological components, such as antibodies or antigens, immobilised in lines and reacting with the bound analyte. Analyte recognition results in an appropriate response at the test line, while the control line shows the proper liquid flow through the system. The results can be validated by eye or through a dedicated detector. To maintain sample flow, an absorbent pad sits at the end of the strip to wick excess reagents and to prevent back flow due to a greater absorption volume than the other test strip components [14].

Many LFAs are designed for, and achieve, cheap and rapid POC tests suitable for primary screening both in industrial and medical settings. The visual result is clear and easily distinguished, providing a qualitative result for the presence of a target analyte. It is more difficult for LFAs to achieve quantitative results, as they mainly provide Yes/No information. Paper-based systems are often more complex to design than conventional microfluidics when it comes to multi-channel systems, or patterning channels. However, paper-based systems for single channel analysis are preferable for POC devices as they don't require any external pumping systems and are more easily stored and transported as they are not fragile unlike some glass fluidic systems. Paper is also more environmentally friendly than its counterparts consisting of PDMS, glass or plastic [15]

1.1.2 Biosensing

Sensors are typically categorised as either physical or chemical, determined by their likeness to human senses. Physical sensors respond to audio waves, electromagnetic radiation or pressure (hearing, seeing and feeling respectively), whereas chemical sensors respond to chemical stimuli such as odour or palate flavour of molecules (taste and smell) [16,17]. There are various subcategories of sensors including magnetic [18], optical [19], radiation [20], electrical [21], and electrochemical [22] to name a few, which are distinguished by their mode of reception, application, detectable analytes and measuring method. A sensor can be understood as a transducer, which translates the physical or chemical stimulus into a readout, usually in electronic form [23].

A biosensor is a hybrid of physical and chemical sensing that measures biological or chemical reactions through the generation of a signal proportional to the concentration of an analyte in the reaction. Biosensors use an analyte, which is a liquid that contains some substance of interest that needs detection, and which could be as simple as sugar in a water-based solution. Biosensors usually employ biorecognition molecules to achieve specificity, such as aptamers or antibodies that specifically bind to the molecule of interest. When binding occurs, the biosensor transduces the bio-recognition event into some measurable signal. Following bio-recognition detection, the signal is nowadays displayed in some electronic form for user analysis and interpretation.

1.1.3 Optical Biosensing

Optical biosensors use light as the key part of the transduction mechanism. Optical biosensors have a wide range of applications including biomedical research, environmental monitoring and healthcare [24]. Detection protocols can be classified as labelled and label-free. In the labelled approach, a fluorophore is typically attached to the molecule of interest which acts as an amplifier. Fluorescence-based detection is capable of single molecule detection but is more difficult to implement and therefore usually laboratory-based. For POC applications, the label-free approach is usually preferred, which is easier to implement. In contrast, the label-free approach relies on a direct interaction between the light and the molecule and allows for quantitative measurement of molecular interaction. Label-free detection mechanisms measure a change in refractive index induced by bio-recognition analyte interactions, which is directly related to the density of bound molecules [25]. A photonic crystal (PhC) is often used for refractive-index-based biosensing, as the resonance of the PhC yields strong evanescent electric fields that enter the sensing region. A shift of RI in the sensing region associated with bio-recognition analyte interactions is probed by the evanescent field, resulting in a shift in the resonant wavelength of the PhC [26] which is then detected by a spectrometer. Because label-free approaches tend to be less sensitive than labelled ones, looking for other mechanisms to enhance sensitivity such as preconcentration is important.

1.2 Photonic Crystal Biosensors

The following section provides a brief overview of photonic crystal used as a biosensor. The focus of the work is on the use of a heating element to provide a thermal preconcentration, thereby improving the limit of detection of the sensor. The performance of a photonic crystal biosensor depends on many factors, some of which are outside the scope of this thesis. The main feature to consider for a figure of merit (FOM) is the sensitivity of the PhC, which is defined as the ratio between the change in sensor response and the change in the measured value. Typically, this is given as the wavelength change, $\Delta\lambda$, and the change in refractive index, Δn. Hence, the sensitivity is a measurement of wavelength shift per refractive index unit (nm/RIU). The sensitivity is found by measuring the resonant wavelength for solutions of known refractive index and taking the gradient of the resulting graph.

The other feature to consider for a FOM is the minimum detectable wavelength shift, which is directly proportional to the sharpness of the peak, known as the Q factor. The Q factor is the ratio between the peak's centre wavelength and its full width at half maximum (FWHM). It has been shown that the PhC noise σ is inversely proportional to the peak linewidth $\Delta\lambda$, which means that the minimum detectable shift is inversely proportional to the Q factor [27].

The two sources of noise associated with this sensing modality is the intensity and wavelength noise [27,28], which arise from the photodetector noise, fluctuations in the light source intensity and temperature fluctuations in the temperature of the PhC (wavelength noise). A sharper Q factor is more affected by wavelength noise and requires very precise spectrometers.

The sensitivity measurements mentioned here refer to the bulk sensitivity of the PhC, which is a measure of the PhC response to changes in the entire cover medium. For the purpose of this thesis, it is more relevant to consider bulk sensitivity rather than surface sensitivity. The surface sensitivity refers to the measurement of molecular binding on the PhC surface. For similar 2D PhC S.Pal et al. [29,30] have achieved a bulk sensitivity of 64.5nm/RIU, with a limit of detection of 10µg/mL. Similarly, D.Conteduca et al. reports a limit of detection of 10pg/mL [31] for a 2D PhC in hydrogenated amorphous silicon.

1.3 Scope of the Thesis

The main goal of this work is to design and create a cheap and simple point of care device for the purpose of detecting the presence of- and measuring the quantity of- analytes. In order to achieve this, I will combine a paper-based lateral flow device (to act as a pumping mechanism), a photonic crystal biosensor (to measure the analytes) and a localised heat source to generate a thermal preconcentration.

Paper-based LFDs (without functionalisation) can also be used for analytes that do not require a bio-recognition molecule to be detected and measured. Accordingly, we used a paper channel LFD to act as a powerless pumping system, which allows for the detection and measurement of a solution whereby we measure the local refractive index in the detection area above the surface of the sensor.

The photonic crystal used as the sensor element is realised as a nanohole array, which consists of a square array of nanoscale holes within a dielectric. The nanohole array is fabricated using electron beam lithography and the dielectric in question is hydrogenated amorphous silicon (a-Si:H). The a-Si:H needs to be thin (~100-150nm) to allow for leaky mode resonance within the photonic crystal. To deposit material of this thickness, we use pulsed DC magnetron sputtering. To implement the sample heating, I initially made heating tracks lithographically; this approach turned out to be far more complicated than anticipated, so was abandoned. I then conceived the idea of adopting Kanthal mesh (of e-cigarette fame) and superimposing it onto the sensor, which was implemented successfully.

The effectiveness of the heating element was observed using red food dye over a series of experiments to determine the best achievable system design. I then moved on to salt and sugar solutions and was able to demonstrate preconcentration effects. I also tried protein solutions with antibodies but was not successful.

2. Manipulating Concentration of Analytes

2.1 Introduction

It is commonly observed that a droplet of liquid containing a solute, such as coffee, does not leave a uniform spot of solute when drying; instead, a ring and a gradient towards the droplet centre is observed. Deegan et al. [32] first explained that the ring is produced as solvent lost to evaporation is replenished from the centre thus carrying solute outwards. Chapter 2 will focus on this effect and how it can be targeted through substrate manipulation and temperature gradients to enhance analyte concentration over a sensor and correspondingly enhance detection sensitivity.

2.2 Initial System Design

The starting point for our system is shown in figure 2.1. It includes a paper substrate, a photonic crystal biosensor and the liquid analyte. The paper substrate acts as a pumping system based on wicking action and typically, a paper test strip used in this manner is known as a lateral flow device (LFD).

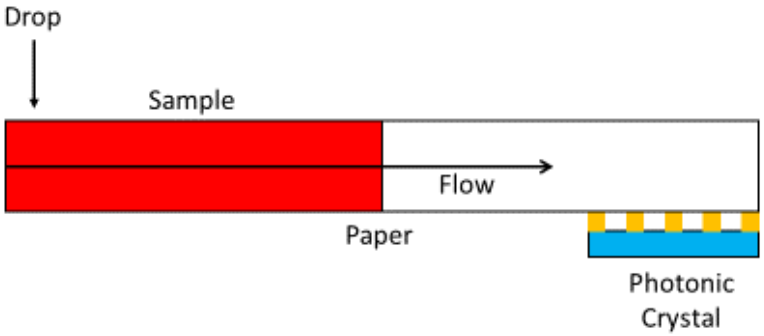

Figure 2.1: *Initial experimental setup*

The wicking action of the paper is based on capillary forces, as paper is a porous material that readily absorbs liquid due to its cellulose composition. Capillary action is the ability of a liquid to flow without the assistance of, or sometimes in opposition to, external forces like gravity. It requires the adhesive forces between substrate and liquid to be greater than the cohesive forces (or surface tension) maintaining the fluid body. A dry porous material absorbs a liquid with a rate that decreases over time as the material becomes saturated[33].

Absorption in porous mediums is governed by two properties, the sorptivity and capillarity of the medium. Sorptivity is a measure of absorption and exposure time, given in equation 2.1, it

may be more relevant to measure the distance of water uptake (x) with respect to exposure time (t), which is represented by the capillary coefficient (k), given in equation 2.2[34,35].

$$S = \frac{I}{\sqrt{t}} = \frac{V}{A\sqrt{t}}$$

Equation 2.1: *Sorptivity coefficient*

$$k = \frac{x}{\sqrt{t}}$$

Equation 2.2: *Capillary coefficient*

Both S and k can otherwise be represented as shown in equation 2.5 and 2.6, which are derived from Darcy's Law[36] and a derived equation for the volume of water flux in a porous medium[35], given equation 2.3 and 2.4 respectively.

$$V_F = \frac{r^2 \Delta P}{8\eta x}$$

Equation 2.3: *Darcy's Law*

$$q = \pi r^2 x = \pi r^2 \sqrt{\left(\frac{r\gamma}{2\eta}\right)\cos(\theta)}\sqrt{t}$$

Equation 2.4*: Volumetric water flux*

$$k = \sqrt{\frac{r\gamma}{2\eta}\cos(\theta)}$$

Equation 2.5: *Capillary coefficient equation*

$$S = \gamma k$$

Equation 2.6: *Sorptivity coefficient equation*

Where V_F is the water flow velocity, r is the capillary pore radius, ΔP is the pressure difference across the capillary, η is the viscosity of the liquid, x is the capillary pore length, q is the volumetric water flux, γ is the liquid surface tension, θ is the capillary-liquid contact angle, t is the time at which a measurement is taken (exposure time), S and k are the sorptivity and capillary coefficients as defined in equation 2.1 and 2.2 respectively. For our system we can assume a contact angle of θ=0˚, and thus a cos(θ) term of 1.

It is apparent from equations 2.5 and 2.6 that the paper absorption and liquid uptake is largely dominated by the surface tension of the liquid (γ), which is governed by the cohesion of the liquid molecules. The solutions used in this work are water-based, providing a relatively high surface tension due to a large tensile strength in water molecules caused by the energy stored within hydrogen bonds[37]. To overcome this issue, we need to ensure the pore radius of the paper is sufficiently large to break the surface tension of the water.

In paper chromatography, which requires similar substrate conditions, hydrophobic barriers are created using ink-jet printed wax strips to restrict liquid flow. During preliminary experiments using wax to create such a hydrophobic barrier, I regularly observed leakage as shown in figure 2.2(a), which shows that creating a barrier is more difficult than anticipated. Instead, I decided

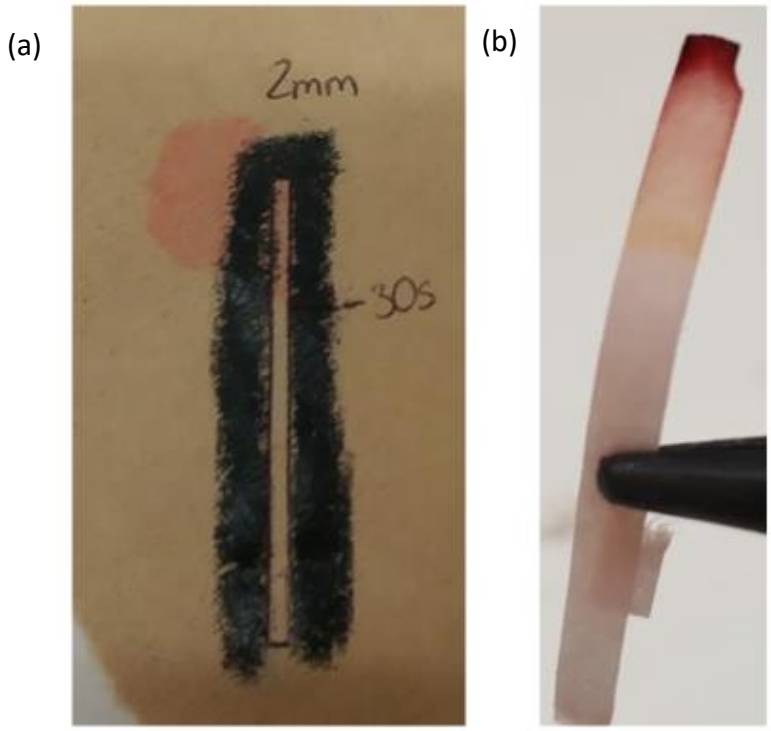

Figure 2.2: *Hydrophilic channel creation*

(a) Wax hydrophobic barrier creating paper channel. Sample applied with pipette. Sample leaking observed at weak point in wax barrier. (b) Channel produced by simple cutting.

to create a channel simply by cutting to contain the liquid in a narrow paper strip, shown in figure 2.2(b). The absorption volume is then restricted by the length and area of the paper substrate. A dye was added to the water applied to the strip and heated at the top end to enhance evaporation, like the coffee ring effect.

2.3 The Coffee Ring Effect

A phenomenon known as the coffee ring effect (CRE) occurs when a liquid droplet containing a solute evaporates. Since evaporation scales as the surface-to-volume ratio, it proceeds faster at the edge of droplet, thus creating gradient between the outer edge and the droplet centre. The differential evaporation then drives the liquid towards the outside of the droplet, increasing the concentration of solute [32]. The CRE is illustrated in figure 2.3 [38].

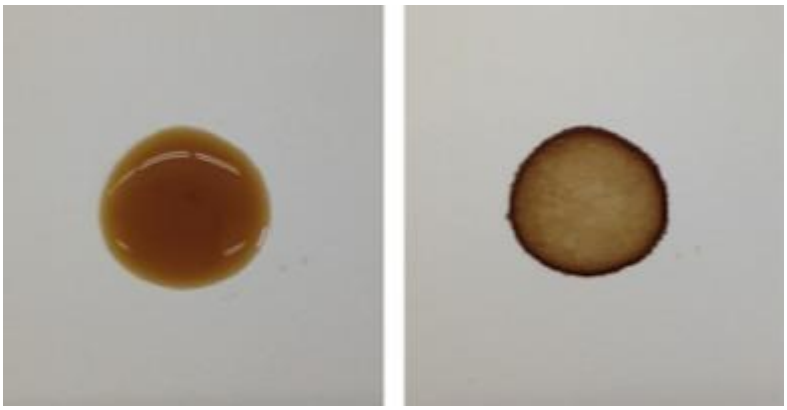

Figure 2.3: *Coffee ring effect*

(a) Coffee droplet, (b) Dried droplet showing the solute gradient towards the droplet edge.

The CRE can be enhanced by external heating to further increase the evaporation rate; this will increase the local concentration of the analyte thereby offering the possibility of improving the limit of detection of a biosensor placed in the area of increased concentration.

(a) (b)

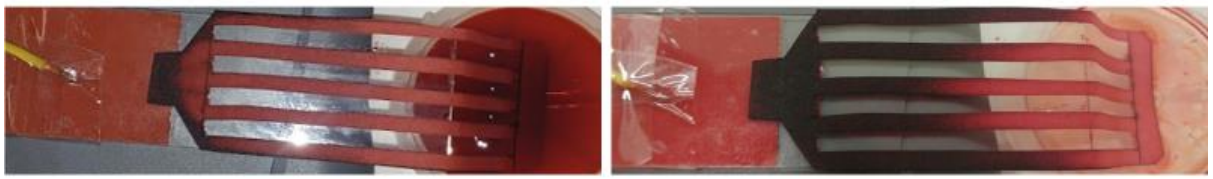

Figure 2.4: *Targeted coffee ring effect with red food dye reservoir.*

(a) Flow in progress, heater switched on, concentration beginning to build. (b) All solution used, heater switched off, and large concentration gradient established. This work was conducted in the context of my BSc project and it serves as the motivation for the present MSc research.

By placing a heat source at one end of the paper strip, using insulating materials and allowing the system to operate in an open environment, the CRE can be greatly enhanced. Figure 2.4 shows a first version of the proposed system consisting of a large paper channel array, a resistive heat source used with food dye and water as the analyte for visual confirmation.

2.3.1 System Update I

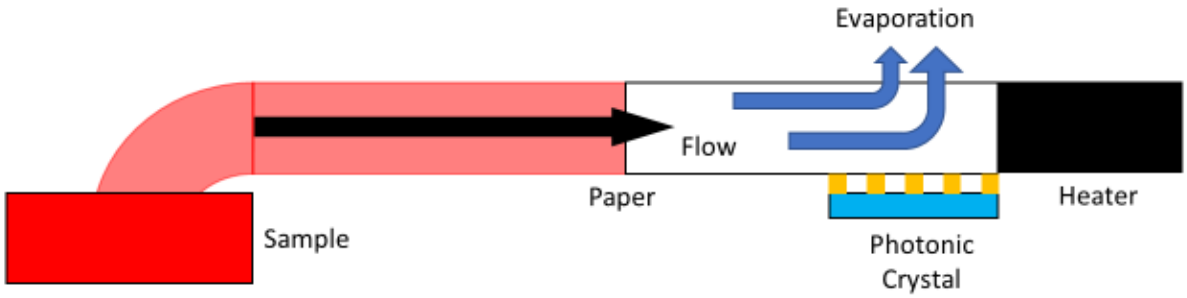

Figure 2.5: *System update I*

System development featuring a sample reservoir, from which the paper draws the sample solution through capillary action, and a heat source to create solvent evaporation.

The next stage of development is to add the photonic crystal sensor to the system, shown in figure 2.5, and optimise the localisation of the heat source to concentrate analytes in the observable region only. We will also switch to testing the photonic crystal (PhC) with a colourless solution and measure the concentration as a refractive index change.

The process is covered more in chapter 4, but a brief overview of the process is given here. The PhC biosensor is illuminated with a white light source and a reflection spectrum is measured. Due to the periodic nature of the PhC, a resonant wavelength is observed which corresponds to the local refractive index (RI) above the surface. The local RI is affected by the concentration of analytes, hence increasing the analyte concentration shifts the resonant wavelength. Paper delivery and thermal concentration of analytes used in this fashion is a unique method and has the potential to compete with microfluidic systems due to a lower limit of detection created by a thermal preconcentration.

2.3.2 Protein Denaturation

While there are a range of analytes that may benefit from CRE-like preconcentration, the ultimate goal of the project is to enhance the detection of proteins. Therefore, the system needs to be compatible with proteins, especially in terms of temperature. Protein molecules are highly specific in structure, as each protein performs a specific task within a living system. When the three-dimensional structure of the protein is disrupted, it loses its functionality, a process known as denaturation. If a solution containing proteins is heated, it will reach a temperature analogous to that of melting a solid. The melting points for different proteins varies, but generally, a temperature above 41˚C means that many proteins will lose their shape, thus denature [39].

Therefore, the heating element used in the system needs to be capable of maintaining a steady state temperature at the paper/photonic crystal boundary of 35-38˚C to allow for minor fluctuations and to ensure that the proteins do not denature. The temperature can be set higher, e.g. if the analyte is saltwater or sugar solution, but temperatures near 100˚C or above should also be avoided, as the solvent needs to evaporate steadily. After some initial testing, I established the most suitable operating temperature range of 35-60˚C.

2.4 Targeted Heating of Analytes

2.4.1 Joule Heating

Joule, or resistive, heating is the process where an electric current is converted to heat as it flows through a resistor and is describe by Joule's first law, shown in equation 2.7.

$$Q = I^2Rt$$

Equation 2.7: *Joule's first law*

Where Q is the amount of heat energy produced, I is the electric current, R is the electric resistance, and t is the length of time this happens for. When the electric current flows through a solid with finite conductivity, the electrical energy is converted, through collisions between the conductor's electrons and atoms, to thermal energy [40]. The resistance (R) of a circuit component is given by Ohm's law, equation 2.8.

$$R = \frac{V}{I}$$

Equation 2.8: *Ohm's law*

If that component is an electrical wire, then the resistance is proportional to the length (L) of the wire and inversely proportional to its cross-sectional area (A), as shown equation 2.9. The resistivity (ρ) of a material is a factor of resistance that accounts for the material properties, including temperature dependent properties [41].

$$R = \frac{\rho L}{A}$$

Equation 2.9: *Resistivity*

Resistance of a current carrying wire is proportional to temperature due to the dimension change that occurs as temperature varies. A material constant known as the temperature coefficient of resistance (α) represents the change in resistance per degree of temperature [40], given in equation 2.10.

$$R = R_0[1 + \alpha(T - T_0)]$$

Equation 2.10*: Resistance and temperature*

Where R_0 and T_0 are resistance and temperature of the conductor at 20˚C. The application of these equations to my heater design is discussed in the next section.

2.4.2 Microheaters

The first idea was to produce the microheaters lithographically, i.e. to place them directly onto the sensor chip, which seems most practical, as all the elements can be combined monolithically, and the heated volume can be minimised given the small size of the sensor chip. The sensors, discussed in chapter 4, are fabricated as a 1mm^2 structure and the proposed sensor-heater arrangement is sketched in figure 2.6.

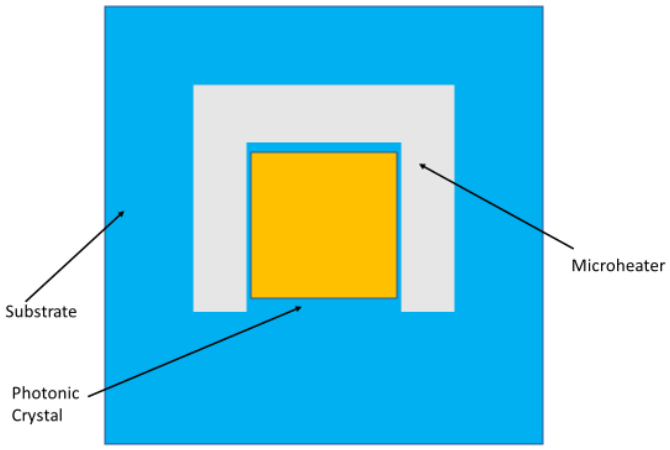

Figure 2.6: *Photonic crystal with microheater element on glass*

The idea is to produce the heat in close proximity to the sensor chip with the assumption that the liquid within the "horseshoe" of the heater is heated uniformly, thus creating the CRE above the sensor element. The microheaters consist of a wire track made of a metal with low conductivity such as Nickel or Aluminium. Combining equations 2.8 to 2.10 to determine the dimensions of the microheater for a given temperature yields equation 2.11.

$$L = \frac{V^2 A}{P\rho_0\left(1 + \alpha(T - T_0)\right)}$$

Equation 2.11: *Conductor length*

To design the microheaters using in this body of work, I used the following parameters. For nichrome I used the literature value for resistivity, $\rho_0 = 7\text{x}10^{-8}\Omega\text{m}$, and for coefficient of thermal expansion, $\alpha = 13.3\text{x}10^{-6}\text{K}^{-1}$ [42]. I chose to use a D battery as my power source, which has a voltage output, V = 1.5V [43], and a power output, P = 0.001W. For a maximum temperature change ($T - T_0$) of 40˚C, where T_0 is given as 20˚C, I used equation 2.8 to calculate a track length of 30.6mm. I chose this maximum operating temperature (60˚C) to be above the maximum temperature for use with proteins as discussed in section 2.3.2.

Heat is generated in the microheater and transferred through the substrate through conduction. Thermal conduction is the transfer of energy between adjacent molecules or electrons in a conducting medium. The rate of heat flow is proportional to the cross-sectional area of the medium and inversely proportional to the length of the medium, shown equation 2.12.

$$q = -k\nabla T$$

***Equation 2.12**: Thermal conduction*

Where q is the heat flux, k is the medium's conductivity and ∇T is the temperature gradient across the medium [40]. Effectively equation 2.12 means that for a medium with low conductivity, such as silica (k = 0.02), paper (k = 0.05) and water (k = 0.606) [44], the rate of heat transfer is slow. A low rate of heat transfer only affects the initial thermal ramp, hence a higher ΔT is required in the initial ramp phase to bring the silica, paper and water-based solution up to operating temperature.

Once the system is up to temperature, the input power is adjusted to be equal to the energy out. The energy out is given as the transfer of internal energy as electromagnetic waves, known as heat radiation. Thermal radiation is governed by the Stefan-Boltzmann law shown in equation 2.13.

$$P = \varepsilon\sigma A(T^4 - T_0^4)$$

***Equation 2.13**: Thermal radiation*

Where P is the net heat flow out of the system, ε is the emissivity of the medium which is a measure of a material's ability to emit or absorb thermal radiation (0-1), σ is the Stefan constant, A is the surface area of the medium emitting or absorbing and T and T_0 are the absolute temperature of the object and the environment respectively [40]. Silica (ε = 0.77), water (ε = 0.95), and paper (ε = 0.93) have relatively high emissivity values [45], which means that our system relatively easily absorbs and emits thermal energy.

Combining equation 2.11 and 2.12 leads to a system that requires a large amount of thermal energy to reach a desired temperature, but easily transfers that thermal energy between components. The radiated power, and therefore the required thermal power output of the microheater, is largely governed by the temperature difference between the environment and the system. A metal with a high emissivity is needed, therefore, to efficiently transfer electrical energy into thermal energy to maintain a steady state system.

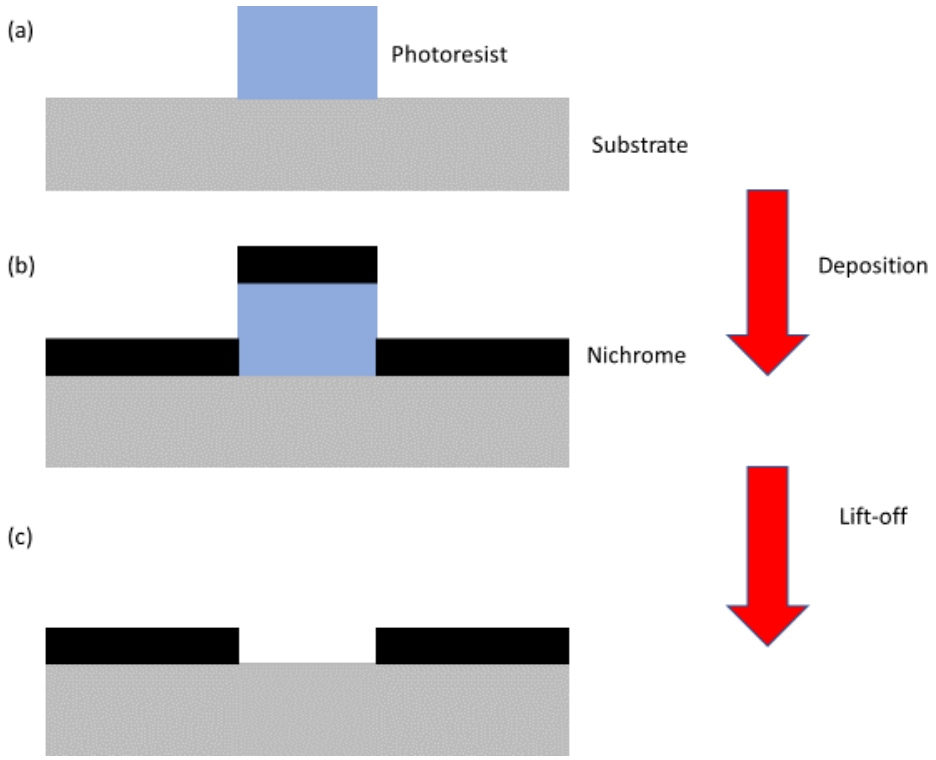

Figure 2.7: *Electron beam lithography and lift-off*

(a) Electron beam lithography is used to create a desired pattern in photoresist on a substrate. (b) Nichrome, or other material, is deposited using evaporation or sputtering. (c) The photoresist is removed leaving desired material in created shape.

Microheater designs were created using computer aided design (CAD) software and produced using electron beam lithography. Electron beam lithography is the process of patterning a target material using a sacrificial layer of resist, a process described in more detail in chapter 4. The conducting material used for making the wire tracks is then deposited using a lift-off process, shown in figure 2.7 [46].

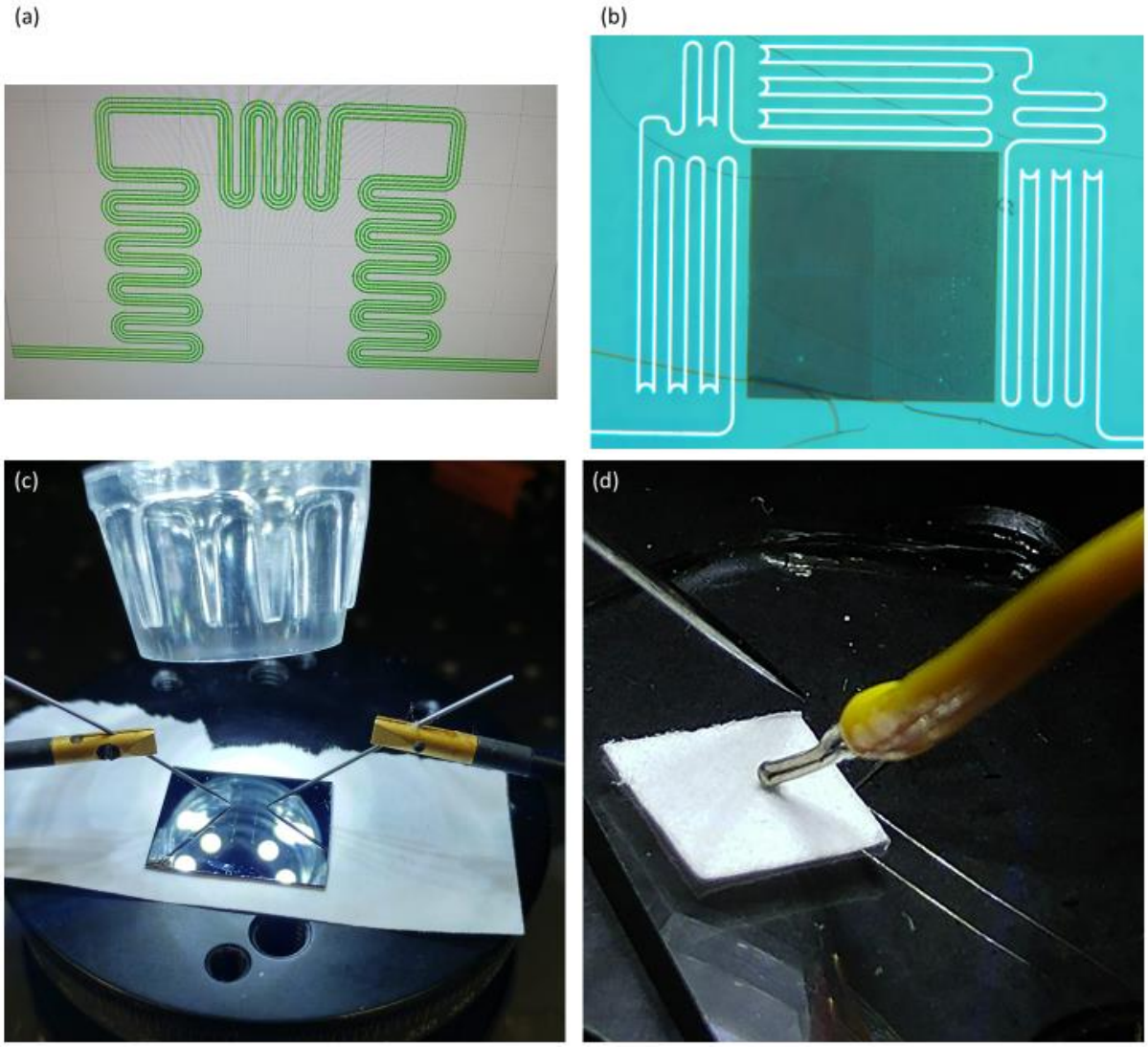

Figure 2.8: *Microheater designs*

(a) Multi-track nickel microheater design. (b) Single-track nickel microheater viewed under a microscope. (c) Microheaters on substrate connected to a power supply using electrical probes. (d) Microheater temperature output measured through a piece of paper using a k-type thermocouple.

Microheaters were designed as both single- and multi-nickel tracks, as shown in figure 2.8(a, b). The multi-track design had separate connectors but the same total length as the single-track design. The reason for including multiple tracks was to allow for tracks to become damaged without the need for re-fabrication. Once deposited, the microheaters are connected to a power supply using electrical probes, shown figure 2.8(c). Using a thermocouple and some paper I was able to measure the temperature output of the microheaters as a function of input power, as shown figure 2.8(d). Paper was used to prevent damage to the microheater tracks during probing.

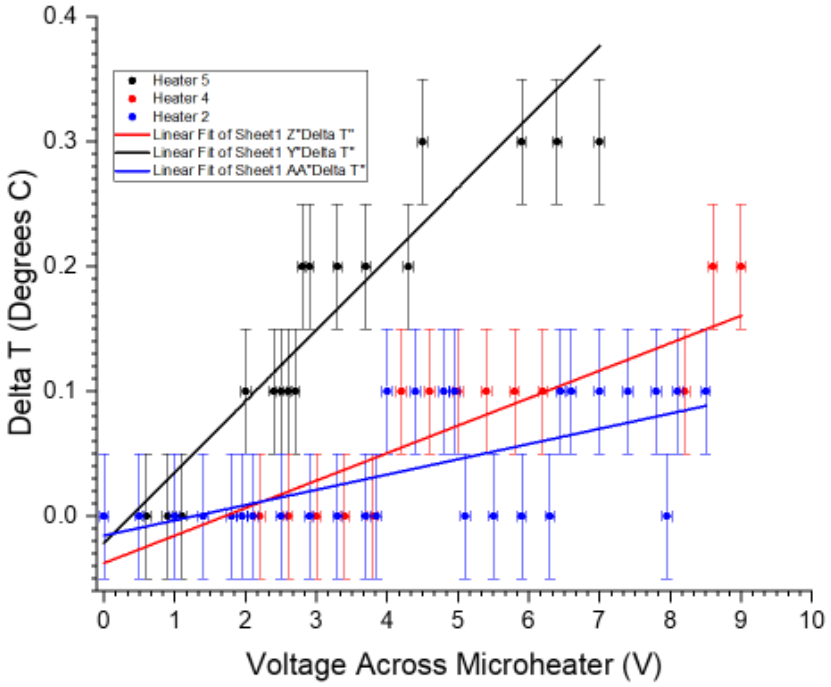

Figure 2.9: *Nickel microheater temperature measurements*

Figure 2.9 shows the results of the temperature measurements for three nickel microheaters. Heater 2 and 4 were multi-track microheaters, and heater 5 was a single-track microheater. The track lengths were designed to be used with a low voltage battery, using equation 2.6, with a deposition depth of 100nm and a track width of 10µm. As figure 2.9 clearly shows, the microheaters did not reach the desired temperature. The obvious test was to check the resistance of the tracks. According to equation 2.4 and 2.5, the resistance of the microheaters should be R = 2.1kΩ. I measured the resistance of the heaters using a potential divider setup, which allows us to measure the resistance of a circuit element with only knowing the voltage supplied and the voltage across another resistor in the circuit, using equation 2.14 to give equation 2.15.

$$V_{In} = V_H + V_R$$

Equation 2.14: *Potential divider voltage*

$$R_H = \frac{R_R}{\left(\frac{V_R}{V_{In}}\right) - 1}$$

Equation 2.15: *Potential divider resistance*

Where V_R is the voltage across the known resistor, V_{In} is the supplied voltage, V_H is the voltage across the microheater, R_R is the resistance of the known resistor, R_H is the resistance of the microheater.

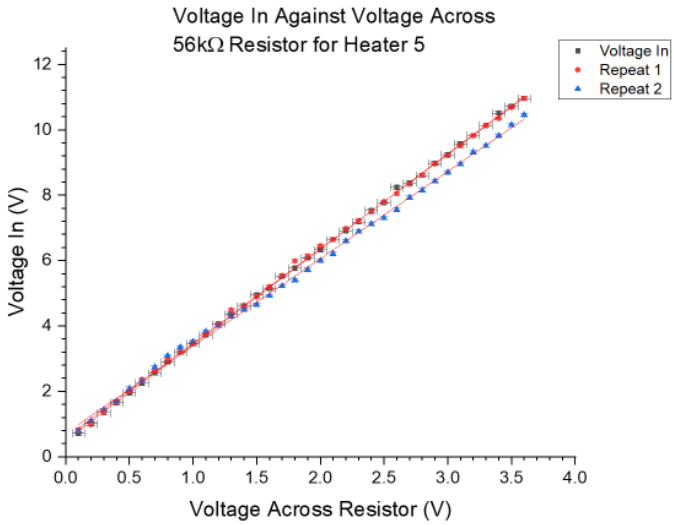

Figure 2.10: *Microheater resistance results*

Figure 2.10 shows one example of a nickel microheater resistance measured using a potential divider setup and showing a resistance of (162±0.9)kΩ, calculated using equation 2.12. Similar values were obtained for other nickel microheaters fabricated in the same way. The measured resistance is much higher than intended, which was found to be due to deposition thickness of the conductor being far less than intended (~10nm).

There were several problems with the microheaters which made them unsuitable for use in our system. Firstly, the deposited nichrome didn't reach the target height, thus reducing the cross-sectional area of the track and increasing resistance. It also turned out that the nickel tracks were fragile and prone to breaking when probed. Ultimately, the temperature output of the heaters was clearly not high enough to achieve analyte concentration [47,48].

2.4.3 Mesh Heaters

The next iteration of the heater design arose from a very simple observation, namely the fact that electronic cigarettes need to heat small amounts of water in a very short time. Here, a liquid is heated by the transfer of thermal energy from a conductor to turn it into steam and use it to carry flavours to the consumer. Electronic cigarettes, or vaping, continues to grow in popularity and is predicted to be worth $32 billion by 2021 [49]. An electronic cigarette is a battery powered device that consists of similar elements as our system, so we can adapt it to our purpose and use some if its elements to improve our system. The heating element can reach temperatures up to 500˚C repeatedly to evaporate oil-based solutions stored in cotton wool [50]. There are two main conductors used in the vaping industry that can be used in our system, namely Kanthal and nichrome.

Nichrome, or nickel chromium, the material used in the initial lithographic heaters, has been widely used in heating elements since 1905 and most commonly occurs as 80% nickel 20% chromium. Nichrome provides an ideal heating element due to an adherent layer of chromium oxide that forms when it is heated for the first time, making it resistance to corrosion. Nichrome heats with a minimal ramp time due to a relatively low resistivity. Kanthal is the trademark

name for a group of iron chromium aluminium alloys that are widely used in a range of resistance heaters. It consists of mainly iron, with a 20-30% chromium and 4-7.5% aluminium. Kanthal is best known for its ability to withstand very high temperatures without failure. Kanthal has a bright annealed and oxidised surface thus making it corrosion resistant and preventing the core becoming oxidised. At the core is ferrite, or α-iron, which is very durable thus allowing Kanthal to withstand repeated heat cycles. Kanthal is characterised by a high consistent resistivity, good oxidation resistance, high maximum operating temperatures, and better longevity, i.e. four times that of nichrome [51–53].

	Kanthal	**NiChrome**
Resistivity [Ωm]	1.5×10^{-6}	$(1\text{-}1.5) \times 10^{-6}$
Coefficient of Thermal Expansion [K^{-1}]	1.1×10^{-7}	1.4×10^{-7}
Specific Heat Capacity [$JKg^{-1}K^{-1}$]	460	450
Thermal Conductivity [$Wm^{-1}K^{-1}$]	11	11.3
Young's Modulus [Pa]	2.2×10^{11}	2.2×10^{11}
Emissivity	0.7	0.6

Table 2.1: *Physical properties of Kanthal and nichrome summary*

The similarities between Kanthal and nichrome are highlighted in table 2.1. Both metals are ideal for use in a heating element. The key differences to be noted are the specific heat capacity, coefficient of thermal expansion and emissivity. I chose to use Kanthal as the heater in our system. Kanthal is more durable, expands less under heating and more readily radiates thermal energy due to its iron core, smaller coefficient of thermal expansion and greater emissivity. Therefore, the Kanthal heater can be used in repeat experiments with only minor deterioration in performance, is more stable over long periods of time due to less alteration in its dimensions and is more efficient in transmitting thermal energy for the same electrical energy.

2.4.4 System Update II

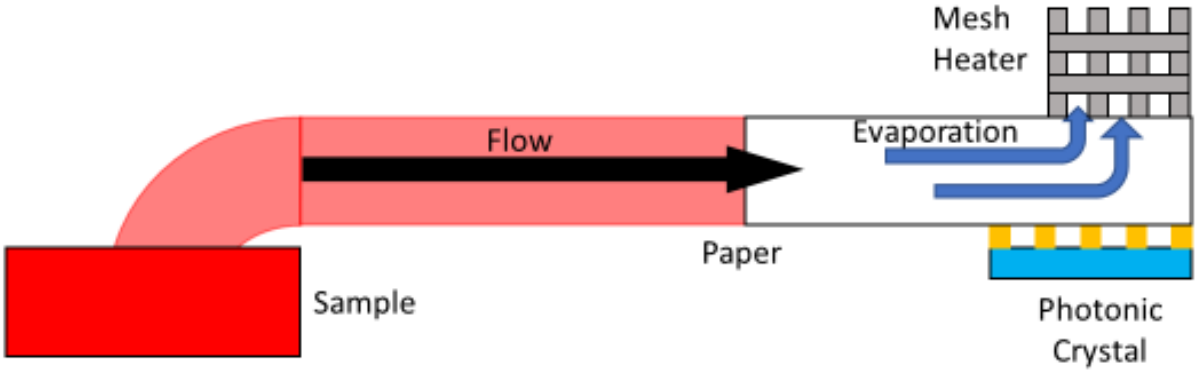

Figure 2.11: *System update II*

System development featuring a sample reservoir, from which the paper draws a sample solution through capillary action, photonic crystal biosensor and a Kanthal mesh heater above the paper channel providing an analyte concentration and continuous wicking action.

Figure 2.11 shows a summary of the system developments, the Kanthal mesh heater is placed above the paper to allow for evaporation of the sample solution, which is still drawn from a reservoir. A concentration of analytes forms at the end of the paper above the photonic crystal, which as before measures a shift in resonant wavelength.

2.4.5 Heater Location

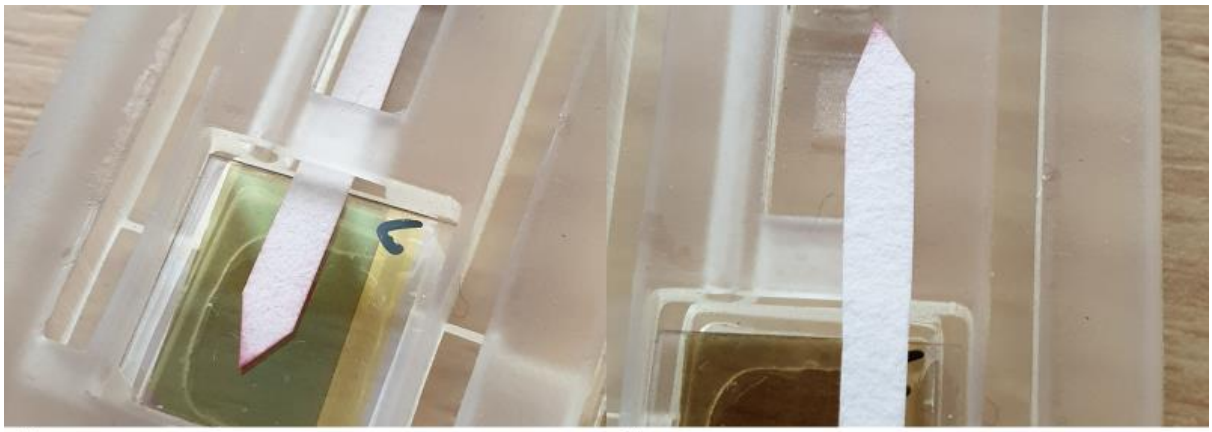

Figure 2.12: *Localisation of analyte due to channel shape*

(a) Top (air) side of the paper channel, (b) Bottom (PhC side) of the paper channel.

The coffee ring effect occurs naturally at room temperature and can be encouraged through the shaping of the paper channel, as discussed earlier in this chapter and shown in figure 2.12. Thermal evaporation of the solution is shown in figure 2.11 to be upwards through the mesh, it follows that the general flow of solution would be upward and therefore away from the sensor. It was proposed that moving the heater underneath the paper may allow for analytes to be drawn downwards towards the sensor, therefore increasing detection rate.

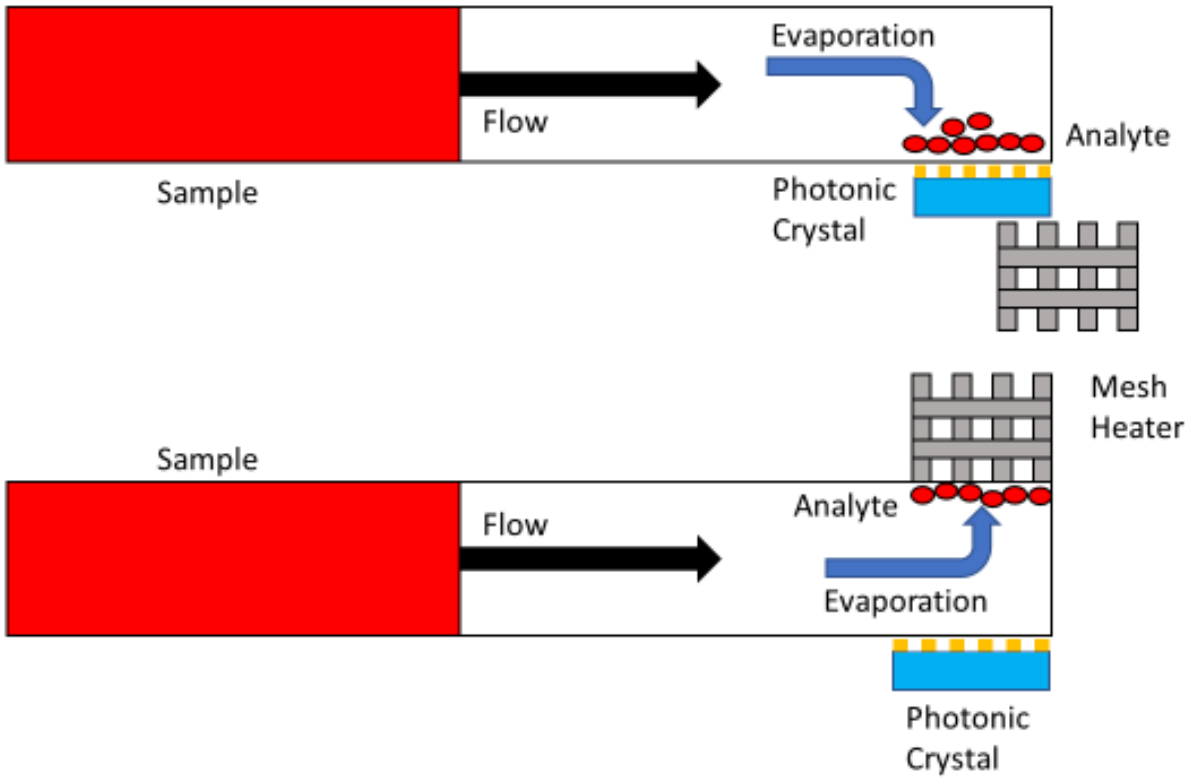

Figure 2.13: *Heater location and theoretical resulting analyte concentration*

To determine if the heat location does determine analyte flow and therefore analyte concentration location, as illustrated in figure 2.13, I again used red food dye to visually observe the analyte flow. I used 300µL of a low concentration of red food dye dissolved in deionised water, which was allowed to flow towards the end of the paper channel for no heater (figure 2.12), and a Kanthal heater both above and beneath the paper.

Concentration on both sides of the paper was measured qualitatively. Both heater above and heater below experiments were left to flow for 3 hours, both channels were still damp during visual inspection.

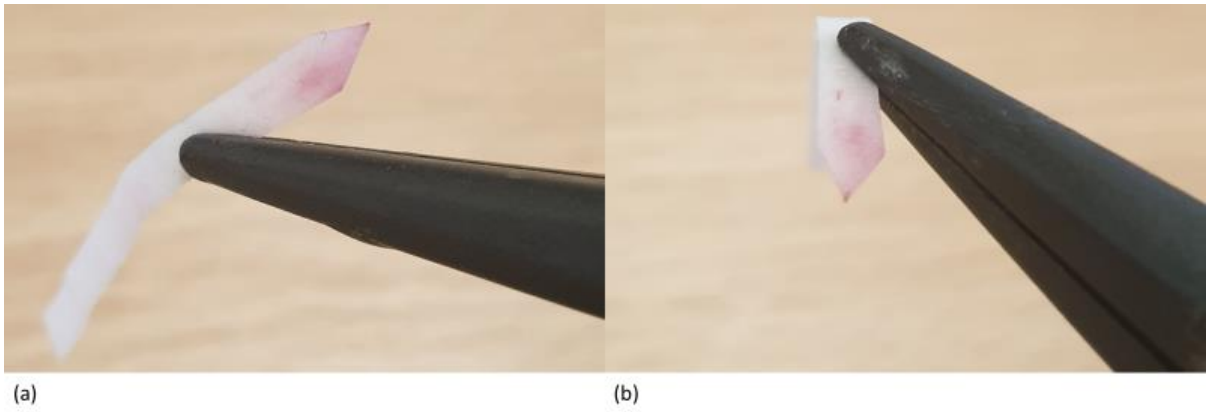

Figure 2.14: *Thermal concentration of analyte with heater above*

(a) Top (heater) side of paper channel, (b) Bottom (PhC) side of paper channel.

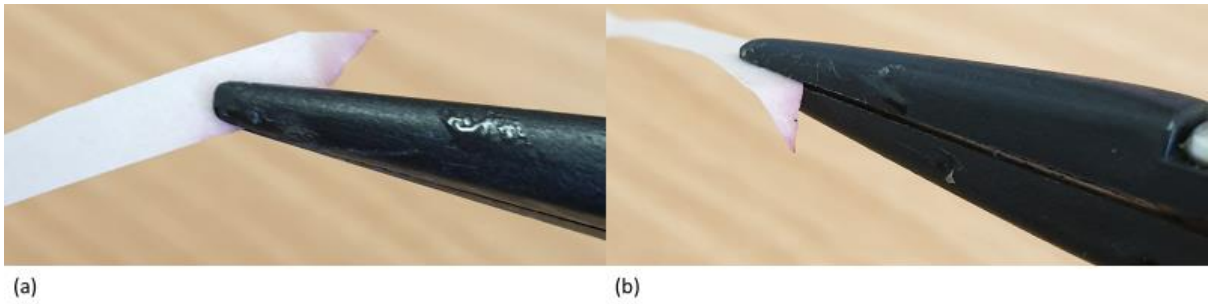

Figure 2.15: *Thermal concentration of analyte with heater underneath*

(a) Top (air) side of paper channel, (b) Bottom (PhC/heater) side of paper channel.

Comparing heater locations with figure 2.14 and 2.15, we see that the heater being above the paper is less efficient at localising the concentration. The red colouring extends further away from the paper channel tip, likely due to the more open nature of the heat flow from above. In both instances, the concentration is increased on the side of the paper that "faces" the heater. Confirmation of this result is shown in chapter 5 (figure 5.9). To fully utilise the thermal preconcentration, the Kanthal heater was moved to the underside of the PhC.

Using a 2.5x1cm shape Kanthal mesh heater I measured the temperature output of the mesh, and the corresponding temperatures in the paper above and underneath the PhC as a function of supplied power. Temperature measurements were taken using a thermocouple place on the mesh and underneath the paper respectively, results shown in figure 2.16.

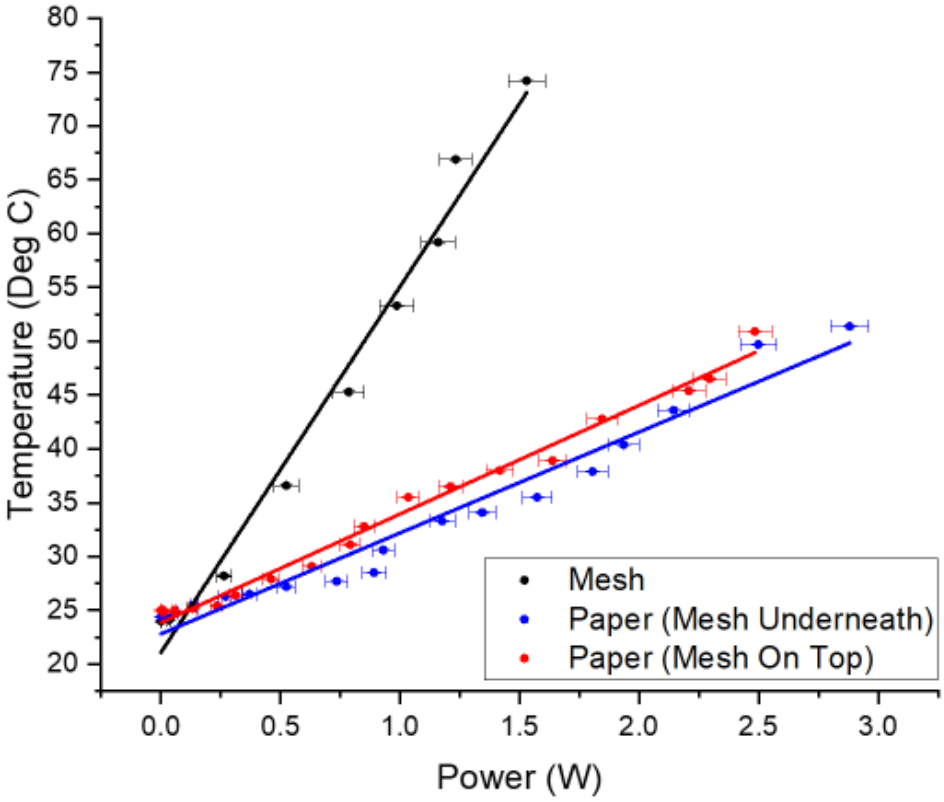

Figure 2.16: *Temperature measurements of Kanthal mesh locations*

Mesh temperature (black) against paper temperature for heater above (red), below (blue).

2.4.6 System Update III

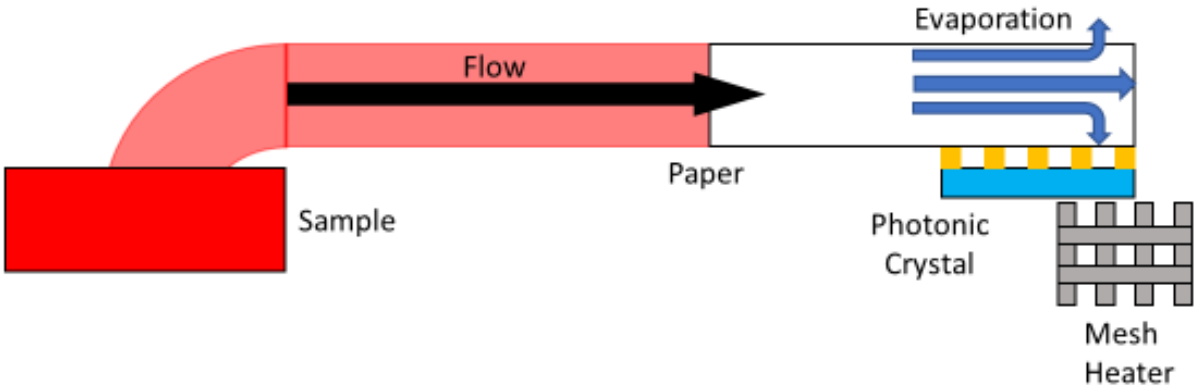

Figure 2.17: *System update III*

Features include a solution/sample reservoir, paper channel, photonic crystal biosensor, Kanthal mesh heater underneath paper to increase concentration of analyte on paper-sensor interface.

Figure 2.17 shows the updated system development. The solution (sample) is kept in a reservoir allowing the paper channel to wick unforced. The sample flows toward the photonic crystal, which is above the Kanthal heater, thus creating a temperature gradient vertically through the paper. The analyte is predominantly concentrated on the paper-sensor interface in the initial experiment phase.

2.5 Targeted Handling of Analytes

The coffee ring effect increases the concentration at the edge of a free-standing droplet containing a solute, as observed in figure 2.3. For a solution contained within a porous medium and exposed to a heat source, the edge of the fluid body becomes the edge of the paper.

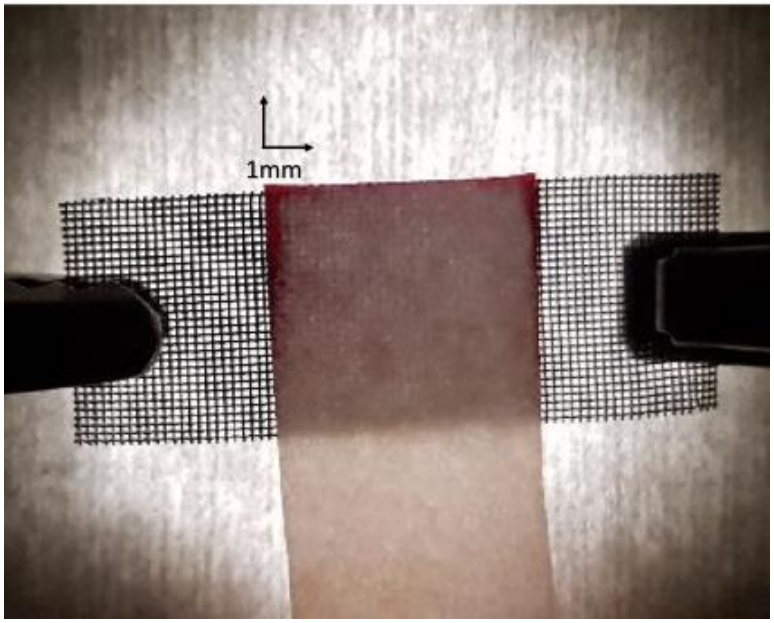

Figure 2.18: *Thermal concentration of analyte in chromatography paper*

The effect of thermally inducing an analyte concentration are observed in figure 2.18. The analyte begins to concentrate on the paper edge, and, as more solution is drawn into the paper channel, the concentration builds up. We investigated the effect of shaping the paper channel end to increase the concentration of analyte. We used three shapes, shown in figure 2.19, and qualitatively assessed this effect.

Paper channels are observed in transmission with a white light source, photographs taken at twenty-minute intervals. Red food dye is used as analyte. Paper channels of 5mm width and 45mm length were used. The Kanthal mesh was heated to 50˚C.

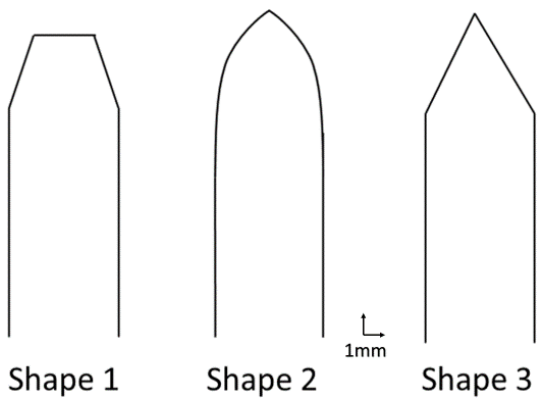

Figure 2.19: *Three shapes of paper channel termination*

2.5.1 Paper Design

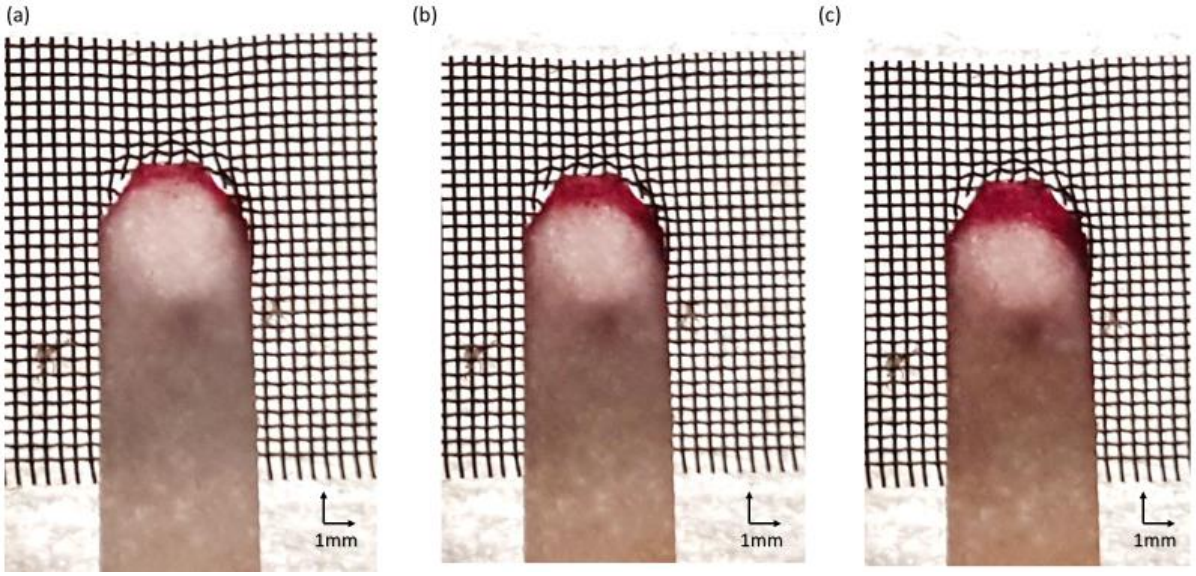

Figure 2.20: *Shape 1 at time (t)*

(a) t = 20 minutes (b) t = 40 minutes (c) t = 60 minutes.

Shape 1 has an improved localisation compared to the square terminated paper shown in figure 2.18. However, the concentration after 60 minutes is largely distributed over the end of the paper channel. The outermost cut-away edges in figure 2.20(a) saturate quickly before the centre area builds up.

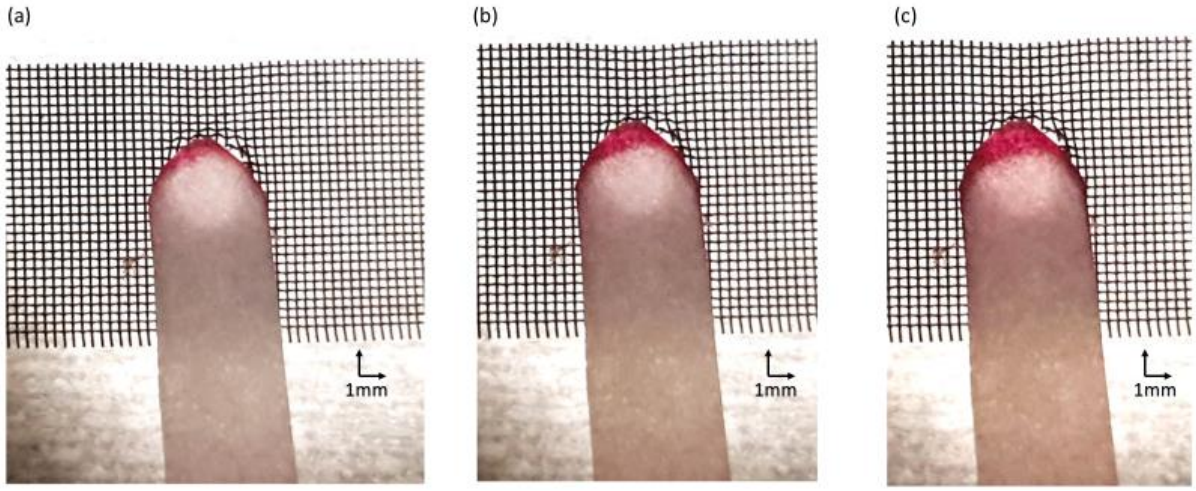

Figure 2.21: *Shape 2 at time(t)*

(a) t = 20 minutes (b) t = 40 minutes (c) t = 60 minutes.

Shape 2 features fewer edges and a sharper point at the tip and benefits from a smaller central are. At t = 60 minutes (figure 2.21(c)) the total covered area is much smaller than in figure 2.20. Visually, the red colour is equal thus the total concentration appears unaffected.

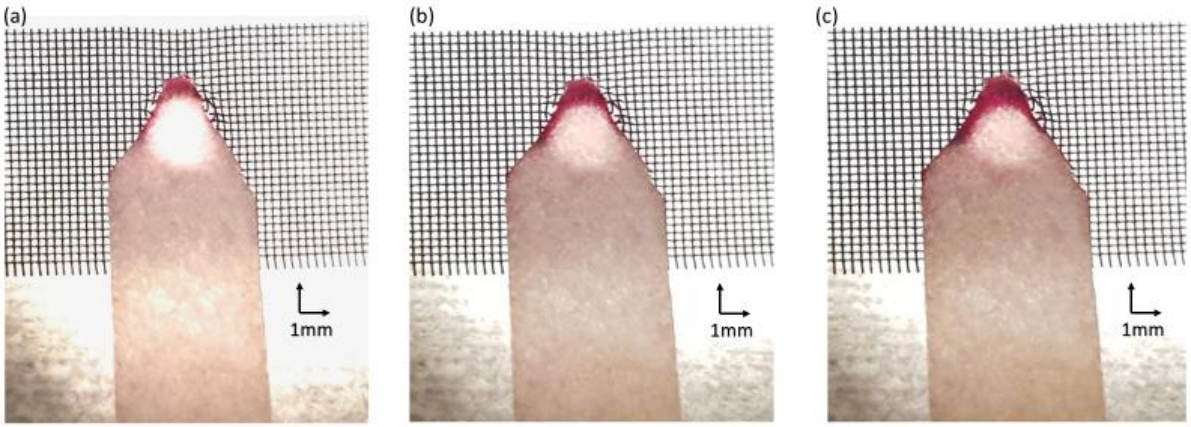

Figure 2.23: *Shape 3 at time(t)*

(a) t = 20 minutes (b) t = 40 minutes (c) t = 60 minutes.

Shape 3 features a shaper point at the paper channel tip than that in figure 2.21. At t= 60 minutes (figure 2.22(c)) the total covered area is lowest of all shapes considered. The red colour is darker than that in figure 2.20, hence we can assume a greater concentration in the tip.

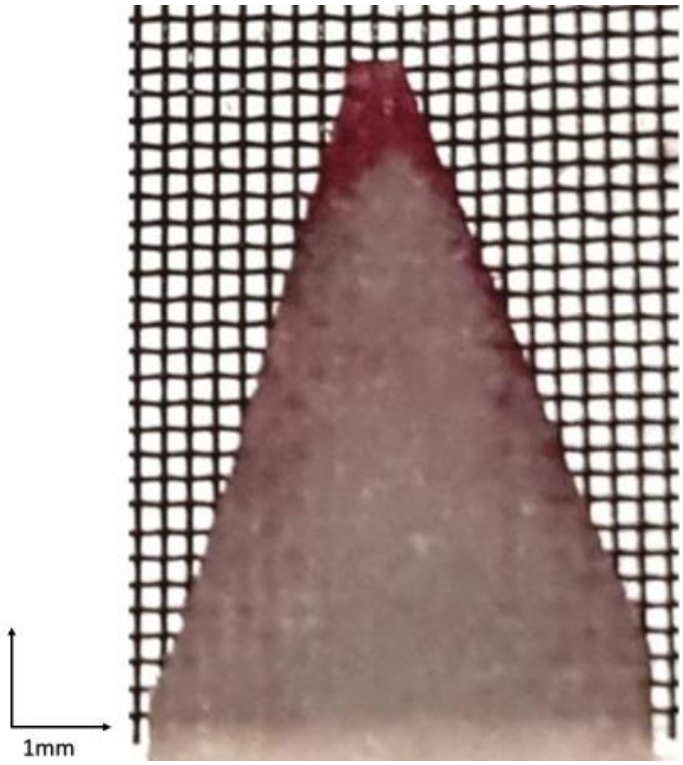

Figure 2.22: *Optimum paper channel shape*

We conclude that the most favourable geometry is to narrow the paper channel tip further and to create a triangular tip. The analyte concentrates initially on the outer edges, and then begins to fill the tip as shown in figure 2.23.

Translating these findings to the sensing application, we note that the area of the grating sensor is 500µm square. Therefore, by reducing the tip width to 1mm, we can ensure that the photonic crystal is quickly and entirely covered with the analyte.

2.5.2 System Update IV

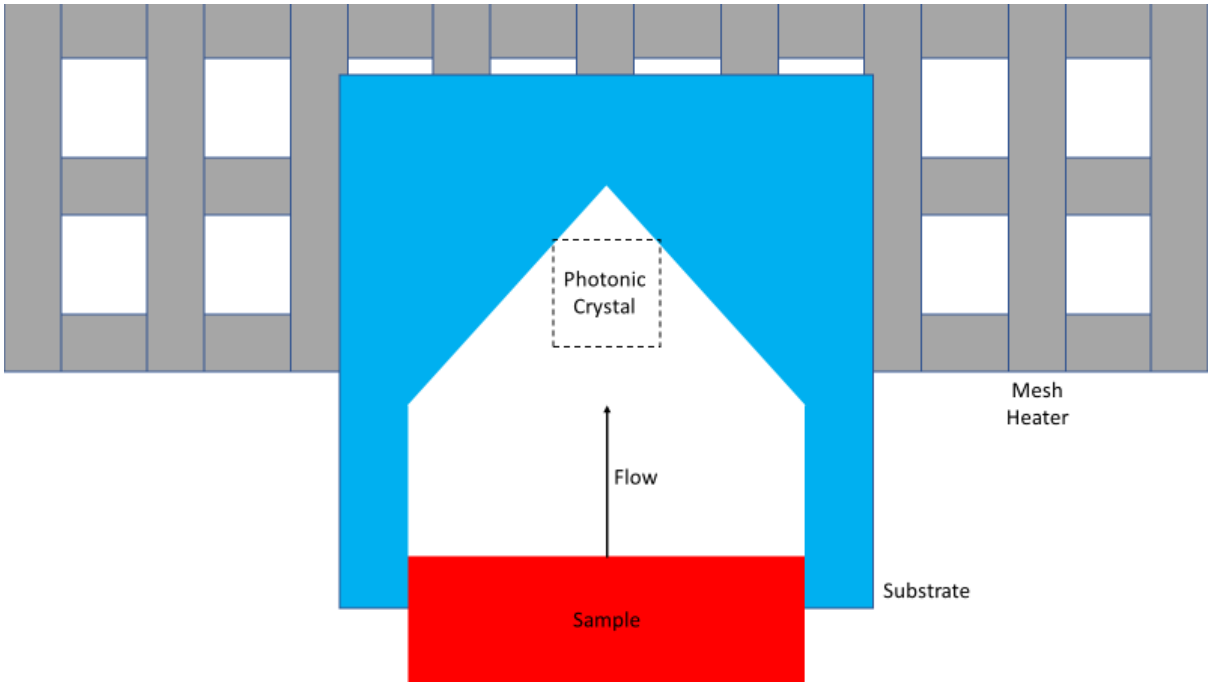

Figure 2.24: *Final system update*

Final system development step. Features include: Kanthal Mesh underneath grating sensor, allowing for measurements in reflection and more effective thermal concentration of analytes. Pointed paper channel tip allows for a better concentration of analytes.

The final system development includes the alterations to paper channel design, with the pointed tip allowing for a more localised concentration of analytes. The remainder of the system is shown in figure 2.17. Analyte concentration results for the system shown in figure 2.24 are discussed in section 5.4, along with a direct comparison with the system shown in figure 2.11.

2.6 Chapter 2 Conclusion

Chapter 2 has discussed the development of a paper-heater-photonic crystal system designed to manipulate the flow of a solution and target the concentration of analytes within. Our system comprises a chromatography paper channel, a solution reservoir, a photonic crystal and a Kanthal heating element. The solution is introduced using a reservoir, to allow for the natural wicking of a porous material to draw the sample into the channel, with the total volume that can be absorbed governed by equation 2.1.

At room temperature, a phenomenon known as the coffee ring effect occurs. The coffee ring effect is the outward flow of a solute due to an evaporation flux across a solution liquid body. It was discovered that this effect can be increased through an induced temperature gradient across the fluid body, as observed in figure 2.3. Drawing a solution through a porous material allows for an analyte within a solution to be concentrated within the porous substrate and the concentration can be increased using a temperature gradient.

Initially it was thought that a micro-heating element could be fabricated around the photonic crystal biosensor to increase the local concentration in only the sensing region, shown in figure 2.8. The microheaters proved to be unsuitable for our system due to their high resistance and fragility causing them to struggle to reach the desired maximum temperature of 60˚C and to break easily when in use. An alternative heating element, from the e-cigarette industry, was proposed, which provided a strong and durable metal, a reliable thermal output and a malleable material. The heating element used was Kanthal, discussed in section 2.4.3 in greater detail, which is an iron-chromium-aluminium alloy with similar properties to other commonly used heating elements, such as nichrome. Kanthal benefits from an iron core, providing greater stability during sustained heating and greater durability across repeated cycles.

The location of the Kanthal mesh was key to ensuring maximum localisation of analytes in the sensing region. While the paper channel is relatively thin (approximately 0.5mm), it is macro-scale compared to test solutes. The location of the heating element is key to the net analyte-flow within the paper channel, as observed in figures 2.14 and 2.15. Combining this effect with the shape of the paper channel tip, shown in figures 2.20-2.22, allowed us to maximise the localisation of analytes.

3. Deposition and Properties of Hydrogenated Amorphous Silicon

3.1 Introduction

Amorphous silicon provides a suitable material for use in photonic crystal biosensing due to its relatively high refractive index [54] especially when compared to competing materials such as silicon nitride (Si_3N_4) [55]. Amorphous silicon also provides a suitable surface for biological functionalisation due to its high reactivity with oxygen [56]. Chapter 3 will cover the deposition of hydrogenated amorphous silicon thin films, measuring thickness and optical properties.

3.2 Hydrogenated Amorphous Silicon

An amorphous material, or non-crystalline material, is a solid lacking the long-range order typical of crystalline structures. Amorphous materials are instead formed of interconnected structural blocks bearing some resemblance to the basic crystalline structural units [57]. Crystalline silicon forms strong covalent bonds tetrahedrally with neighbouring atoms due to outer shell electron configuration and valence electron sharing [58]. Crystalline silicon suffers from a high defect density which can prevent useful properties such as doping and photoconductivity [59].

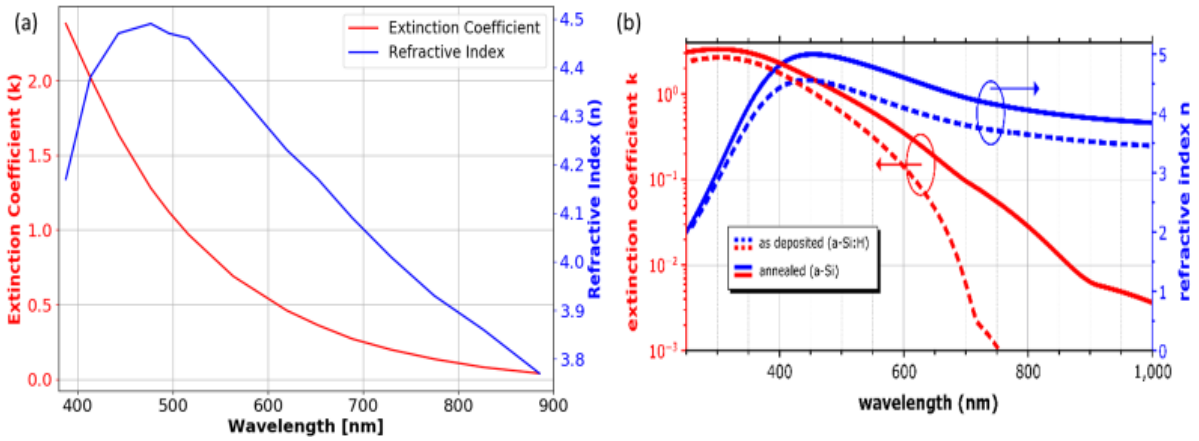

Figure 3.1: *Known values for refractive index and extinction coefficient of a-Si*

(a) Literature values for refractive index (blue) and extinction coefficient (red), (b) Known experimental comparison data between hydrogenated and non-hydrogenated amorphous silicon (C. Schuster).

In amorphous silicon, there are many irregularities in the bonding structure, leaving many atoms with dangling bonds [60]. These dangling bonds create defects in the bandgap thus increasing photon absorption. The increase in absorption caused by dangling bonds can be

effectively removed by occupying these bonds with hydrogen atoms, i.e. through hydrogenation of amorphous silicon [61].

As shown in figure 3.1, amorphous silicon has a complex refractive index (**n**), shown in equation 3.1, which relates refractive index (n) and extinction coefficient (k). Amorphous silicon is considered a direct-bandgap material, so has a relatively high extinction coefficient in the visible which drops towards the near infra-red spectrum. Adding hydrogen to the dangling bonds of amorphous silicon during deposition has been shown to decrease the extinction coefficient, thereby reducing absorption [62,63].

$$\mathbf{n} = \mathrm{n} - \mathrm{ik}$$

Equation 3.1: *Complex refractive index*

A plane wave with frequency (f) propagates through a material with velocity (*v*) with a direction (x), the electric field (E) is related to the incident electric field (E_0) through equation 3.2 below.

$$E = E_0 e^{i2\pi f\left(t-\left(\frac{x}{v}\right)\right)}$$

Equation 3.2: *Electric field of propagating wave*

Substituting the known relation between the wave velocity, speed of light and complex refractive index (*v* = c/**n**), and substituting equation 3.1, we can rewrite equation 3.2 as follows.

$$E = E_0 e^{i2\pi ft} e^{-\frac{i2\pi xn}{c}} e^{-\frac{2\pi fkx}{c}}$$

Equation 3.3: *Electric field of propagating wave*

The final term in equation 3.3 is known as the damping factor and is closely related to the absorption coefficient of a material. Using the damping term, the fraction of incident power ($P = \sigma E^2$) propagated from x=0 to x=x through a material with conductivity (σ) we find an expression for the absorption coefficient.

$$\frac{P(x)}{P(0)} = \frac{\sigma E^2(x)}{\sigma E^2(0)} = e^{\left(-\frac{4\pi fkx}{c}\right)}$$

Equation 3.4: *Absorption coefficient expression*

Leaving the absorption coefficient as shown in equation 3.5 and can be expressed in terms of wavelength(λ) [64].

$$\alpha = \frac{4\pi fk}{c} = \frac{4\pi k}{\lambda}$$

Equation 3.5: *Absorption coefficient*

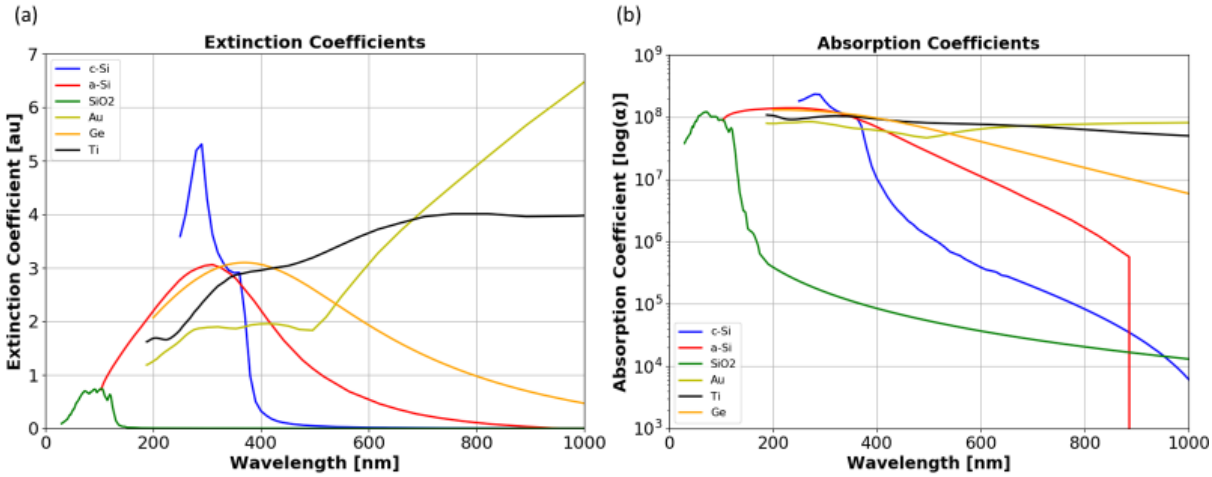

Figure 3.2: *Literature values of extinction and absorption coefficients*

(a) Extinction coefficients for a range of materials used in the fabrication of photonic crystal and plasmonic optical biosensors. (b) Corresponding absorption coefficients (per metre) plotted on a logarithmic scale.

The relationship between extinction coefficient and absorption coefficient is highlighted in equation 3.5 and in figure 3.2 for a range of materials frequency used in photonic crystal and plasmonic biosensors. Units for absorption coefficient are given as $[m^{-1}]$ and displayed in figure 3.2 on a logarithmic scale. It is clear that non-hydrogenated amorphous silicon is highly absorbing in the visible spectrum, while it drops sharply in the near-IR.

3.3 Deposition Techniques

The two most common techniques used for the deposition of hydrogenated amorphous silicon (a-Si:H) are chemical vapor deposition (CVD) and physical vapor deposition (PVD). Chemical vapor techniques, including plasma enhanced (PECVD) and catalytic CVD, are a coating process using thermally induced chemical reactions on the substrate surface. Chemical reagents are supplied in gas form and can on occasion include reactions with the substrate material itself [65]. By contrast PVD techniques involve a solid material, often referred to as a target, which is vaporised in a vacuum and then deposits on a substrate. The transfer of coating material can be on the single atom or molecular level and therefore can provide a high purity deposition [66]. Both techniques have their own advantages and disadvantages which will be briefly considered in this chapter.

In PECVD processes the film deposition is achieved through the introduction of reactant gases between parallel electrodes. One electrode is energised with a radio frequency (RF), alternating current (AC) or direct current (DC) while the other remains grounded. Capacitive coupling between electrodes is sufficient to excite a plasma with the reactant gases. The plasma induces a chemical reaction resulting in a reaction product being deposited on the substrate which is typically heated between 250˚C and 350˚C which can cause high strain or damage to a deposited film [67]. Other CVD processes are performed at temperatures of 350˚C or above thus making them unsuitable for the deposition of amorphous silicon [68]. Silane plays a key role in

the deposition of silicon through CVD processes which can spontaneously combust in air without external ignition, so is very hazardous [69].

Sputtering is a thin film PVD process used in a variety of sectors including the fabrication of semiconductors and optical devices. Sputtering relies on an exchange of momentum between high energy ionised inert gas atoms and a target material to eject surface target atoms with the intention of deposition on a substrate.

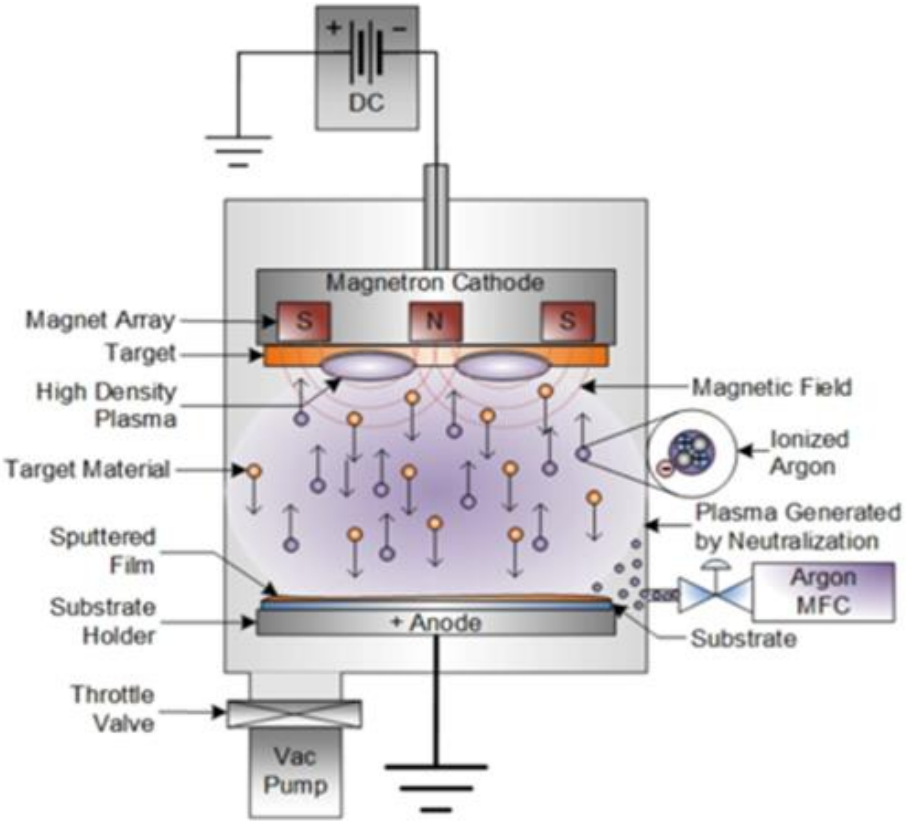

Figure 3.3: *DC magnetron sputtering*

Argon flows in through gas inlet, towards the cathode. A strong magnetic field manipulates free electron movement, preventing flow towards the anode. [© Semicore 2019].

Sputtering requires a target material, a substrate, an inert gas (typically argon), a large potential between an anode and a cathode and a vacuum chamber, as shown in figure 3.3. A negatively charged target allows free electrons within the target to flow away and collide with outer shell electrons within the gas creating positively charged gas ions. The movement of these free electrons towards the anode can be prevented through magnetic field manipulation, thus reducing substrate bombardment. Subsequently the positively charged ions impact upon the negatively charged target and eject surface atoms at high velocities towards the anode [70]. Vaporised target atoms condense on the substrate surface, where the deposition thickness is monitored using a quartz crystal microbalance (QCM) [71]. DC sputtering deposits a net charge on the target, most notably with dielectric materials. Using a pulsed DC supply avoids this problem by the intrinsic polarity reversal [72].

3.4 Depositing Hydrogenated Amorphous Silicon

I used the pulsed DC magnetron sputtering technique to fabricate a series of a-Si:H thin films on to either a silicon dioxide (silica, SiO_2) or a silica-silicon-silica substrate. The parameters that were controlled during the sputtering process were the deposition rate and the thickness. Both the rate and the thickness were measured with a quartz crystal microbalance (QCM). Quartz is a piezoelectric material and the quartz crystal is made to oscillate at a set frequency though the application of a voltage. The oscillation frequency is affected by the change in mass on the surface of the QCM. The change in mass, which can be as small as nanogram, can be monitored in real time and can be used to calculate a rate and thickness for a known atomic mass [73].

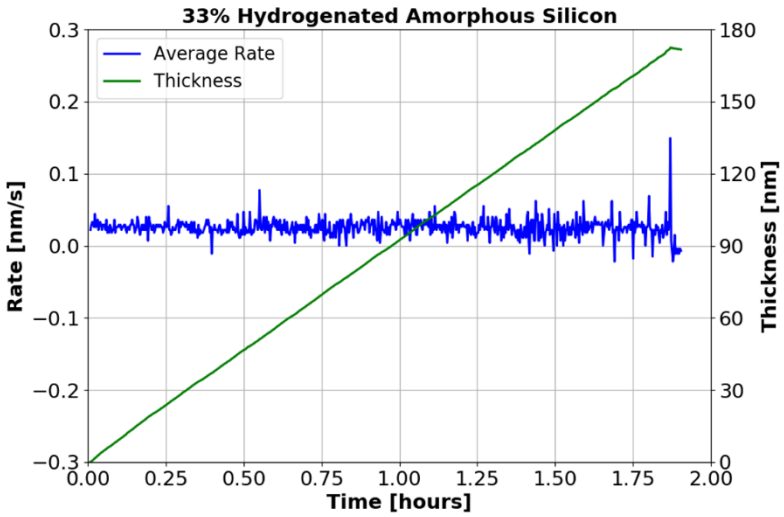

Figure 3.4: *Deposition parameters measured with a QCM*

Deposition parameters measured using a quartz crystal microbalance (QCM) during a pulsed DC magnetron sputter deposition of hydrogenated amorphous silicon (a-Si:H) in a 67% argon 33% hydrogen atmosphere.

Figure 3.4 shows measurements made using a QCM for both average deposition (blue) and deposition thickness (green) for a 33% hydrogenated amorphous silicon film. The percentage of hydrogenation corresponds to the percentage of hydrogen in the total gas flow into the chamber, see table 3.1.

Other parameters that were monitored during the process include total gas flow, chamber pressure and DC power. A copper-backed silicon target is used as the deposition material, copper acting both as a good electrical conductor and a heatsink.

The gas flow rate into the chamber was measured in units of standard cubic centimetres per minute (SCCM). Argon, as the inert plasma gas, was introduced to the chamber at a base flow rate of 20 SCCM, with higher flow rates used when required though high flow rates tended to reduce deposition uniformity across the substrate. Table 3.1 below show the flow rates used and the corresponding hydrogen concentrations.

Ar Flow Rate [SCCM]	H Flow Rate [SCCM]	Total Flow Rate [SCCM]	Hydrogenation [%]
20	0	20	0
24.5	0.5	25	2
20	1	21	5
20	2.5	22.5	10
20	5	25	20
20	10	30	33

Table 3.1: *Flow rates used during a-Si:H depositions*

Flow rate in standard cubic centimetres per minute (SCCM) for argon (Ar) and hydrogen (H) used during a-Si:H films during this project. Corresponding hydrogenation concentrations calculated as hydrogen flow rate as a percentage of total flow rate and used to denominate separate depositions.

Gas was allowed to flow into the chamber for five minutes before any power was applied to the silicon target to allow for any un-evacuated gas to be drawn out of the chamber. The chamber pressure during sputtering was maintained at $7.5x10^{-3}$mbar using a vacuum pump and a flow gate to control gas outflow.

The deposition rate is directly proportional to the power and I found that film quality suffered when using power levels of 150W or higher. As film quality is more important than rate, I used a DC power of 100W with a ramp time of three minutes in order not to stress the silicon target. The plasma is then allowed to bombard the silicon target for another 5 minutes before deposition begins, which allows for any impurities on the surface of the silicon target to be removed, thereby increasing the purity of the deposited film.

3.5 Measuring Film Thickness

A surface profilometer was used to provide an accurate measure of the deposited film thickness. The profilometer can measure a step height of less than 10nm and has a stylus radius of 2µm, which limits its lateral resolution. Areas of the silica substrate beneath each deposited film were covered during sputtering to create a step, and each film was measured in at least four locations with each location measured twice to yield an average film thickness.

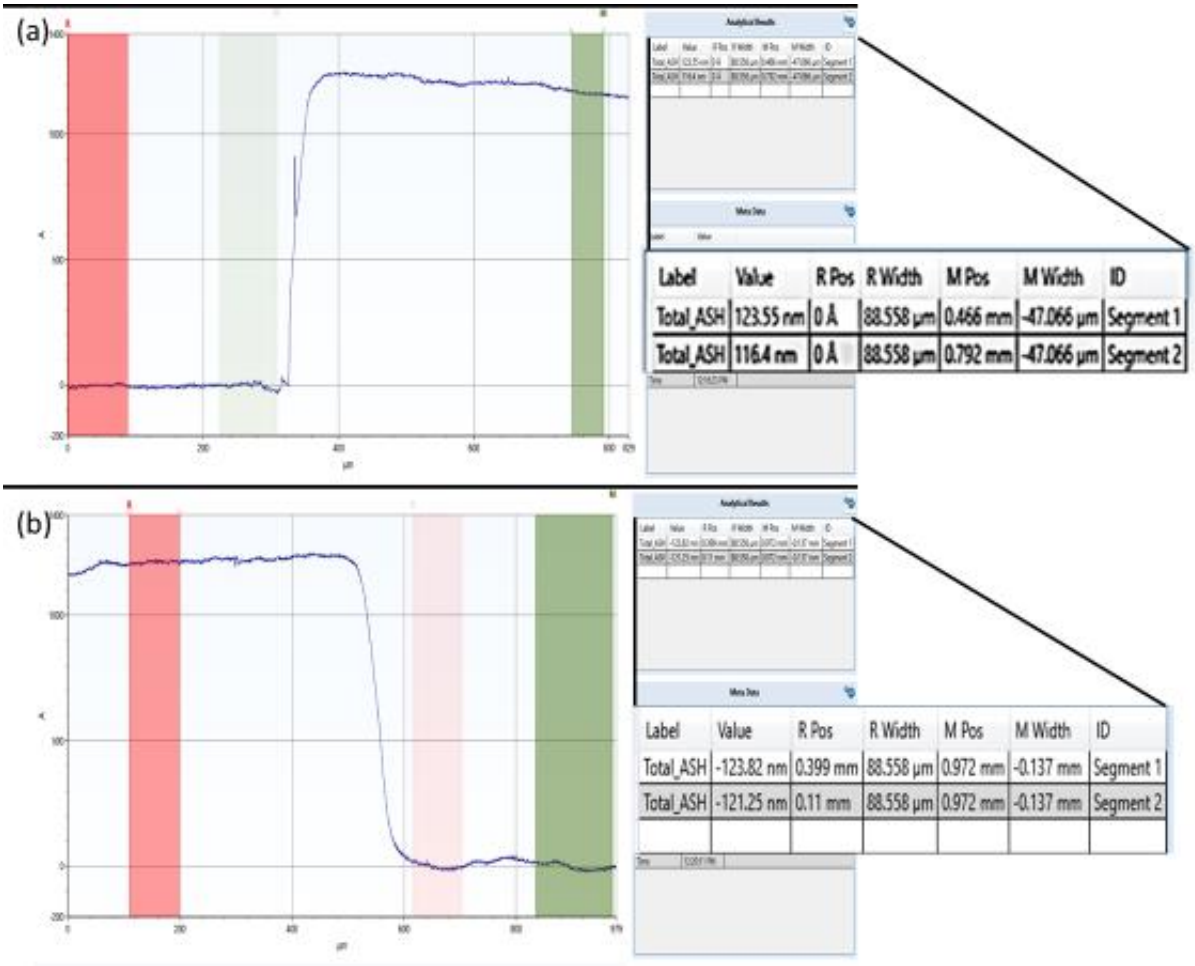

Figure 3.5: *Stylus profilometer of 33% a-Si:H thin film*

Two of the four measurements are shown. (a) Positive step height measured during transition from silica to deposited film. (b) Negative step height measured during transition from deposited film to silica.

Figures 3.4 and 3.5 were chosen to illustrate the difference in measured deposition thickness during the sputtering process and the measured film thickness using a stylus profiler. The average film thickness in figure 3.5 was calculated to be (123±7)nm in contrast to the thickness of 171.6nm measured by QCM. The difference in thickness between measurements is dependent on many factors, such as the omnidirectional nature of sputtering and the radial mass sensitivity of a QCM [74].

Obtaining an accurate measurement of film thickness is important due to the nature of light in resonant gratings. One of the conditions for guided mode resonance within a grating is that the effecting index of the grating be greater than all surrounding refractive indices. A higher effective index ensures the grating layer can support guided modes, and the thickness of the grating (dictated by the film thickness) determines the number of modes that can be supported [26]. Statistical analysis was conducted over a series of depositions to calibrate for the difference in thickness measurements from the QCM and surface profilometer, which is shown in appendix figure A.1. Calibration was possible to within a 20nm film thickness, so a large error remains.

3.6 Spectroscopic Ellipsometry

Spectroscopic ellipsometry provides a contactless, non-invasive and non-destructive optical technique to determine the thin film thickness and optical properties through the change in polarisation state of light reflected from a thin film sample [75]. The polarisation change is typically represented through the complex Fresnel reflection coefficients, amplitude change (Ψ) and phase difference (Δ). The measured response of the material is dependent on material properties such as thickness and optical properties shown in equation 3.1 (refractive index and extinction coefficient). Ellipsometry can determine the refractive index and extinction coefficient for a known thickness or vice versa.

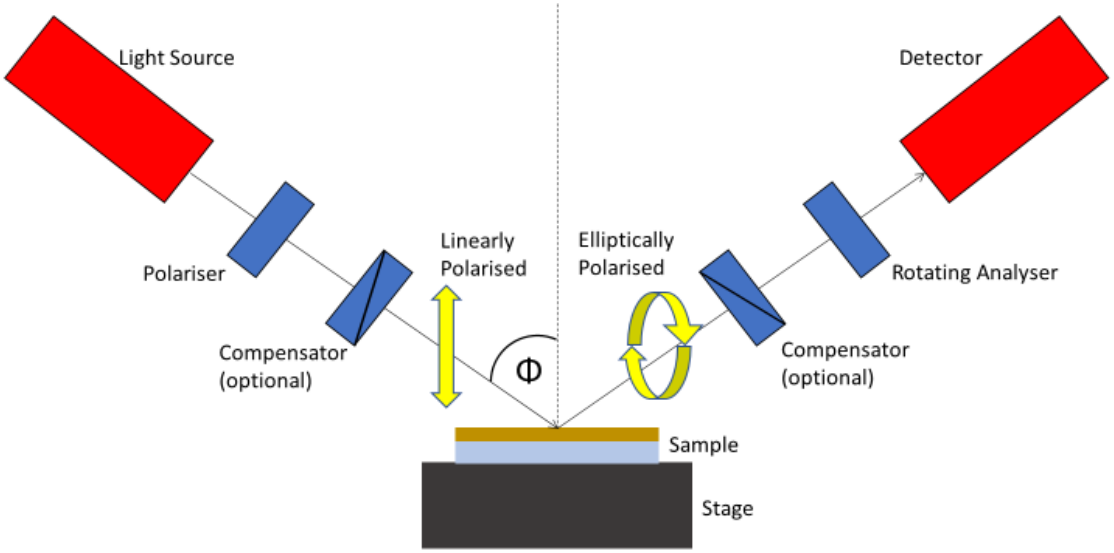

Figure 3.6: *Schematic diagram of ellipsometer*

Optical elements required to determine the change in polarisation of the light upon reflection at the sample are shown.

Ellipsometry detects how p- (parallel) and s- (perpendicular, from German "senkrecht") components change upon reflection or transmission in relation to each other. The change in light polarisation is used to determine the sample material's thickness and optical constants. The main components for collecting ellipsometry data are shown in figure 3.6, and include a light source, a polariser, the sample, an analyser and a detector. The broadband light source produces an unpolarised light wave which passes through a polariser. Incident linearly polarised light reflects from the sample surface and becomes elliptically polarised. The analyser allows an amount of light to pass through dependent on the polariser's orientation with respect to the electric field coming from the sample. The reflected polarisation is determined by the detector and the change in polarisation (ρ) in the ellipsometry measurement is calculated as shown in equation 3.6.

$$\rho = \tan(\Psi)\, e^{i\Delta}$$

Equation 3.6: *Ellipsometry polarisation*

The most common technique for obtaining optical constants, n and k, and thickness of materials using spectral ellipsometry is to fit the experimental data to a known model. Thickness and optical constants are not mutually exclusive when measured using ellipsometry. Material

thickness affects the path length of light travelling through the film and the refractive index determines the velocity and refracted angle of reflection of light travelling through the material. Both optical constants must be known or determined along with thickness to obtain accurate results. A dispersion relationship describes the optical constants' shape as a function of incident wavelength and can be modelled using a model such as the Cauchy model given in equation 3.7, where y represents n[76].

$$y(\lambda) = A + \frac{B}{\lambda^2} + \frac{C}{\lambda^4}$$

Equation 3.7: *Cauchy model*

The corresponding k value, as the imaginary index in equation 3.1, is calculated using the Kramers-Kronig relations. The Kramers-Kronig relations are mathematical relations for calculating the real or imaginary part of response functions in physical systems from the imaginary or real part respectively. The relations are commonly used with respect to the dispersion relation as they assume strict causality. That is to say that no reflected wave can appear until the incident wave has reached a part of the reflector[77].

All sample layers are analysed during ellipsometry due to reflection and transmission at all interfaces. To account for the substrate onto which the a-Si:H films were deposited I used ellipsometry to measure the thickness for known optical constants pre-deposition. I then used spectral ellipsometry to characterise the different deposited a-Si:H films as a function of hydrogenation level.

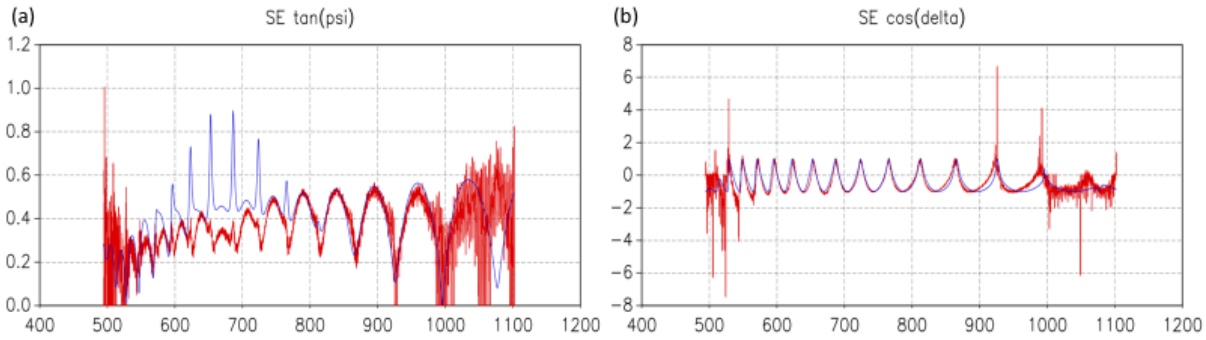

Figure 3.7: *Raw ellipsometry data*

Ψ and Δ data gathered from a measure in change in polarisation for a hydrogenated amorphous silicon film, plotted as tan(Ψ) (a) and cos(Δ) (b). Red represents the measured film and blue represents a Cauchy model for amorphous silicon. Cauchy parameters are adjusted until the best fit of model onto measured data is found.

Finally, the measured data, shown in figure 3.7 in red above, is compared to a Cauchy model of amorphous silicon, shown in blue above. Cauchy coefficients A, B and C in equation 3.7 are altered for refractive index and extinction coefficient until the closest fit between the model and the measured data is achieved (regression). Peaks in figure 3.7(a) highlight an amplitude maximum from the Fabry Perot mode for incident light between 600nm and 800nm. Film and substrate thickness are also altered within a range of 20nm compared to that measured by the surface profilometer. Cauchy coefficients for n and k are then used to plot a dispersion relation.

3.7 Results

Figure 3.8 shows the dispersion relations for six different deposited hydrogenated amorphous silicon films. Refractive index (n) is shown in blue and extinction coefficient (k) shown in red, with solid line representing the deposited film and the dashed line representing an amorphous silicon reference [54]. All dispersion relations were plotted using a Cauchy model with coefficients determined using regression.

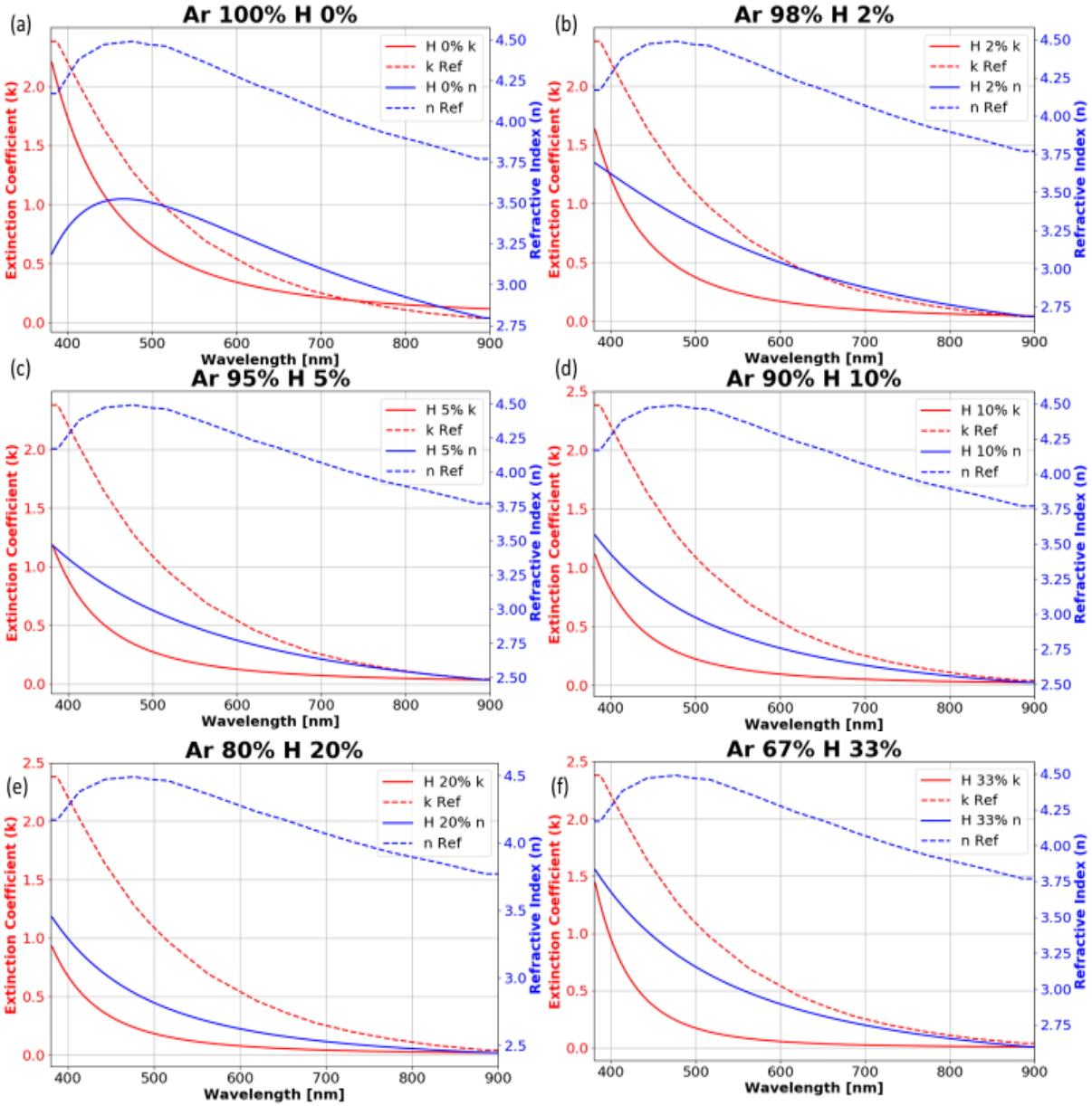

Figure 3.8: *Measure a-Si(:H) dispersion relations*

Refractive index (blue) and extinction coefficient (red) for (a) 0% hydrogenated amorphous silicon, (b) 2% hydrogenated amorphous silicon, (c) 5% hydrogenated amorphous silicon, (d) 10% hydrogenated amorphous silicon, (e) 20% hydrogenated amorphous silicon, (f) 33% hydrogenated amorphous silicon. Sputtered films are shown as solid lines, and the literature values for amorphous silicon are shown as dashed lines. Dispersion relations plotted using a Cauchy model.

Figure 3.8(a) shows a 0% hydrogenated amorphous silicon film (a-Si), which serves as a calibration measurement for the deposition technique used in this project. The extinction coefficient for 0% a-Si:H is a close fit to that of known literature values, showing a peak offset around 500nm incident light. Dispersion relations for the remaining hydrogenation levels figure 3.8(b-f) show that adding hydrogen to amorphous silicon reduces the extinction coefficient in the near-IR spectrum, due to the saturation of dangling bonds as discussed earlier.

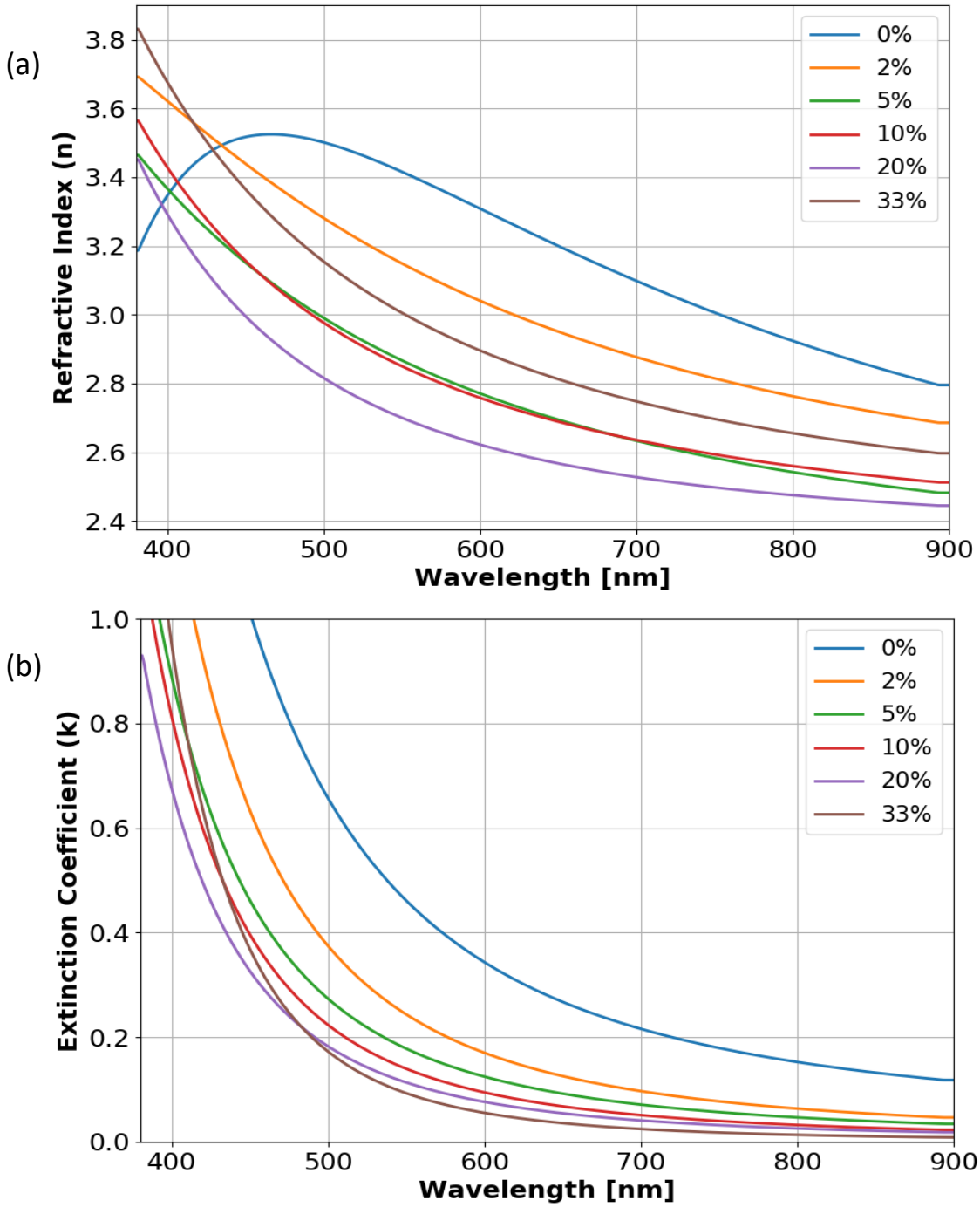

Figure 3.9: *Measured extinction and absorption coefficients*

(a) Refractive index (n) comparison for sputtered hydrogenated amorphous silicon films. (b) Extinction coefficient (k) comparison for sputtered hydrogenated amorphous silicon films on a logarithmic scale.

Figure 3.9 shows a comparison between the different hydrogenation levels for the refractive index(a) and extinction coefficient(b) for a-Si:H films shown in figure 3.8. Figure 3.9(a) shows that the refractive index, with the exception of 33%, decreases as hydrogenation increases for incident light in the visible spectrum. Figure 3.9(b) shows that the extinction coefficient decreases as level of hydrogenation increases for incident light in the visible spectrum. In all instances, the refractive index of the sputtered films is around 1 RIU lower than literature values, which is a concern. It indicates that there might be impurities, such as oxygen, which would lead to a silicon-rich silicon oxide. The oxygen could originate from a leak in the sputtering system. A thorough leak-check was performed and initially some leaks were found, but the film quality did not change noticeably afterwards. In order to explore this issue further, I conducted surface chemistry analysis.

3.8 X-Ray Photoelectron Spectroscopic Analysis

X-ray photoelectron spectroscopy (XPS) is a technique used to analyse the surface chemistry of a material including elemental composition, chemical state and electronic state of the elements within the material. A material's surface is irradiated with a beam of X-rays which releases electrons from the first 1-10nm of the material. The kinetic energies of these electrons are measured, and a photoelectron spectrum is recorded by counting ejected electrons over a range of kinetic energies. Peaks in an XPS spectrum represent atoms emitting electrons of a characteristic energy, thus enabling identification and quantification of surface elements [78].

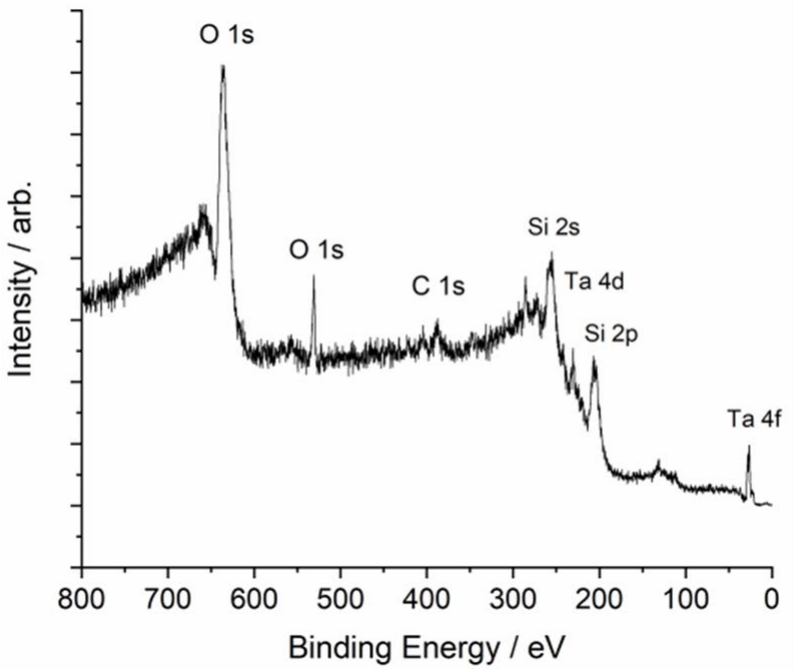

Figure 3.10: *X-Ray photoelectron spectroscopy of a-Si:H*

XPS of a 20% a-Si:H sputter-deposited film showing two clear oxygen peaks and other elements corresponding to the stage elements (noise).

I used XPS to determine the surface chemistry of a 20% hydrogenated amorphous silicon film to see if there were any imperfections or elements present that could cause the decrease in refractive index observed in figure 3.8. XPS revealed two strong oxygen peaks and two silicon peaks on the 20% hydrogenated a-Si:H film's surface shown in figure 3.10. The sharp peaks in figure 3.10 indicate a scattered photoelectron that has been detected without a loss in kinetic energy. It is common to see a much shallower and broader peak close to these sharp peaks and these indicate a background photoelectron that has lost some of its kinetic energy. The step-function shape of figure 3.10 arises from the inelastically scattered electrons from lower energy ionisations which, as the binding energy increases, become a much larger contribution to the overall background noise.

There are other peaks which we associate with the target holder. The presence of the oxygen, however, is a clear indication that there is a silica (SiO_2) in the top surface of the deposited film. Silica has a refractive index of 1.45 [79]. Silicon has a high reactivity with oxygen, so the presence of silica can be attributed to atmospheric reactions post-deposition [56]. The presence of such a refractive index on the surface and substrate of all deposited films is still not sufficient to reduce the bulk refractive index to the levels observed in figure 3.8.

3.9 Chapter 3 Conclusion

Using pulsed DC magnetron sputtering, I have been able to deposit hydrogenated amorphous silicon films that serve as the waveguiding material for my guided mode resonant sensor. I varied the levels of hydrogenation via the flow ratio. Argon was used as an inert gas to initiate a plasma, and hydrogen was added into the chamber. Both gases were controlled using mass flow controllers and evacuated using a vacuum pump and a gate controller to maintain a constant pressure within the sputter chamber. Hydrogenation percentages varied from 0%, 2%, 5%, 10%, 20% and up to 33%.

Using spectral ellipsometry, surface profilometry and regression analysis, I was able to determine values for the optical constants, refractive index and extinction coefficient (n and k). Using a Cauchy model and Kramers-Kronig relation, I determined the relation between hydrogenation level and extinction coefficient. The greater the level of hydrogenation the lower the extinction coefficient, and therefore the lower the material absorption.

The refractive index of amorphous silicon is reduced during the sputtering process. Through x-ray photoelectron spectroscopy I was able to determine the presence of oxygen in the top 1-10nm of the material. Silicon is highly reactive with oxygen, as such the presence of oxygen is not surprising but can partially explain the reduction in measured refractive index due to the formation of silica. A further XPS scan was done for a 0% hydrogenated a-Si:H film, shown in appendix figure A.2, which shows a strong oxygen peak at roughly the same binding energy as in figure 3.10. The presence of oxygen in both samples could be due to oxygen bonding post-deposition or could be more indicative of the presence of oxygen during deposition. Sputtering with a silicon target is not a quick process and any oxygen present in the chamber during deposition would be able to react with the surface silicon easily, thus creating a deposited film more like silicon-rich hydrogenated silica.

Other factors such as tensile or compression stress during deposition could account for the refractive index difference between measured and literature values. It is known that sputter-deposited films may undergo compression stress at low working pressures which can cause defects to arise within the film structure. While this is more common in the deposition of metals, semiconductors can also be affected[80]. These voids or defects could quite easily be filled with hydrogen, during the deposition, or atmospheric gases, post deposition. Thus, a shift in the refractive index of the film would be observed.

With respect to figure 3.9, it is possible that the Cauchy coefficients are stuck in a local minimum. The measured spectrums would still match the model but other coefficients with similar fits may yield values closer to the expected literature values. Multiple measurements were taken for all the deposited films and corresponding Cauchy coefficients/Kramers-Kronig parameters calculated and, while the technique allows for rapid variation of the parameters, it is still possible that a local minimum was used. With a much larger data set, it would have been possible to use a mean squared error procedure to help eliminate any potential local-minimum error.

Glow-discharge optical emission spectroscopy could potentially be utilised to analyse the layers of the deposited a-Si:H films and determine the composition, if further knowledge of the thin films were required. For our system, we required a higher refractive index than that of silicon nitride and we were able to obtain that.

To use hydrogenated amorphous silicon films for the purpose of photonic biosensing, it is important to have high precision on fabrication parameters. The higher flow rate of 33% hydrogenation, compared to 20% hydrogenation has been shown to decrease the accuracy in film deposition depth (shown figure A.1). The reliability in deposition of 20% a-Si:H, and the minor difference in extinction coefficient and refractive index compared to 33% a-Si:H recommend the 20% film as a basis for the photonic crystal fabrication described in chapter 4.

4. Photonic Crystal Fabrication

4.1 Introduction

Wavelength-scale gratings, also known as photonic crystals, have been used for biosensing purposes since the early 2000s [81,82]. They are scalable to realising multiple binding assays in parallel, they offer high sensitivity and the possibility for large scale production using nanoimprint technology [83–85]. This chapter outlines the fabrication process. The process can be applied to either a 1D- (grating) or a 2D- (array of holes) structure and here is applied to the fabrication of a 2D nanohole array in a hydrogenated amorphous silicon thin film.

4.2 Photonic Crystals

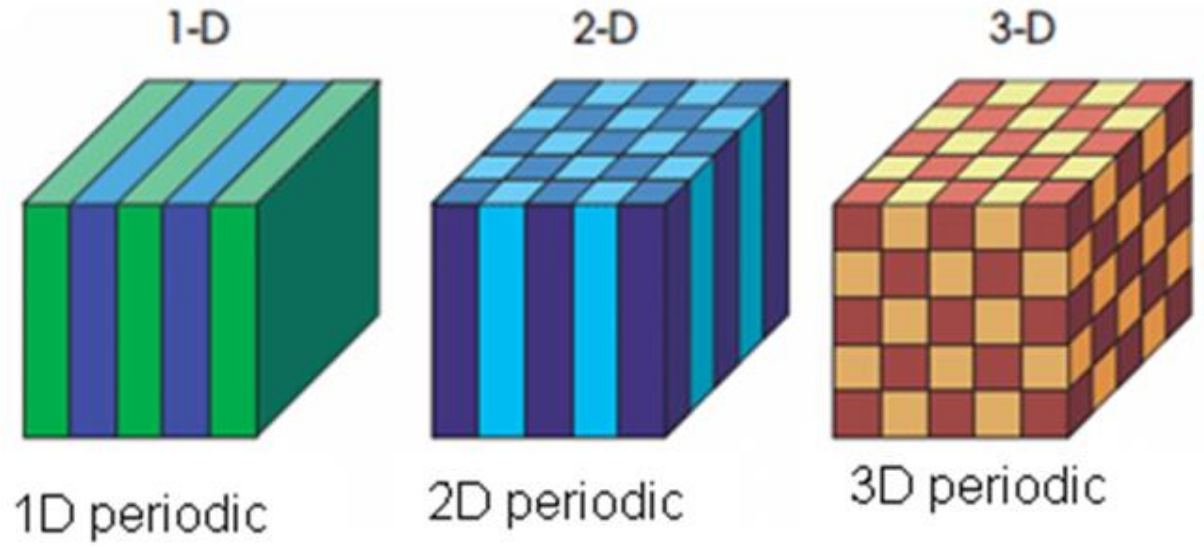

Figure 4.1: *1D, 2D and 3D photonic crystal structures*

Periodic modulation of permittivity in one, two and three dimensions. Dielectric constant represented through structure colour.

Photonic crystals (PhCs) are near-wavelength grating structures with a periodic modulation of the refractive index in one, two, or three dimensions, as illustrated in figure 4.1 [86]. Photonic crystals consist of a periodic structure of high-index material surrounded by low-index material [87]. The effect of the periodic refractive index modulation on an electromagnetic wave is analogous to the effect of a periodic atomic potential on an electron in a crystalline lattice [26], so a PhC is the optical analogue of a periodic system of electric potentials. The optical system is described by Maxwell's equations.

Using appropriate assumptions and boundary conditions, such as linearity, isotropy and periodicity of the refractive index, the solutions of these equations take the form of Bloch waves. The shape of these Bloch waves is an envelope of plane waves modulated by the

periodicity of the medium [86]. The allowed energies at each wave vector then constitute the band diagram, while the corresponding solutions to Maxwell's equations are the modes supported by the structure. The electronic band gap in materials such as semiconductors, referring to a range of energies and directions in which electrons are not allowed to propagate, arises from the restricted nature of these Bloch waves.

4.2.1 Guided Mode Resonance

The gratings referred to in this study support guided-mode resonances (GMRs), which are quasi-guided, or leaky, modes. GMRs confine energy in the slab, which can readily couple to external radiation providing an efficient way of coupling power into and out of the slab.

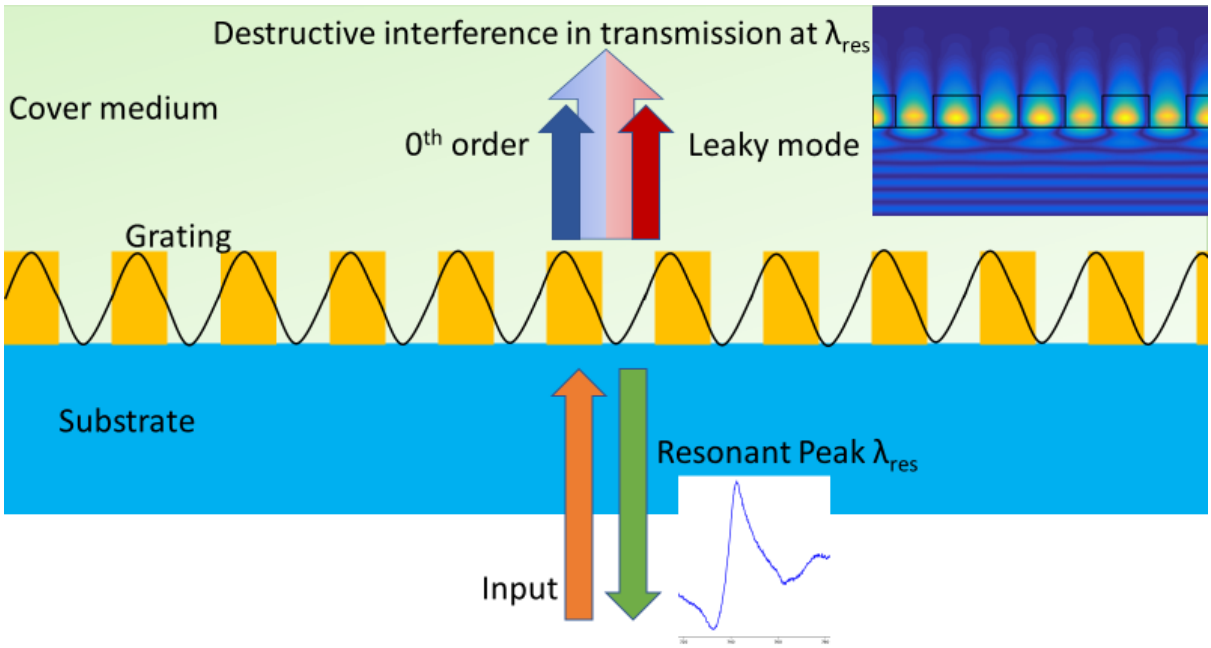

Figure 4.2: *Diagram of guided mode resonance in wavelength-scale grating*

The grating exhibits one diffracted order at normal incidence, which couples into the grating plane and excites leaky modes in the form of a standing wave (black).

GMRs can be excited in visible wavelength-scale gratings and exhibit a sharp peak in the reflection spectrum at normal incidence, shown figure 4.2. The guided mode is sensitive to the refractive index of the cover medium, which provides the mechanism for sensing. A guided more resonance is a specific type of resonance that occurs when the grating layer acts as a waveguiding layer. An electromagnetic field can propagate in the waveguiding layer and the corresponding modes can assume one of two polarisations, i.e. transverse-magnetic (TM) or transverse-electric (TE). For the TM mode, the *magnetic* lines of flux are perpendicular to the waveguide axis, while for a TE mode, it is the *electric* lines of flux that are perpendicular to the waveguide axis [88].

Since the waveguide is not homogenous, the guided mode scatters at each interface giving rise to coherent scattering. The structure is designed as a second order grating and through careful engineering of the grating period, thickness of the waveguide layer, polarisation and the

refractive index of the medium, the phase can be tuned to ensure destructive interference between the transmitted light and the light scattered upward by the leaky mode, again shown figure 4.2. The result is a reflectance peak that can have up to 100% efficiency [89].

$$n_{eff} > n_{inc} \qquad \frac{\lambda_0}{n_{eff}} < a < \frac{\lambda_0}{n_{inc}}$$

Equation 4.1: *Grating resonance conditions*

Resonance occurs in GMRs when the grating meets the conditions shown in equation 4.1, known as the 'near-wavelength' regime. The first condition shows that the effective refractive index of the grating must be higher than the highest refractive index of the surrounding media, which in this case is the silica substrate onto which the grating layer is deposited. The first condition is a requirement for the grating layer to act as a waveguide, and the number of modes the waveguide can support is governed by the layer thickness (t), discussed in chapter 3 as a crucial parameter, and the incident wavelength λ. The second condition states that the grating period (a) must be smaller than the wavelength in the incident medium (silica), but larger than the wavelength in the grating layer.

4.2.2 Photonic Crystals and Bloch Modes

Bloch modes, are distinguished by their k-vector, **k**. They are described by expressing the periodicity of ε(**r**) in terms of a grating vector:

$$\boldsymbol{G} = \frac{2\pi}{a}$$

Equation 4.2: *Grating vector*

Where *a* is the period. The modes within the periodic structure then take the form:

$$\boldsymbol{E_k}(\boldsymbol{r}) = \sum_{m=-\infty}^{\infty} E_m e^{i(\boldsymbol{k}+m\boldsymbol{G})\boldsymbol{r}} \qquad for\ m = \cdots, -2, -1, 0, 1, 2, \ldots$$

Equation 4.3: *Modes within periodic structure*

A plane wave can couple to the Bloch modes of a periodic structure by adding or subtracting integer multiples (m) of a grating vector (**G**) to an incident k-vector. Hence the field boundary conditions, and the conservation of momentum, dictate the phase-matching condition in the direction of periodicity:

$$k_{x,m} = k_{x,inc} - mg \qquad for\ m = \cdots, -2, -1, 0, 1, 2, \ldots$$

Equation 4.4: *Phase-matching condition*

Equation 4.4 dictates all the permitted harmonics in the grating (Florquet condition).

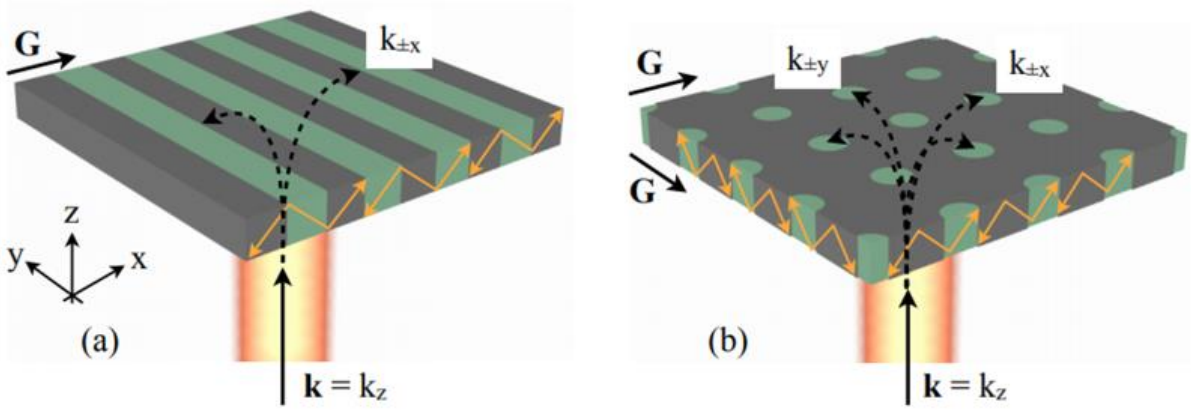

Figure 4.3: *Incident light coupling into a guided-mode resonance*
(a) A one-dimensional grating and (b) a two-dimensional grating. [© IEEE 2015, taken from (Triggs, Resonant Grating Surfaces…)].

Guided mode resonance gratings reported in section 4.2.2 represent a 1D photonic crystal. The nanohole arrays used in the body of work reported here extend this principle to a 2D periodic grating (2D photonic crystal). A comparison between a 1D and 2D grating structure is shown in figure 4.3, showing the additional k-components in y-direction provided by the nanohole array thus directing propagation in both x- and y-directions. It follows that the spatial resolution of the 2D structure should be equal in both x and y, unlike the asymmetric 1D structure.

4.2.3 Nanohole arrays

Having introduced nanohole arrays as a subset of photonic crystals, we now study them in more detail. The key feature we are interested in for the sensing application is the resonance and its response to external refractive index changes. Typical results are shown in fig. 4.4.

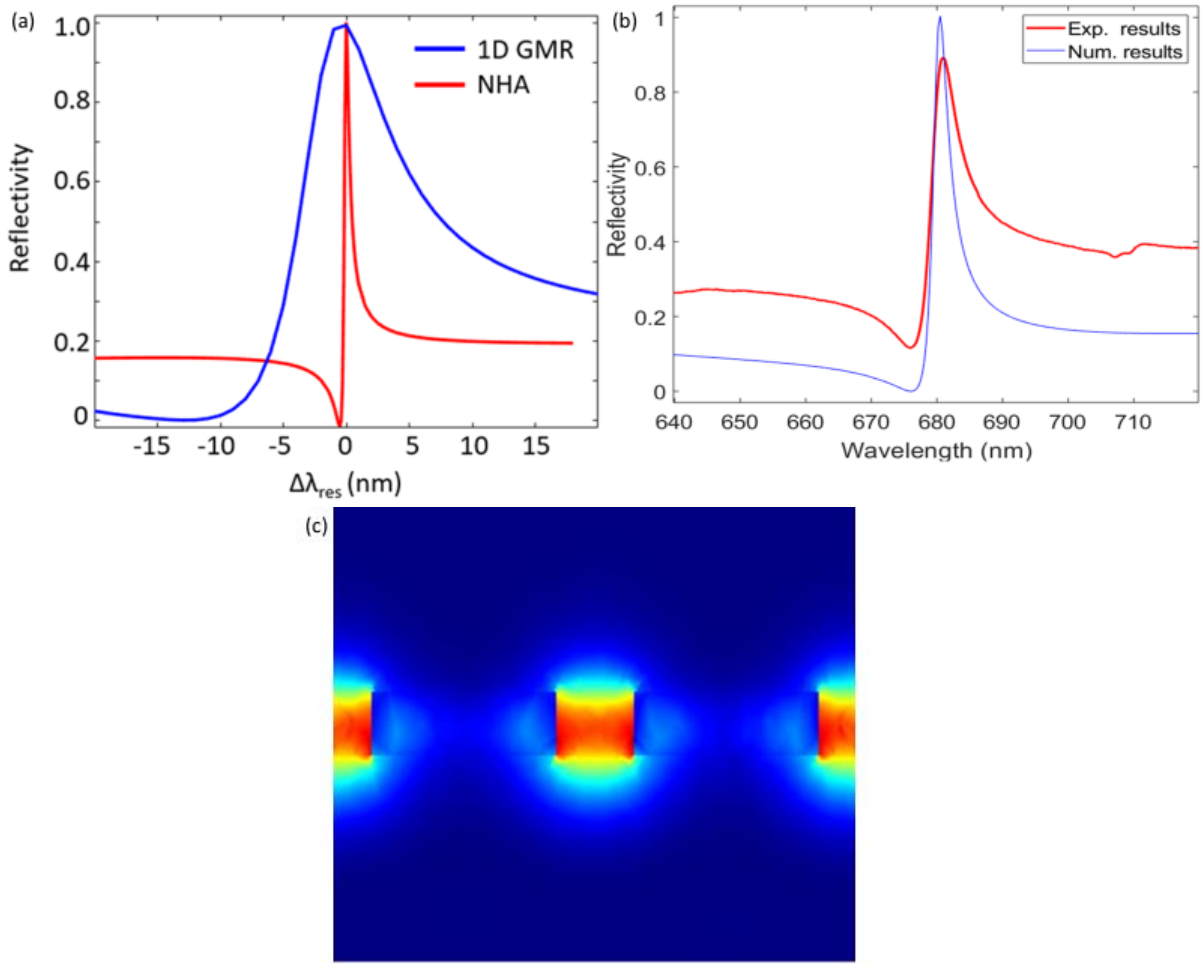

Figure 4.4: *Q-factor, resonance and confinement of a nanohole array*

(a) Simulation of a the Fano resonance typical of a 2D nanohole array (red) in comparison to a 1D GMR (blue). (b) Comparison of the resonance curve in simulation (red) and in experiment (blue). (c) Simulation of the field distribution of the resonant mode.

Overall, the work in collaboration with by my colleague Dr Donato Conteduca has shown that the resonances of 2D nanohole arrays have a higher Q-factor than those of 1-D GMRs and that they are polarisation independent [31], which makes them more advantageous for sensing applications.

4.3 Fabrication

The structures used throughout this work were fabricated in the amorphous silicon film described in chapter 3, with a thickness of 120nm. The silica substrate has a thickness of 500µm.

4.3.1 Rigorous Coupled-Wave Analysis

Rigorous coupled-wave analysis (RCWA) is a Fourier-space semi-analytical method which is typically used to study scattering from periodic dielectric structures, where the structures and fields are represented as a sum of spatial harmonics. We consider the grating, substrate and cover medium as a composition of at least three layers, uniform in the z-axis. The electromagnetic modes in each layer are then calculated and analytically propagated through the layers.

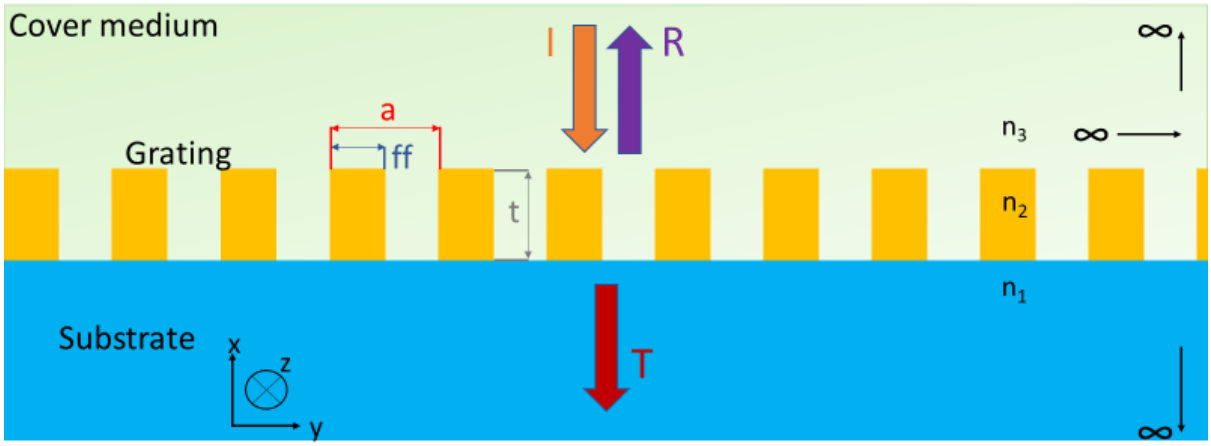

Figure 4.5: *RCWA grating geometry*

The grating is assumed to be infinitely periodic and the cover medium and substrate extend to infinity. The refractive indices (n) of each layer is specified, including real and imaginary parts, along with grating thickness (t), period (a) and fill factor (ff). The geometry this arrangement is shown in figure 4.5. The total electric field in the cover region is given by the sum of the incident wave (I) and the backward-travelling wave (R). In the substrate, the total electric field is given by the sum of all transmitted waves. The total electric field in the grating can be expressed as a Fourier series whereby each Fourier harmonic corresponds to a diffractive order outside the grating layer. The electric fields' boundaries are enforced by the Maxwell equations, while their values may be written as a set of coupled-wave equations, which are numerically solved to give values for the reflected and transmitted orders (R, T). By analysing a series of gratings with varying a, t, ff and the relevant material dispersion relations (see chapter 3), I was able to quickly produce transmission and reflection spectra. This data allowed me to produce grating designs to inform the fabrication process. The RCWA used here was based on a freeware code called S^4 (Stanford Stratified Structure Solver), and all scripts used to sweep wavelength, period, fill factor, thickness and dispersion relations were written by myself.

4.3.2 Fabrication Diagram

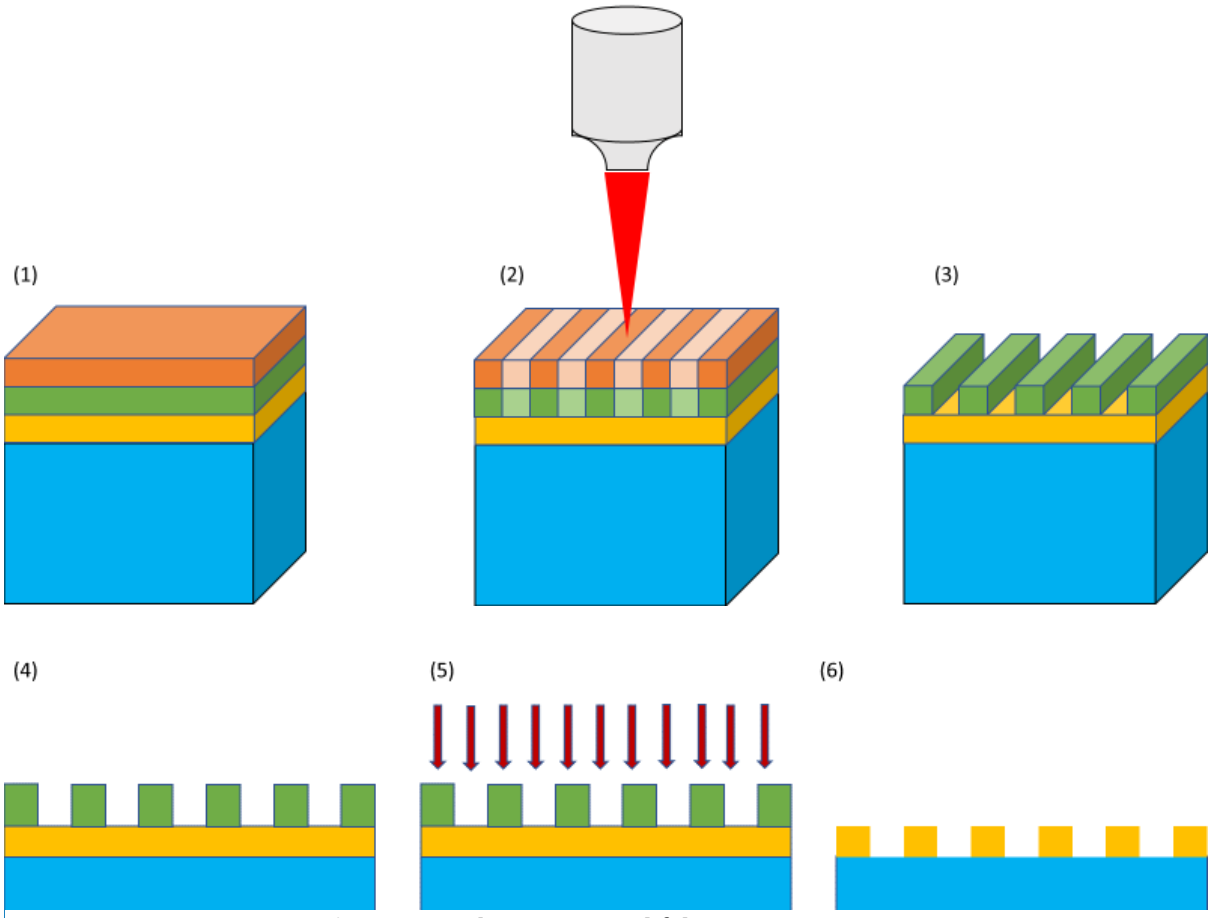

Figure 4.6: *Photonic crystal fabrication steps 1-6*

Key:

- Silica (Blue)
- Hydrogenated Amorphous Silicon (Yellow)
- AR-P 6200.13 (Green)
- AR-PC 5090 (Orange)

4.3.3 Substrate Preparation (Step 1)

The silica substrate is cleaned thoroughly to remove any imperfections such as dust or biological material on the surface. Following the deposition of a-Si:H, the sample is cleaned thoroughly again in acetone and isopropanol using sonication for 10 minutes.

A flat and even layer of a photoresist is applied using a spin coater, which allows the resist thickness to be controlled with spin speed and spin duration to a precision of tens of nanometres. We use AR-P 6200.13 positive electron beam (e-beam) resist [90], which has a high sensitivity to electron exposure and a good resistance to plasma etching. This resist is spun on the device at 5000rpm for two minutes. The resist is then baked at 150˚C for one minute. A

subsequent layer of AR-PC 5090 [91] is applied at 2000rpm for one minute to reduce sample charging during electron beam lithography. The AR-PC layer is baked at 90˚C for two minutes.

4.3.4 Electron Beam Lithography (Step 2)

Electron beam lithography (EBL) is a technique for creating nanostructures with a highly focussed electron beam. Due to the short wavelength of the high-energy electrons, patterns with a resolution of 10-20 nm can be achieved. The 2D periodic pattern was created using CAD software compatible with the EBL system allowing the 50keV e-beam to transfer the structures into the resist [92]. The base dose used in this work was 150μC/cm^2. The base dose can be increased with a scaling factor known as dose factor (DF). A larger dose factor translates to a larger number of electrons impacting on the sample, which leads to a greater effect on breaking down the polymer photoresist. In general, this leads to a deeper exposure within the resist, but it can also lead to a widening of features.

4.3.5 Development (Step 3 & 4)

Post electron beam exposure, the charge dissipation layer (AR-PC) must be removed before the pattern transfer can be completed. The charge dissipation layer is removed using deionised water (DI). A two-minute submersion in DI followed by DI rinses is sufficient to remove this layer, leaving the photoresist on the sample surface. The areas modified by exposure to the e-beam are removed using xylene for two and a half minutes. The process is known as development, and post-development the sample is submerged in isopropanol to remove any DI or xylene from the surface before etching can begin.

4.3.6 Reactive Ion Etching (Step 5)

To transfer the pattern from the photoresist into the hydrogenated amorphous silicon layer, we use a process known as reactive ion etching (RIE). RIE is a plasma etch technology, in which chemically reactive ions are accelerated towards a substrate to remove material as a combination of chemical and physical etching.

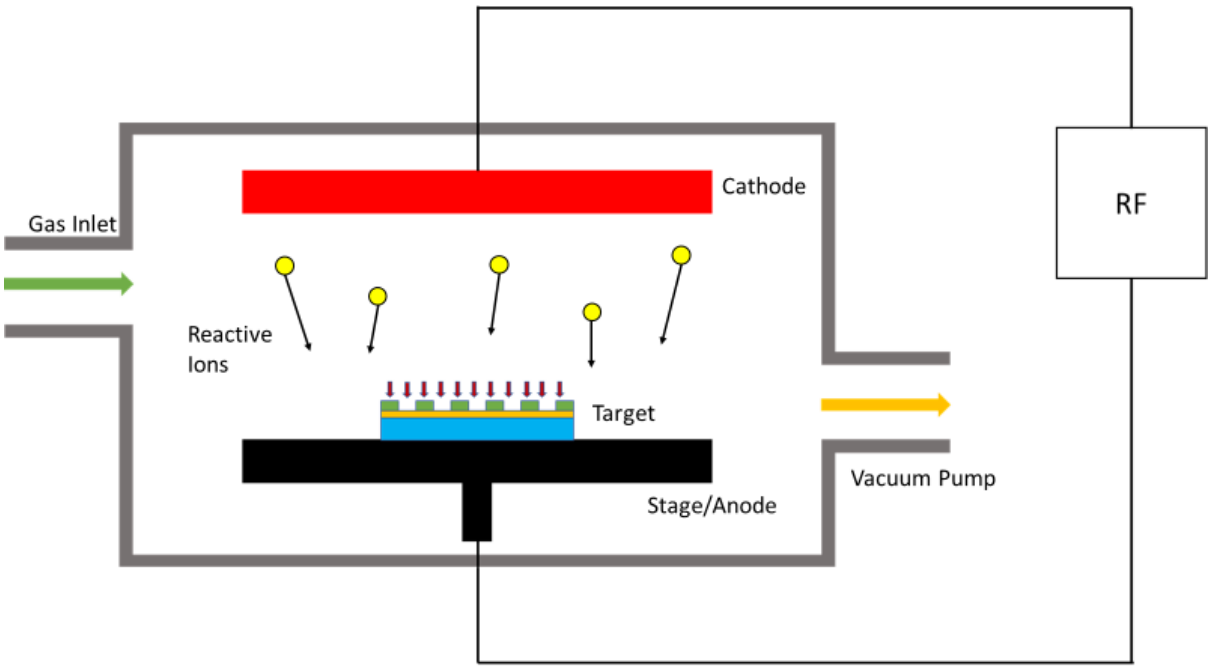

Figure 4.7: *Reactive ion etching chamber*

The plasma is initiated by the application of a 13.56MHz RF powered electrode (cathode). The electric field ionises the gas molecules to create the plasma. A DC bias voltage forms on the bottom of the RF-powered electrode, extracting ions from the 'bulk' plasma, thus the DC bias contributes to the directionality of etching the sample.

Using a chamber similar to that shown in figure 4.7, I used a mixture of fluoroform (CHF_3) and sulphur hexafluoride (SF_6) at a ratio of 1.16:1, respectively, with a DC power of 24W to remove the photoresist and etch a periodic array of holes into the a-Si:H layer. An etch time of 30 seconds is sufficient to etch the desired pattern into the a-Si:H layer.

4.3.7 Final Clean (Step 6)

The photoresist layer is much thicker than the a-Si:H layer, and therefore some photoresist remains on the surface after the etching process. To remove this layer and clean the entire device thoroughly, I conduct a cleaning process; First, a five minutes clean with 1165 MICROPOSIT remover [93] is used . The device is then cleaned in acetone and isopropanol for five minutes each. Low speed sonication is applied throughout this process.

4.4 Fabrication Results

Scanning electron microscopy (SEM) is a well-known technique for obtaining surface topography information. Like the e-beam process, the shorter wavelength of electrons, compared to photons in the visible spectrum, allows for better resolution, i.e. down to the sub-10 nanometre scale. As the beam of electrons interact with the sample, it produces secondary and backscattered electrons. These signals are collected to form an image [94]. Since the amorphous silicon is placed on a (non-conducting) silica substrate, the sample charging issue that occurs in EBL also occurs in the SEM. A layer of AR-PC 5090 is reapplied to the sample prior to SEM inspection. The sample presented in figure 4.8 was fabricated with a period of 520nm and a hole radius of 90nm and highlights the accuracy of the fabrication process. All fabricated samples during this body of work are examined using SEM to ensure that the input parameters translate into desired results.

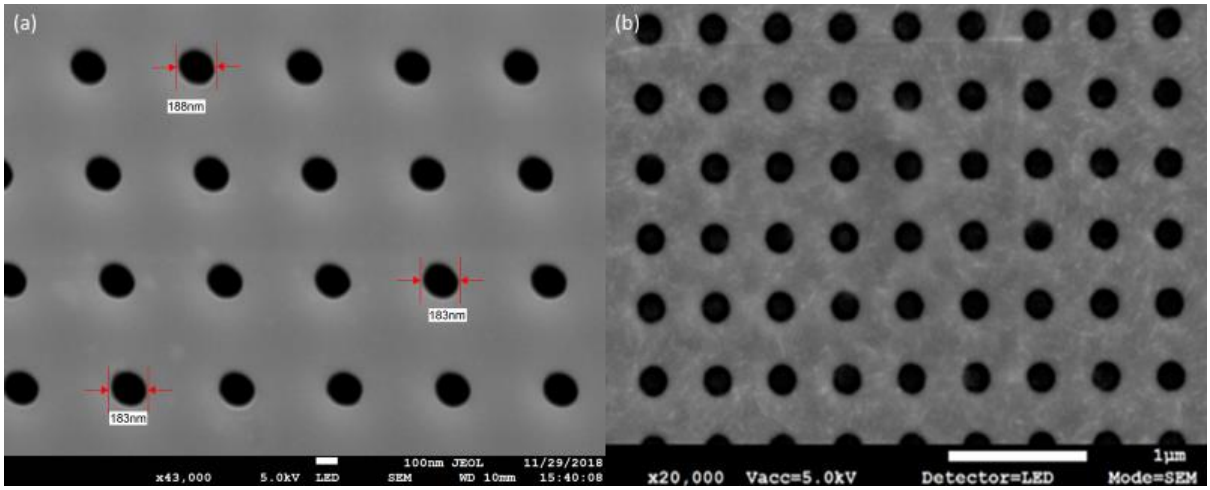

Figure 4.8: *SEM images of a periodic square array of holes*

SEM image of 2D photonic crystal using built-in software tools to measure (a) Hole diameter and image capturing to see (b) structure quality.

4.5 Chapter 4 Conclusion

In summary, chapter 4 has presented the fabrication process used to create 1D and 2D periodic patterns in hydrogenated amorphous silicon, also known as photonic crystals or guided mode resonance structures. The fabrication process allows for multiple-sample production with electron beam lithography and can be performed on a much larger scale if nano-imprint technology were to be used. The fabrication process is finely tuned, and the resulting sample quality is examined using scanning electron microscopy. Rigorous coupled-wave analysis supports the design and reduces the need for physical prototyping by allowing for simulated parameter variation.

5. Measuring Concentration of Analytes

5.1 Introduction

Chapter 5 combines all the steps covered in chapters 2 to 4 to create a point of care measurement device capable of measuring and thermally pre-concentrating analytes. Optical measurements are taken in reflection using a CCD spectrometer to measure intensity vs wavelength data and determine a resonant wavelength shift over time. This chapter also covers the design and fabrication of a system holder, to package together the paper channel, Kanthal heater and PhC biosensor as a separate "unit" that can easily be affixed to an optical setup (such as figure 5.1).

5.2 Experimental Setup

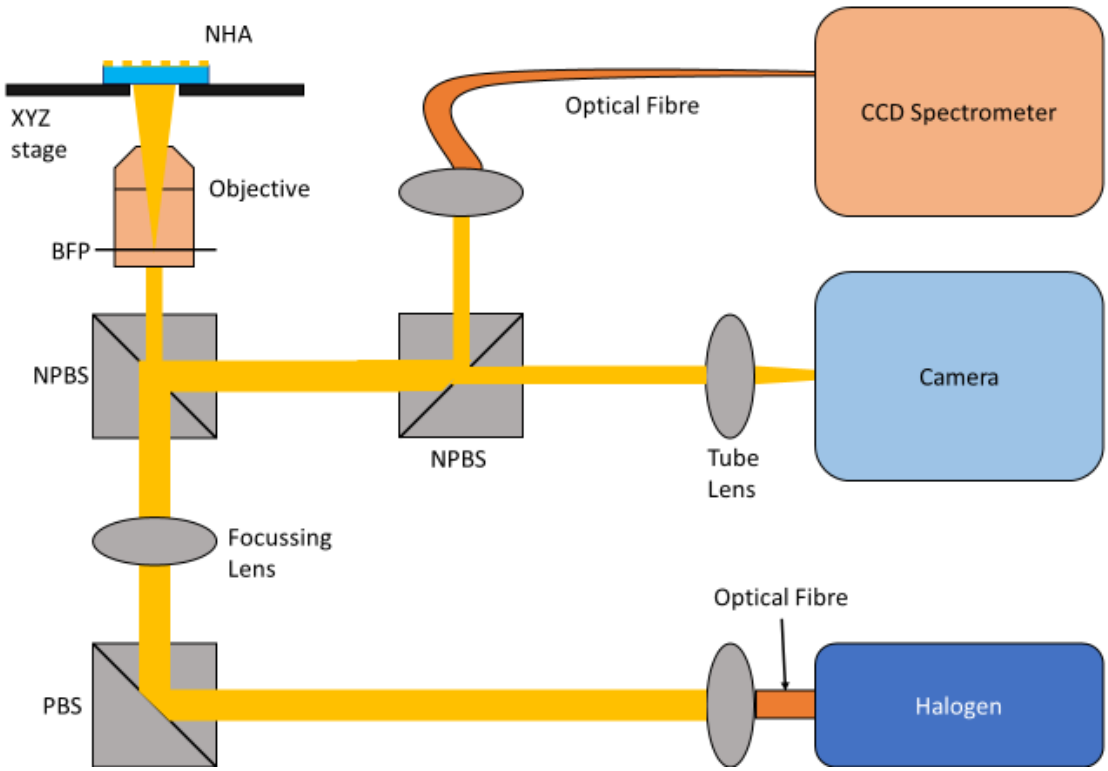

Figure 5.1: *Schematic diagram of experimental setup for measurements in reflection*

White light from a halogen source passes through a polarising beam splitter (PBD), a focussing lens and a non-polarising beam splitter (NBS), where it is focussed on the back focal plane (BFP) of the objective. Upon reflection from the nanohole array (NHA), the light passes back though the NPBS, where it is split for measurement with a charge-coupled device (CCD) spectrometer and the camera for alignment.

The experimental setup shown in figure 5.1 was used to measure the analyte concentration by a reflection measurement of the resonance wavelength as a function of time. The resonant wavelength is highly dependent on the local refractive index in the cover medium (chapter 4), which is altered by the presence of analytes. The measurement allows for the monitoring of the peak but lacks any spatial information. A camera is used to visually align the setup prior to and during the measurements.

5.2.1 Device Holder

In addition to the experimental setup shown in figure 5.1, an important aspect of using resonant gratings as biosensors is analyte delivery. The analyte is typically delivered using microfluidics, which is realised in polydimethylsiloxane (PDMS) and mounted onto the sensor chip [26]. I developed a system capable of handling solutions, sensors, and heating elements able to compete with microfluidic systems. To create this system, I used polymethyl methacrylate (PMMA) resin on a 3D printer. The 3D printer allows for fast prototyping with high resolution and is available with clear resins compatible with optical components.

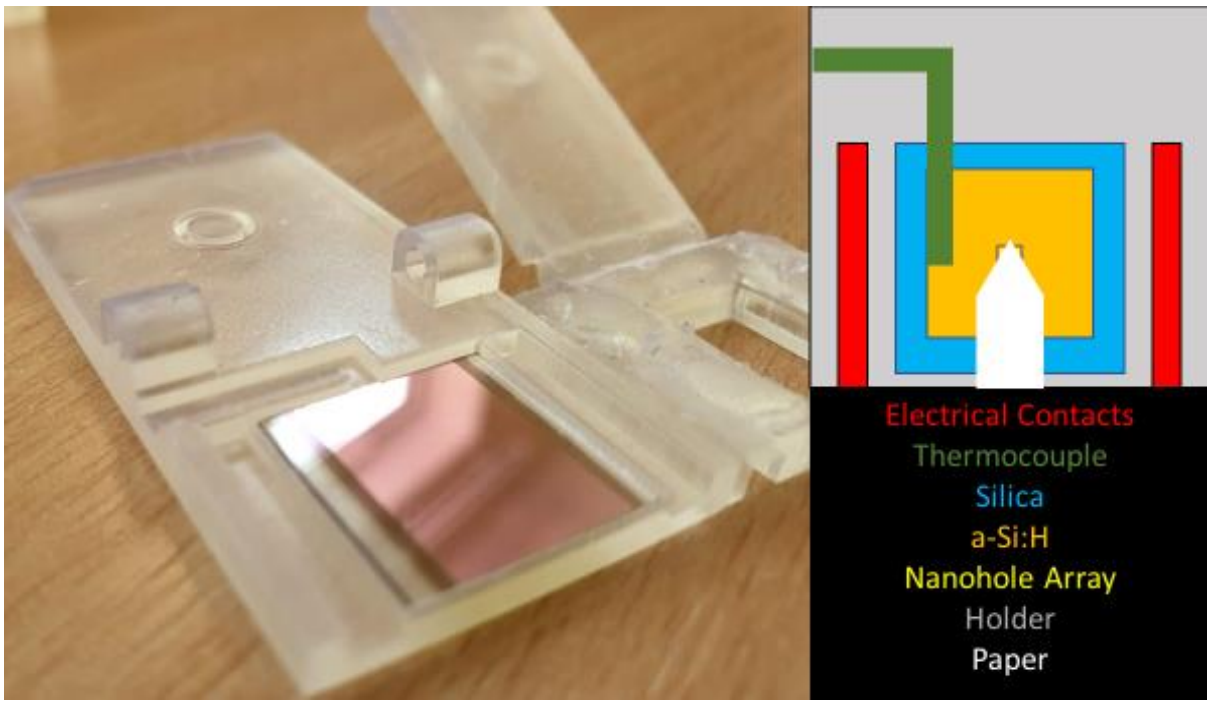

Figure 5.2: *"Clothes peg" style device holder*

Features include a recess for sensor substrate with open space underneath to allow measurements in reflection, recess for electrical contacts for Kanthal mesh, recess for thermocouple to monitor temperature, spring-and-locking-pin clamping mechanism.

The first iteration of the system featured a strong spring clamp to maintain contact between the Kanthal mesh and the electrical contacts. The Kanthal heater, at this stage, sits above the sensor chip, and the temperature is monitored using a thermocouple, as observed in figure 5.2.

While the “clothes peg” iteration enables a good contact between the heating element and the electrical contacts, it did not include a paper-reservoir setup which proved impractical during early experiments as, if over-saturation of the paper occurred, the liquid sample would leak out of the paper and onto optical or electrical components. To improve on the “clothes peg” system, I removed the upper surface and added a sample reservoir to allow the paper channel to draw a solution naturally and without force from a pipette, which can lead to flooding the system. I then narrowed the electrical connector recesses to allow the Kanthal mesh to be fixed between the holder and the connector, shown figure 5.3.

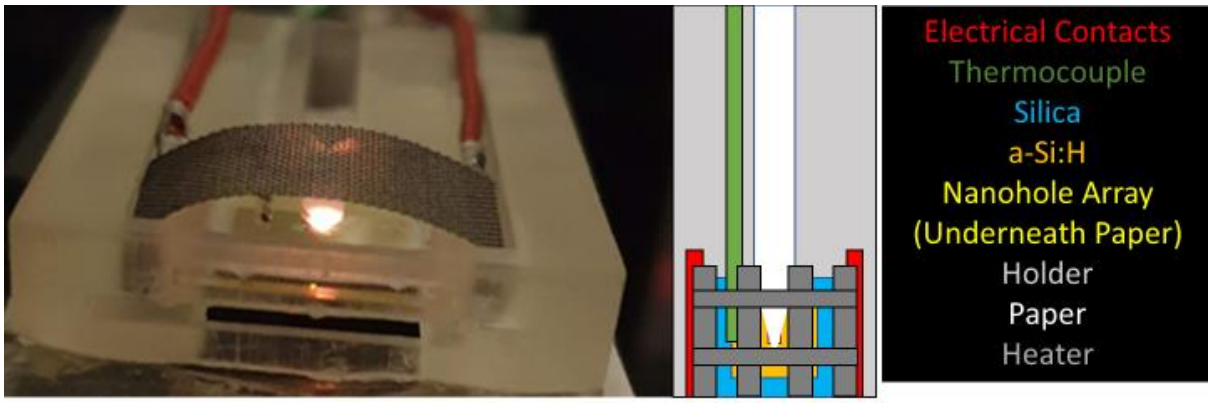

Figure 5.3: *Reservoir system*

Features include a reservoir channel for the paper channel, slot for biosensor with cut-out underside to allow for measurements in reflection, in-line electrical connectors to minimise system footprint, top-mounted Kanthal mesh.

Throughout all system holder development steps, optical measurements using the sensor are taken in reflection as shown figure 5.1. The optical path illuminates the sensor from underneath (all schematic diagrams are illustrated from a top-down view). The sensor is mounted on a PMMA ridge, which leaves a 14x14mm square open underneath through which the light can pass, as shown figure 5.4.

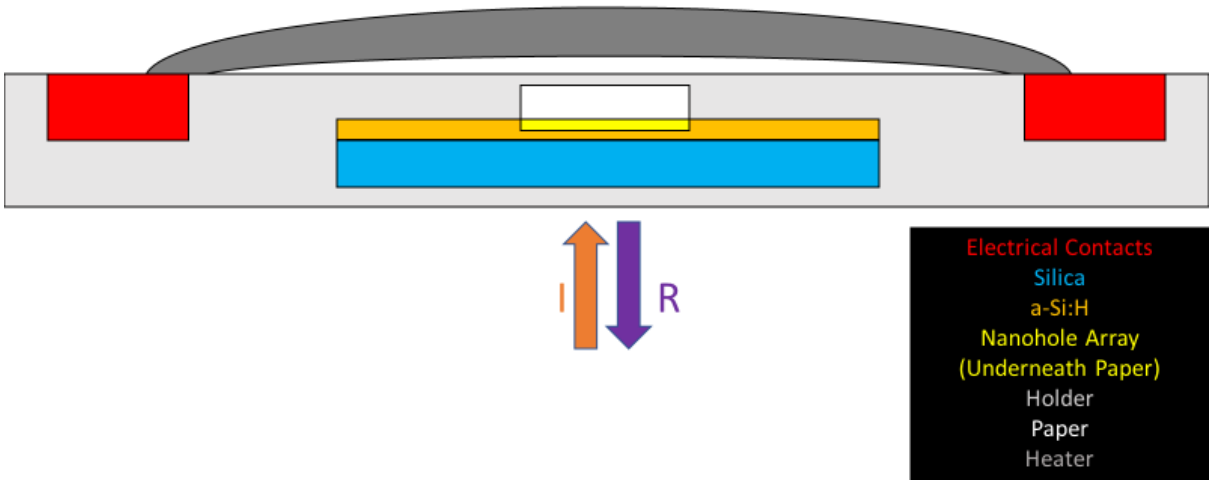

Figure 5.4: *Optical path interaction with holder*

Once it had been discovered that the heating element was more effective when placed underneath the biosensor, the device holder was adjusted accordingly. Moving the heating element underneath the biosensor mimicked the clamping effect observed in the "clothes peg" iteration, thus fixing the heater in place.

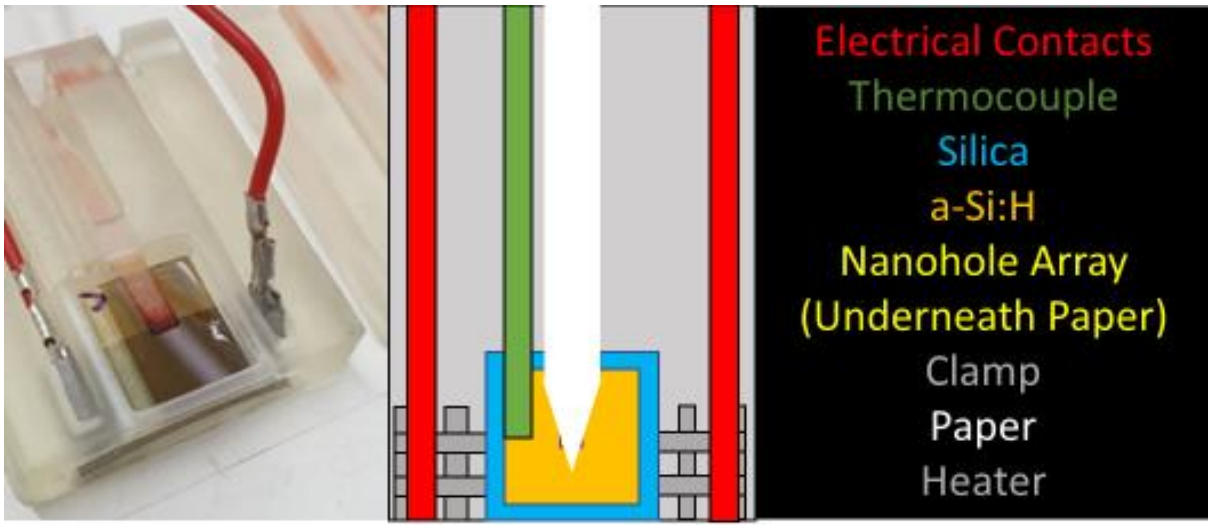

Figure 5.5: *Holder with Kanthal heater underneath*

Features include a reservoir-paper channel, biosensor slot allowing for measurements in reflection, in-line electrical connectors, under-sensor-mounted Kanthal heater.

The ultimate goal of this work is to increase the sensitivity of protein-binding measurements. Such experiments require a washing step, which is easily realised with the flow channels in a PDMS fluidic system, but much more difficult to realise in a paper-based system. As a case in point, the system shown in figure 5.5 does not allow for washing, due to the paper channel ending above the sensor chip (the area requiring a wash). It follows that it would be desirable for our system to include an out-flow area.

To this end, I extended the PMMA base to include a sample pad paper area, which has a greater absorbance than chromatography paper. I added a second heater, which can operate at a much higher temperature than the first heater; the higher temperature allows for a higher evaporation rate and therefore a higher liquid flow. I added an inlet for a microfluidic pump at the reservoir end of the paper channel, which does not pump directly onto the paper but instead allows the reservoir to be topped up gradually. The pump is useful for washing steps that tend to require 1-2mL of a washing solution, such as phosphate-buffered saline (PBS), while maintaining a small reservoir (300µL) and, therefore, a small holder footprint. These additions are shown in figure 5.6.

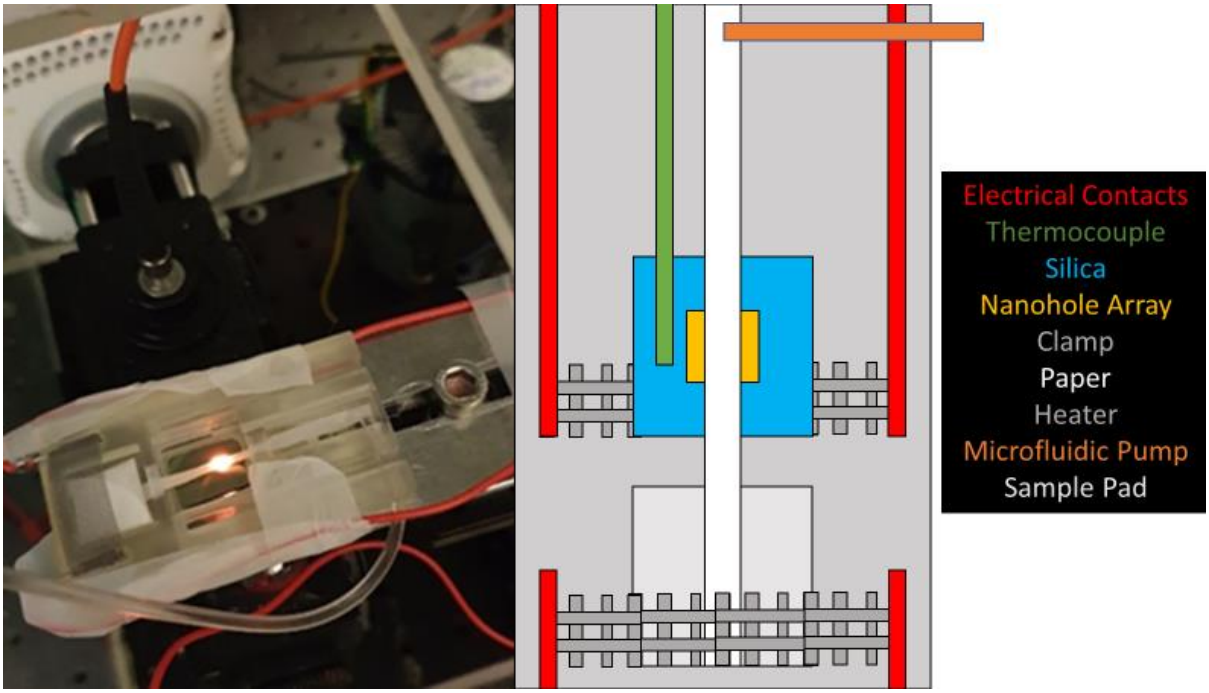

Figure 5.6: *Reservoir-wash system*

Features include a reservoir-paper channel, biosensor slot allow for measurements in reflection, in-line electrical connectors, under-sensor-mounted Kanthal heater, microfluidic pump inlet, extended paper channel with sample pad to absorb wash steps, second heating element to evaporate washes.

5.3 Experimental Results

The nanohole arrays discussed in chapter 4 measure a resonant wavelength which is dependent on the local refractive index in the cover medium as shown in figure 4.5. The corresponding resonance peak has a Fano line shape. A Fano resonance has an asymmetric profile caused by the interference between the local resonance of the GMR and the extended Fabry-Perot resonance of the thin film [95]. The basic principle of the device is to measure the resonant wavelength as a function of time and to translate that information into a concentration of analyte. Before this can be done, the nanohole array needs to be calibrated.

5.3.1 Bulk Sensitivity

The bulk sensitivity of a biosensor is measured using solutions of known refractive index, which are first determined with a commercial refractometer. I used a volume of 100µL to obtain the refractive index values for DI water, isopropanol, and large concentrations (1-4 molar) of sodium-, lithium- and potassium- chloride, and glucose. I then applied these solutions to the sensor chip and measured the corresponding shift in resonant wavelength.

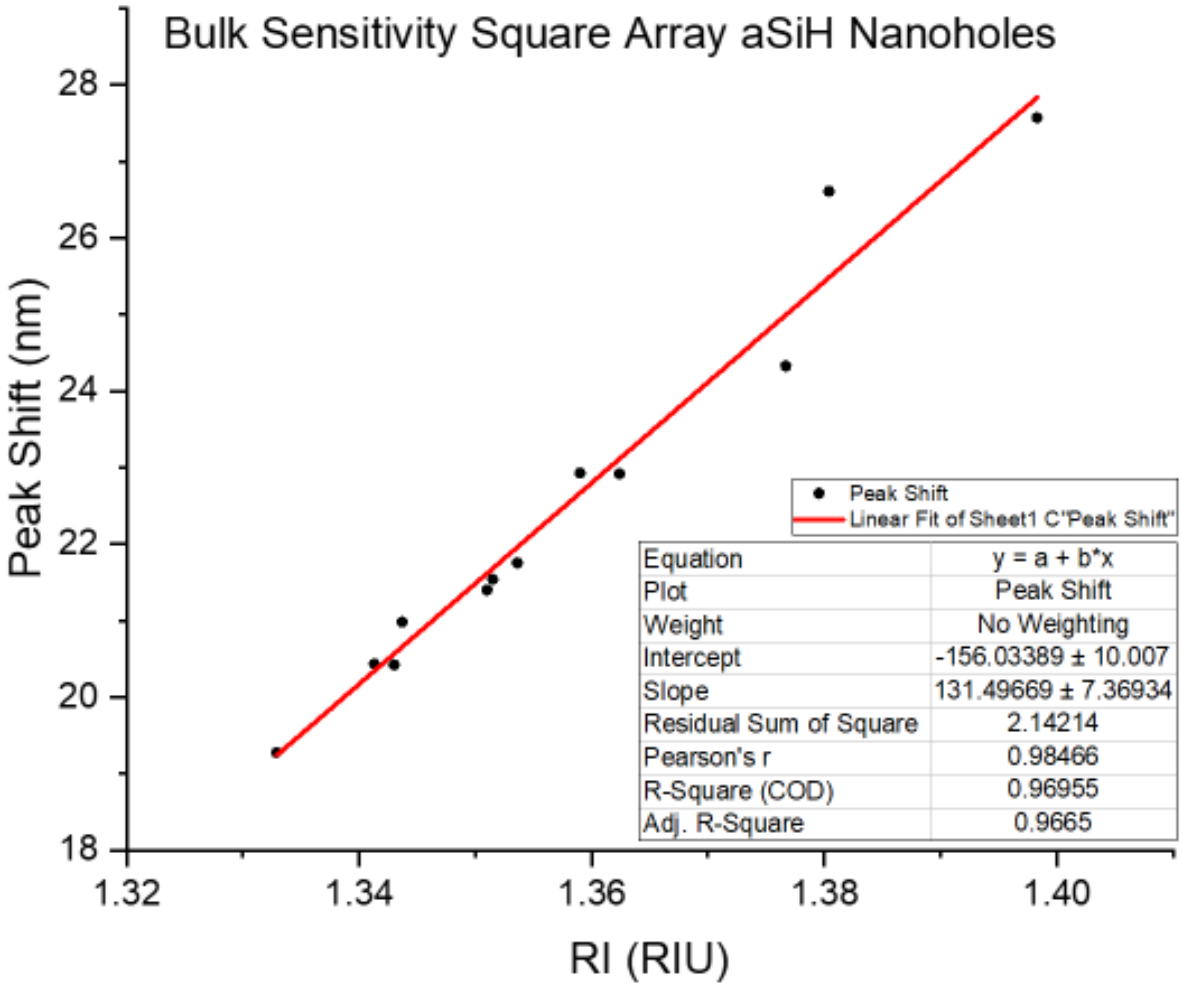

Figure 5.7: *Bulk sensitivity for a nanohole array*

Obtained by measuring the resonant wavelength of different solutions of known refractive index.

Plotting this wavelength shift against the refractive index, as shown in figure 5.7, yields the bulk sensitivity. Accordingly, the bulk sensitivity of the nanohole array shown in figure 5.7 is (131±7) nm/RIU (refractive index unit).

5.3.2 Analytes on Paper

We can now proceed towards measuring analytes with the paper setup. The solution delivery method was either to pipet 300µL of a solution into the reservoir shown in figure 5.5, or to use a microfluidic pump for delivering a solution at 300µL/hr, shown figure 5.6. The total volume in both instances (300µL) is a direct result of the available reservoir volume and it correlates with the average evaporation speed at the heater location, that was determined experimentally. Prior to introducing the solution, the heater was switched on and the temperature was monitored with a k-type thermocouple. In parallel, the spectrum was captured automatically, typically ever 1-2 seconds. With solutions of a fixed volume, the experiment was allowed to run until the paper had dried. With pump-fed solutions, the experiment was allowed to run until a peak shift greater than that of air to DI water was observed, in post processing all concentrations are plotted with respect to DI water.

I used two specific analytes in this body of work, sodium chloride and glucose. Sodium chloride is clinically very relevant as an early indicator of Alzheimer's disease [96], while glucose has clinical relevance in diabetes patients and blood sugar monitoring. Solutions were prepared in concentrations between 1 Molar (M) and 1pM in steps of 1000 for both analytes dissolved in DI water. Pre-experiment cleaning of the biosensor involved a DI clean to absorb any solute present on the surface, and an isopropanol rinse to remove any water or dust.

The molar weights of sodium chloride and glucose are 58.44g/mol and 180.16g/mol, respectively [97].

During this section analyte concentrations are measured as a resonance shift, denoted as peak shift. All peak shifts are plotted relative to DI water as the cover medium and hence DI water is shown as a peak shift of 0nm.

5.3.3 Data Processing

The spectral data was collected with a CCD spectrometer as shown in figure 5.1. The data is collected as a set of intensity vs wavelength values and, using a python script I wrote, I then determined the peak wavelength by fitting a Fano profile of the form:

$$\sigma = \frac{(\varepsilon + q)^2}{(\varepsilon^2 + 1)}$$

Equation 5.1*: Fano profile*

Where σ is the Fano line shape, ε is a reduced energy defined by the peak shape and q is the Fano shape parameter. Where ε is defined as:

$$\varepsilon = 2\left(\frac{E - E_F}{\Gamma}\right)$$

Equation 5.2: *Reduced energy*

Where E_f is the resonant energy, and Γ is the width of the resonance [95]. I used Python functions to optimise the fitting parameters and to accurately determine the resonant wavelength as a function of time. This method allows me to track the peak wavelength and to measure the resonance shift. Using the known sensitivity of the device, I can then calculate the refractive index shift thus inferring the concentration of analyte present.

5.3.4 Effect of Heater on Resonance

As a further calibration step, I need to establish whether the change in operating temperature brought about by the heater has an impact on the resonance, in particular because the thermo-optic effect of silicon is well documented [98–100]; for example, crystalline silicon has a thermo-optic coefficient of $1.86e^{-4}K^{-1}$ [101], and amorphous silicon $2.4e^{-4}K^{-1}$ [102].

It has been reported with other photonic crystal substrates, that operating temperature can affect the resonance response. In some instances the temperature is used to tune the resonance wavelength [103]. To determine if the same effect applies to our 2D photonic crystal, I measured the resonant wavelength as a function of film temperature. I used the experimental setup shown in figure 5.1, and adjusted input power to the Kanthal heater thus increasing the temperature of the a-Si:H substrate. Resonant wavelength was measured at one second intervals. The temperature of the a-Si:H film was increased gradually by slowly increasing the supplied power to the Kanthal mesh heater and monitored with a thermocouple placed on the a-Si:H film surface.

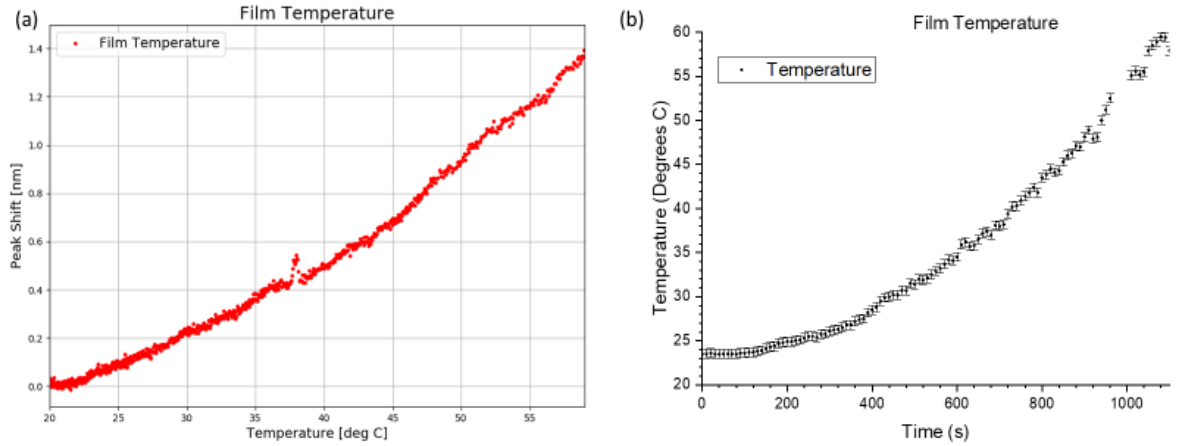

Figure 5.8: *(a) Resonant wavelength shift of nanohole array as a function of a-Si:H film temperature. (b) a-Si:H film temperature as a function of time.*

The gradient of figure 5.8(a) yields the variation in peak resonance with temperature of $\Delta\lambda_r/\Delta T = 0.003$ nmK^{-1} for a-Si:H. Assuming the system to be linear and the proportionality $\frac{\Delta\lambda}{\lambda} = \frac{\Delta n}{n}$, this value yields a thermo-optic coefficient for the resonant mode of $1.26e^{-5}K^{-1}$, which is closer to literature values of silica ($1e^{-5}K^{-1}$) [101]. [which should be lower because the resonant mode only partially overlaps with the material]. Our system operates in the 35-50˚C range where we observe a shift of less than 1nm, so by pre-heating the substrate and maintaining the temperature within $\Delta T \approx 1$ K throughout the experiment, the thermal effect on the substrate can be considered negligible. The corresponding temperature as a function of time measurement

can be seen in figure 5.8(b). Temperature of the a-Si:H film increased gradually and assumed to be evenly distributed across the surface.

5.3.5 Heater Location

To consolidate the hypothesis that placing the Kanthal heater underneath the sensor allows for a greater level of concentration at a faster rate, I compared the two heater locations against the configuration without heater for a 1M concentration of sodium chloride solution. The experiments were conducted over the same length of time, and the nanohole array temperature was maintained at 40˚C in both cases and the same volume of solution (300µL) was used in each experiment.

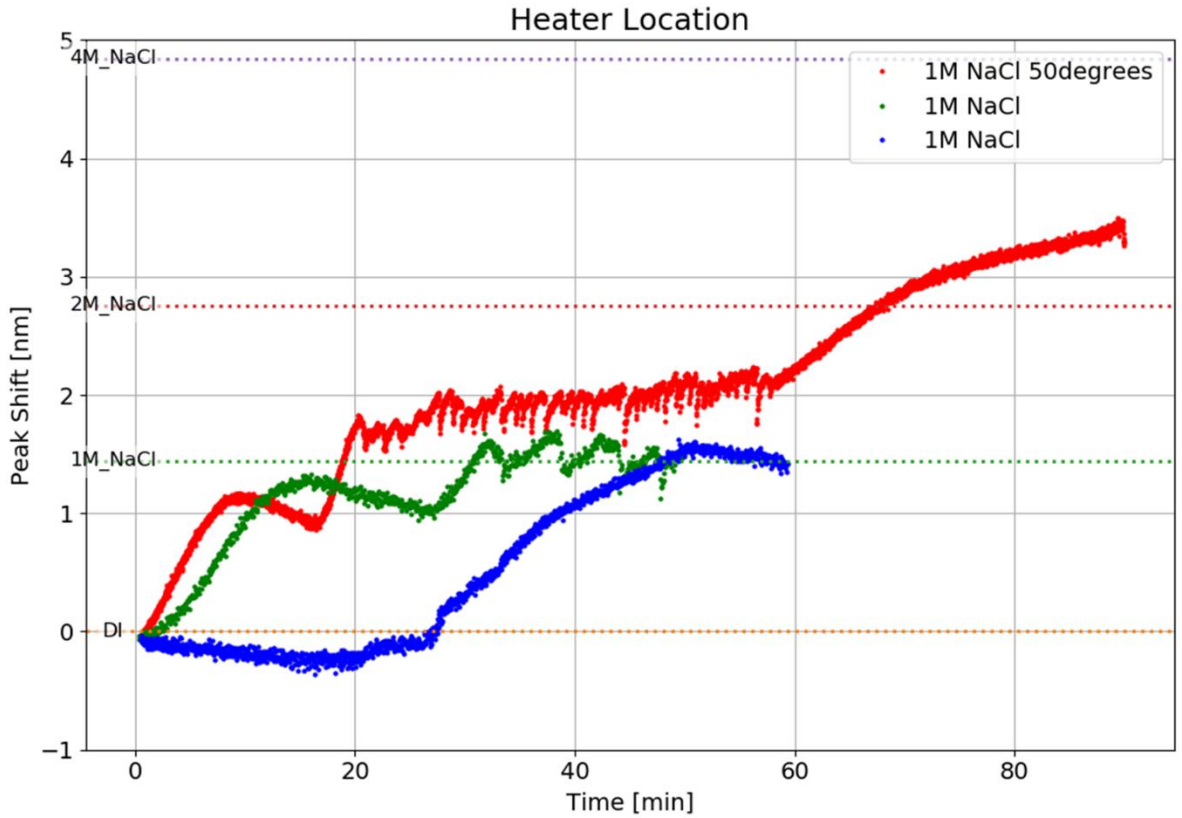

Figure 5.9: *Wavelength shift comparison for heater location*

Wavelength shift for a fixed sodium chloride concentration as a function of time for (green) no heater (blue) Kanthal heater on top of the sensor (red) Kanthal heater underneath the sensor.

The measurement showed a distinct difference. Placing the heater underneath the sensor showed a much stronger effect than placing it on top of the sensor. Similarly, when placing the heater on top of the sensor, the solution does concentrate faster than without heating.

The benefits of placing the heater underneath the sensor extend beyond the greater rate of concentration observes in figure 5.9. With much smaller sodium chloride concentrations (1µM and lower) no shift was observed with the heater above the sensor, which is believed to be a direct of the effect shown in figures 2.14 and 2.15. Point of care (POC) devices, chapter 1, such

as this system should be as portable and simple to use as possible. With the heater located underneath the sensor, it is possible to electrically connect and simultaneously clamp the heater in place and the overall size of the device is reduced as the heater doesn't protrude from the holder. Porous materials deform when they dry, this process often involves shrinking, bending and, in some cases, cracking [104]. With the heater above the paper, we found it was more likely to bend while drying and thus pull the paper channel away from the sensor. With the heater below the sensor, any drying that occurred down the paper channel only assisted in maintaining contact between sensor and paper. The resonance within the sensor is only affected by the cover medium close to the surface. Therefore, removing the paper even slightly from the sensor prevents measurements.

5.3.6 Sodium Chloride

Using the experimental setup and pipetting procedure outlined in section 5.2, 5.3 respectively, I measured the peak resonance as a function of time for a 1M solution of sodium chloride. Measurements were taken with the Kanthal heater underneath the PhC and without a heat source.

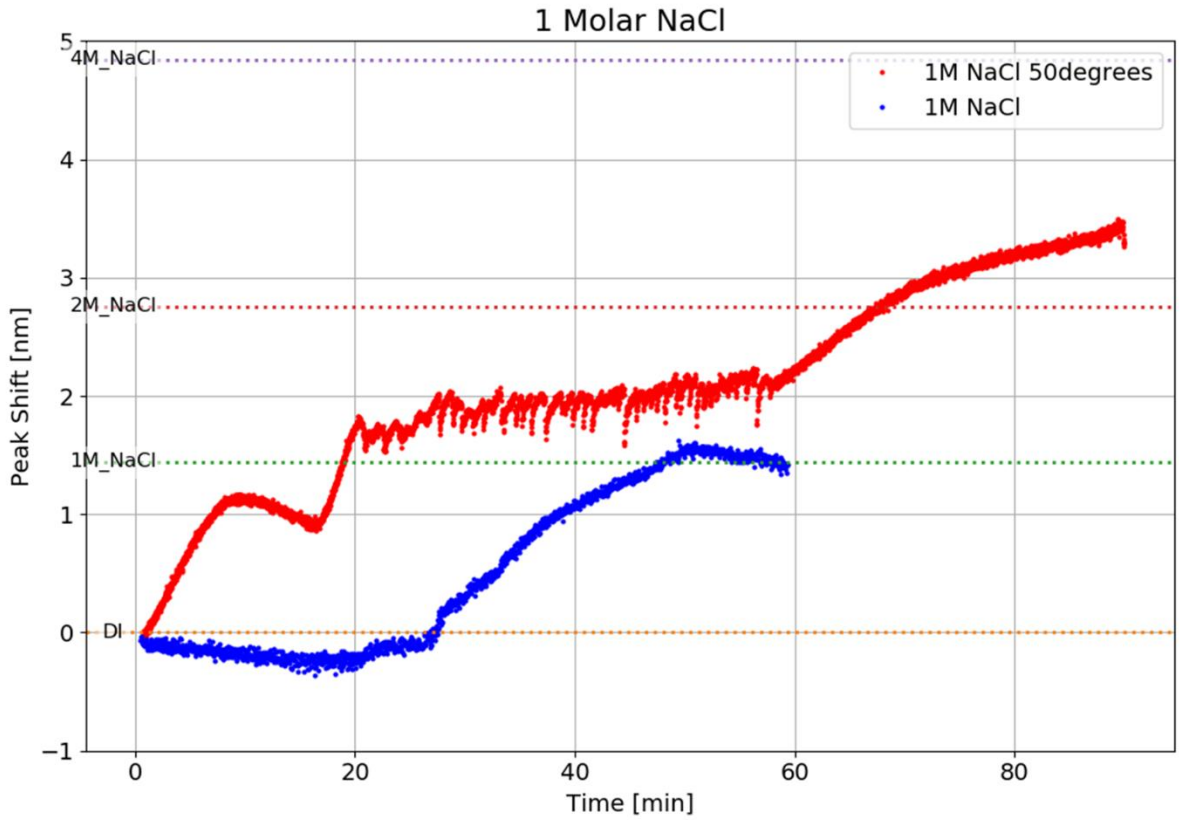

Figure 5.10: *1 molar sodium chloride*

Thermal preconcentration of 1 molar sodium chloride (red) compared to measurement without heater for a 1 molar solution of sodium chloride (blue).

I measured the thermal preconcentration of a one molar sodium chloride solution and compared it to the same solution without the use of the heater (figure 5.10). We observe a wavelength

shift which is more than 2 times stronger, indicating that heating achieves a large concentration difference. The thermal preconcentration shown in figure 5.10, in red, highlights a jagged line-shape, between 20 and 60 minutes, observed in some of the other thermal preconcentration experiments. It is believed that this is, in part, a cause of minor temperature fluctuations in the room affecting the heating temperature of the sensor. The shape is potentially a result of re-absorption of the solute due to a net flow-flux towards the sensor, which is increased by heating the paper channel in the thermal preconcentration measurements. The dip observed at approximately 20 minutes could be either another indicator of a temperature change, or a backflow of the solution as the system equilibrates prior to thermal concentration. Having established successful operation and clearly demonstrated the principle of preconcentration, I moved on to investigating smaller concentrations. The result for a 1mM solution is shown in fig. 5.11.

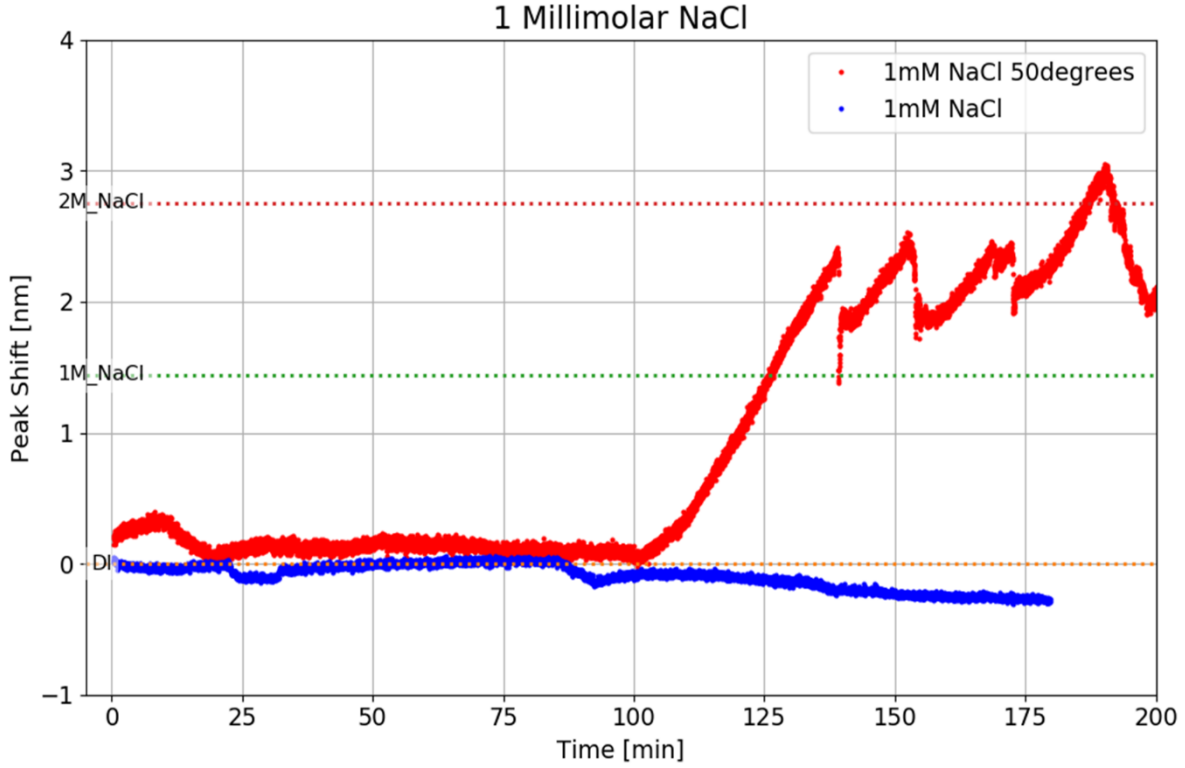

Figure 5.11: *1 millimolar sodium chloride*

Thermal preconcentration of 1 millimolar sodium chloride (red) compared with no temperature gradient 1 millimolar sodium chloride (blue).

One millimolar of sodium chloride, as shown figure 5.11 in blue, is undistinguishable from deionised (DI) water with both a digital refractometer and the nanohole array in our system. Thermal preconcentration at 50˚C produced a measured concentration a factor 10^3 higher than that in the solution. Spikes in the peak shift between 125 and 200 minutes are believed to be caused by re-dissolving of salt as more solution is drawn toward the PhC. The results of 1pM solution is shown in figure 5.12.

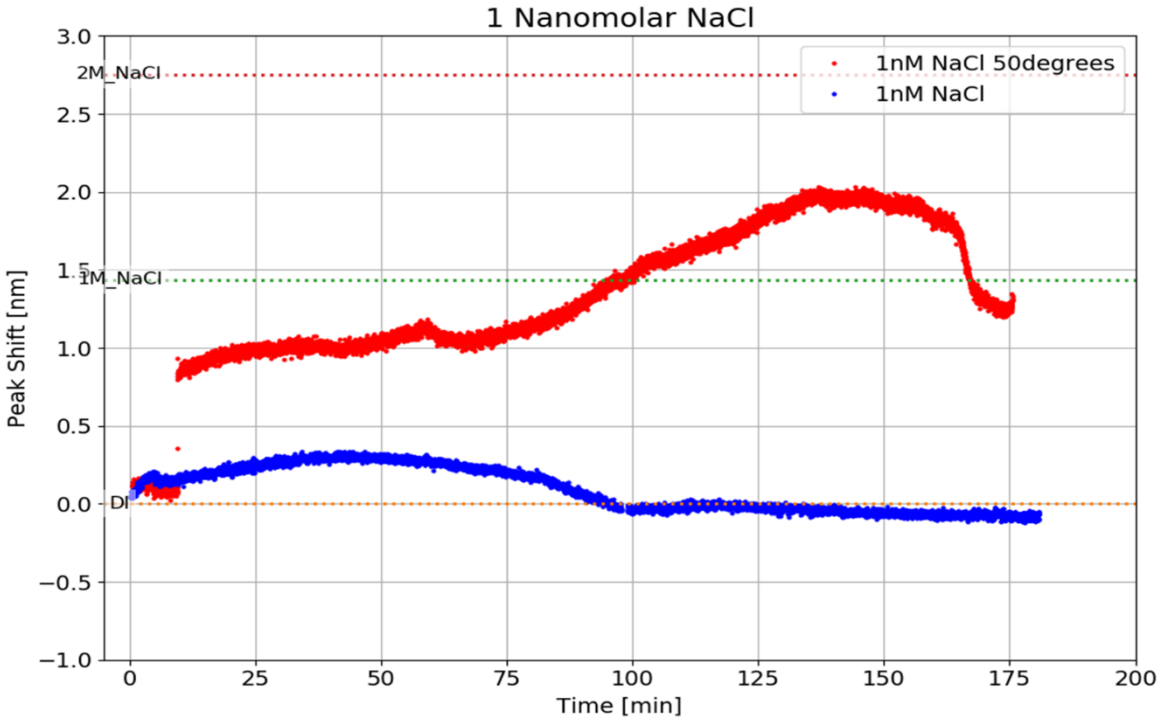

Figure 5.12: *1 nanomolar sodium chloride*

Thermal preconcentration of 1 nanomolar sodium chloride (red) compared with no temperature gradient 1 nanomolar sodium chloride (blue).

One nanomolar of sodium chloride, as shown figure 5.12 in blue, is also undistinguishable from DI water with both a digital refractometer and the nanohole array in our system. Thermal preconcentration at 50˚C produced a measured concentration a factor 10^3 higher than that in the solution. Unlike 1mM the graph shape between 75 and 175 minutes is curved.

The graph shape observed in figure 5.11 between 125 and 200 minutes is more common with this method than the curved shape shown in figure 5.12. The sharp drop in peak shift is believed to be a combination of re-absorption of the analyte and minor fluctuations in heating temperature. The changes in temperature occur due to environment temperature variations, or a decrease in heater output due to a disconnection to the power supply. The curved shape observed in figure 5.12 follows the same overall shape as figure 5.11 but is without these spikes in peak shift. During this measurement it is likely that no variation in temperature output occurred.

Thermal preconcentration measurements with glucose, follow in section 5.4.4.

5.3.7 Glucose

As has already been stated, glucose has a larger molar weight and, in terms of detection, should therefore be easier to detect due to a larger mass available in solution compared to sodium chloride. However, glucose is also a larger analyte which affects the flow through the paper channel. During the drying phase of a measurement, glucose forms a gel-like solution saturating the paper pores and preventing further flow. I used the same experimental setup and procedure as with sodium chloride.

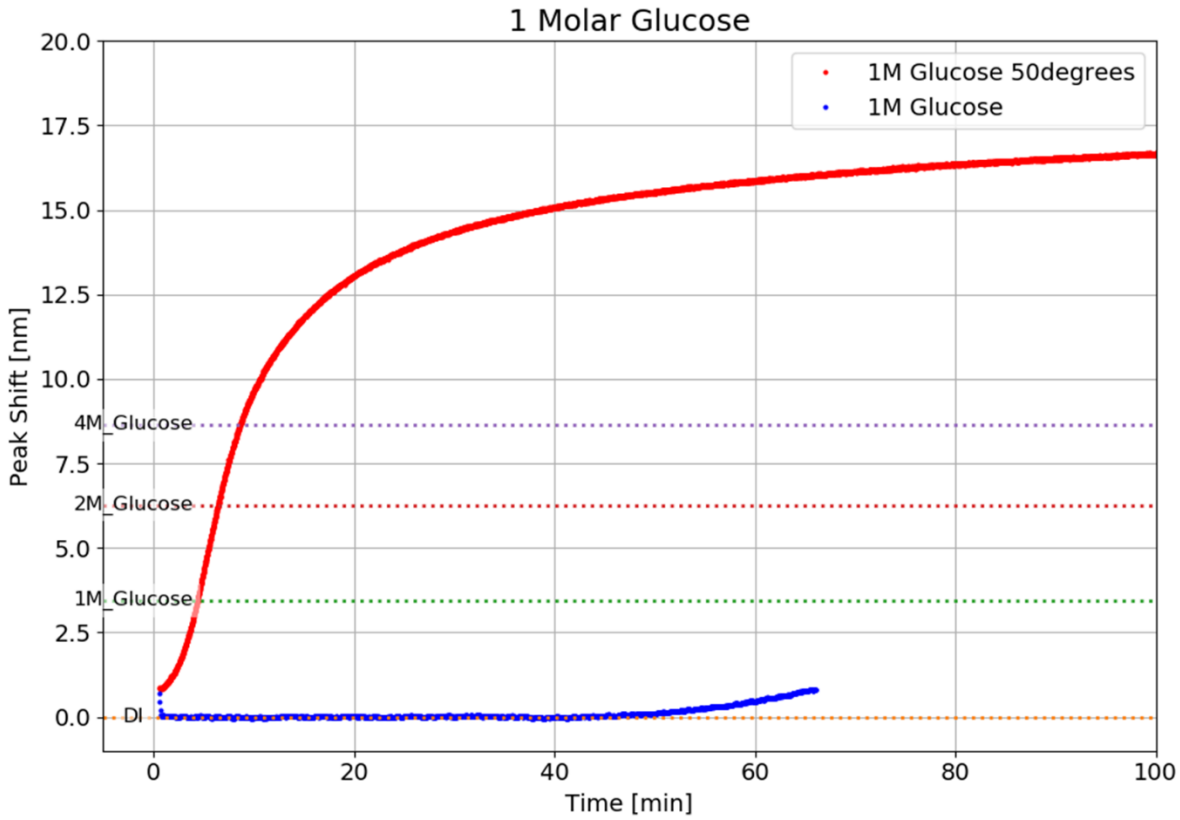

Figure 5.13: *1 molar glucose*

Thermal Preconcentration of 1 molar glucose (red) compared with no temperature gradient 1 molar glucose (blue).

I measured the thermal preconcentration of a one molar glucose solution and compared it to the same solution without the use of the heater, shown figure 5.13. We observe a very strong resonant wavelength shift, indicating that heating achieves a greater analyte concentration. As mentioned above, glucose becomes a thick, gel-like solution when heated and this effect is emphasised with the concentration of glucose within the solution. We observe a shift that appears to show the glucose is beginning to form a crystal-like structure on the surface of the sensor. A “Crystal Glucose” label can be seen in figure 5.13 and occurs at approximately 43nm. Figure 5.13 alone is a good indicator that heating the paper channel has a dramatic effect on the concentration of the analyte. As before, I then moved on to measuring smaller concentrations. 1mM glucose is shown in figure 5.14.

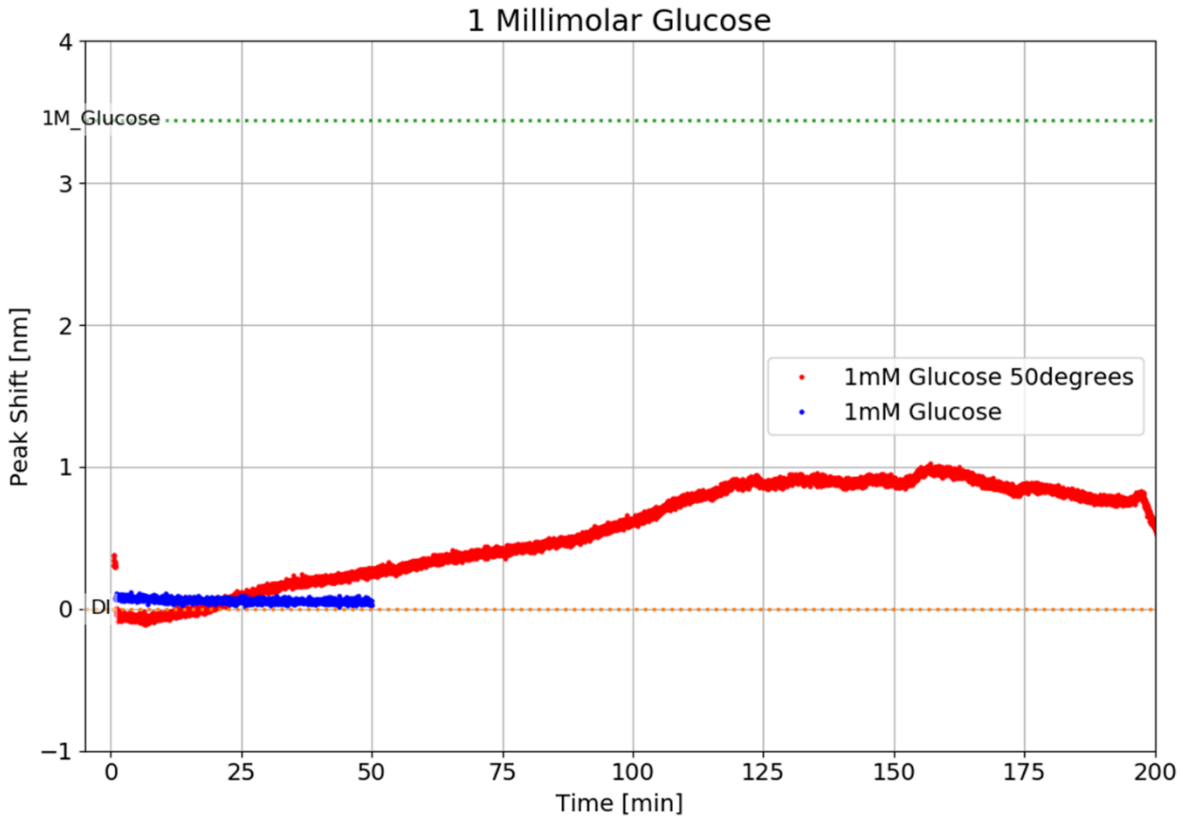

Figure 5.14: *1 millimolar glucose*

Thermal preconcentration of 1 millimolar glucose (red) compared with no temperature gradient 1 millimolar glucose (blue).

As with one millimolar sodium chloride solution (figure 5.11), one millimolar glucose solution is undistinguishable from the DI water in which the glucose is dissolved, with both a digital refractometer and the nanohole array in our system. Thermal preconcentration at 50˚C of 1mM glucose (figure 5.14) produced a measured concentration lower than expected and observed with other solutions. A shift of 1nm is seen in figure 5.14 which, using the sensitivity of the nanohole array (measured as shown in figure 5.8), indicates a detected mass of 15.55mg in 300µL or 0.2 molar glucose solution. 1nM glucose solution is shown in figure 5.15.

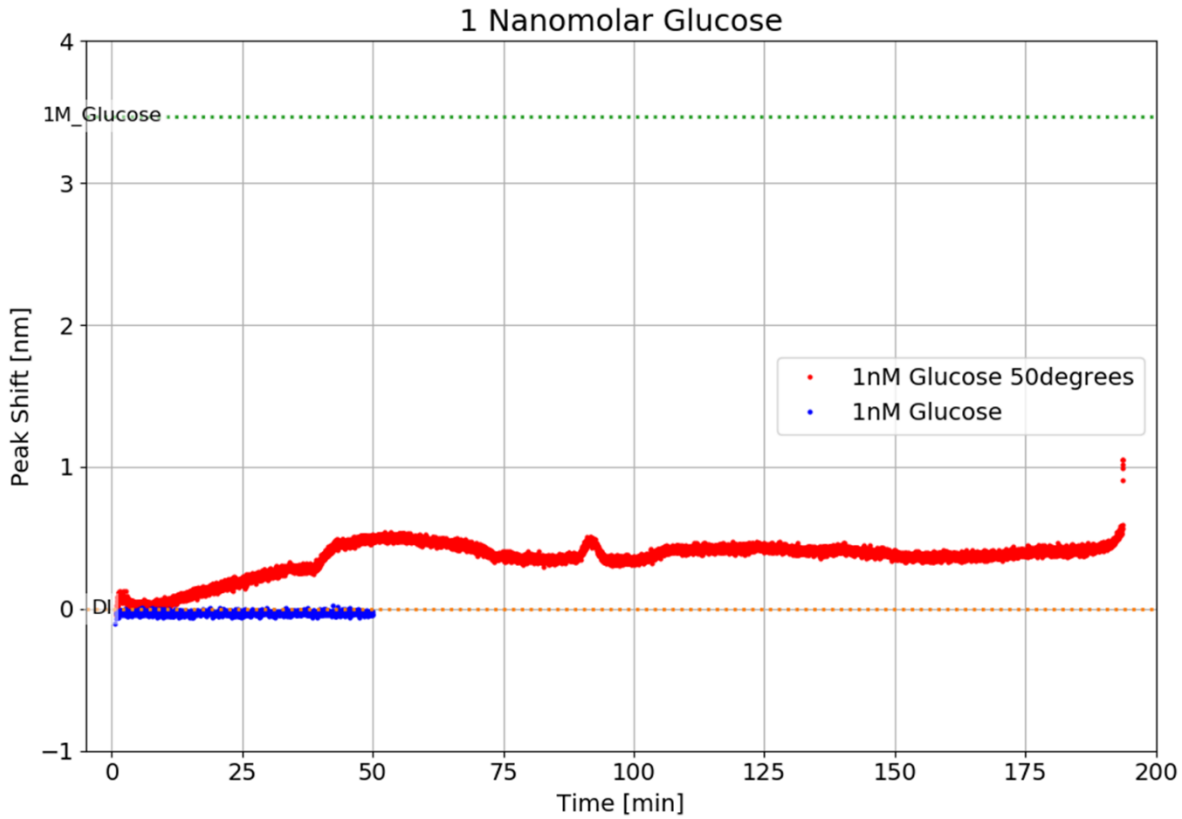

Figure 5.15: *1 nanomolar glucose*

Thermal preconcentration of 1 nanomolar glucose (red) compared with no temperature gradient 1 nanomolar glucose (blue).

Figure 5.15 shows the thermal preconcentration at 50˚C of 1nM glucose solution. As with one millimolar glucose, we see that the un-heater solution is undistinguishable from DI water. We also see that the resonant wavelength shift produced is smaller than expected, which is more common with glucose than with sodium chloride. Like this is due to, as mentioned before, the solution becoming thicker when heated. Using the known sensitivity of the nanohole array, as we did with 1mM glucose, figure 5.15 indicates a detected mass of 7.8mg in 300µL or 0.14 molar glucose solution.

Figure 5.10 to 5.15 represent a selection of thermal preconcentration measurements. There were problems that occurred preventing other concentrations being shown in this work, which are discussed in chapter 6.

5.4 Chapter 5 Conclusion

The first conclusion to draw from chapter 5 is the successful preconcentration of both sodium chloride and glucose solutions shown in figure 5.10-5.15. In every case the resonant wavelength shift measured with a 30 ˚C temperature gradient (50˚C at sensor, 20˚C room temperature) between solution reservoir and sensor was greater than that without a temperature gradient. Above anything else, this shows that our system can reduce the limit of detection of the sensor. The addition of the Kanthal mesh and the location of the heat source drastically improved the thermal preconcentration, which can be seen in figure 5.9. In some instances, a concentration of a factor 10^3 was observed, which had never been possible until the relocation of the heat source.

The concentration measurements are limited by the sensitivity of the sensor, in this case the nanohole array. Any imperfections during the fabrication process or during film deposition (chapter 4 and 3 respectively) or any damage affects the nanohole array quality and its sensitivity. The measurements are also limited by the peak-finding tools, in this instance the Python code used to find the resonant wavelengths. The most accurate method of determining the peak wavelengths would be to individually fit a Fano-shape onto each spectrum to find E_f (equation 5.2). However, this is not a feasible solution due to the time over which measurements are taken and the volume of data that needs to be gathered. The code in this work was benchmarked against commercial graphing software for a random selection of spectrums to ensure it was operating as intended.

The problems that arose with using paper as a solution delivery system were leaking and pore blocking. Firstly, we overcame the leaking problem by adding a reservoir from which the paper can wick (figure 5.5) and only filling the reservoir with a pipette or, for much larger volumes, a pump. Pore blocking only becomes a problem with relatively large analytes, in our case glucose, but other paper substrates can be used. We use chromatography paper almost exclusively and found this to be a good all-round material, in keep with the cheap-and-simple mantra of a POC device.

6. Conclusion and Outlook

To conclude this thesis, this chapter will briefly summarise the results and their meaning and discusses their relevance to future work. A more detailed summary of the results can be found at the end of individual chapters.

6.1 Summary of Achievements

The primary goal of this work was to design and create a cheap and simple point of care device for the purpose of detecting the present of- and measuring the quantity of- analytes in solution. We also proposed that the limit of detection of a sensor can be reduced using a thermal preconcentration.

The first step was to replace the existing PDMS-based microfluidic tubes and pump that are commonplace among point of care devices and microfluidic devices in laboratories. We used the concept of the pregnancy test (and other lateral flow devices), that utilises the capillary force of a porous medium to transfer (and treat with bio-recognition molecules if required) a liquid sample from a drop zone to a detection zone.

A phenomenon known as the coffee-ring effect occurs when a body of water dries, it is responsible for the net outward flow of solutes. To fully maximise the coffee-ring effect we investigated the shape of the paper channel tip and a net thermal gradient between the drop and detection zone on the paper. We found that narrowing the paper to a point, and heating from underneath the sensor allowed for the maximum localisation of any analytes. This result confirms that our system is a potential candidate for a point of care device, although no such device would be useful without a detection sensor.

The sensor we used is a 2D photonic crystal, more commonly known as a nanohole array, consisting of a square array of nanoscale holes in a dielectric. The photonic crystal (PhC) supports leak mode resonance, which allows for energy to be easy coupled to-, resonate in- and couple out of- the periodic structure. The resonant wavelength within the structure is heavily determined by the period, dielectric thickness, hole radius and the refractive index of the cover medium. The PhC measured a refractive index as a resonant wavelength, thus a wavelength shift corresponds to a shift in refractive index. Concentrating analytes can then be measured as a wavelength shift and reported as a refractive index.

To compound the effect of using a 2D periodic structure, as opposed to the regularly used 1D equivalent, we fabricated the nanohole array in a hydrogenated amorphous silicon (a-Si:H) thin film. Adding hydrogen to amorphous silicon is known to reduce the extinction coefficient of amorphous silicon and therefore reduce the energy loss within the medium. Less energy lost during resonance allows for a higher Q-factor grating, and therefore greater sensitivity. Using pulsed DC magnetron sputtering I was able to deposit a-Si:H layers and measure the corresponding optical effect of adding hydrogen. I decided to use a 20% hydrogenated film

(20% of the total gas flow during deposition was hydrogen) due to a lower extinction coefficient and a relatively high refractive index.

Combining the paper channel, heater and nanohole array in a-Si:H, I was then able to measure the thermal preconcentration of sodium chloride solutions and glucose solutions. The experiment involves measuring the resonant wavelength in the photonic crystal in reflection as a function of time, which yields a peak shift vs time. Through proper calibration this quantifies an analyte concentration. The results of these experiments proved the concept and achieved the main goal of this thesis, which is to say that the limit of detection of the photonic crystal can be lowered using a thermal preconcentration making the system a suitable point of care device.

6.2 Context of Results

The limit of detection commonly reported for photonic crystal biosensors, given in the introduction of this thesis, is 10µg/mL. Through thermal preconcentration of both salt and sugar, we have been able to lower this limit of detection to 18ng/mL for glucose and 6ng/mL with sodium chloride. This result corresponds to a factor 10^3 lower limit of detection.

It has not been the primary focus of this thesis so far, but some experiments during this work were performed with an "endless reservoir" created using a microfluidic pump-filled reservoir with the system setup shown in figure 5.6. I measured a millimolar glucose solution, with a reservoir filled at a rate of 300µL per hour. This experiment was performed with the heater above the sensor, to determine if the detection was dependent on analyte mass and therefore could only be increased by sample volume. While we now know this isn't the case, what we can see is that our system is not volume limited in the same way other paper-based LFDs are. The results of this experiment are shown in figure 6.1. After a much longer run time than that shown in figure 5.14, we do observe a thermal preconcentration equivalent to a factor 10^3 increase.

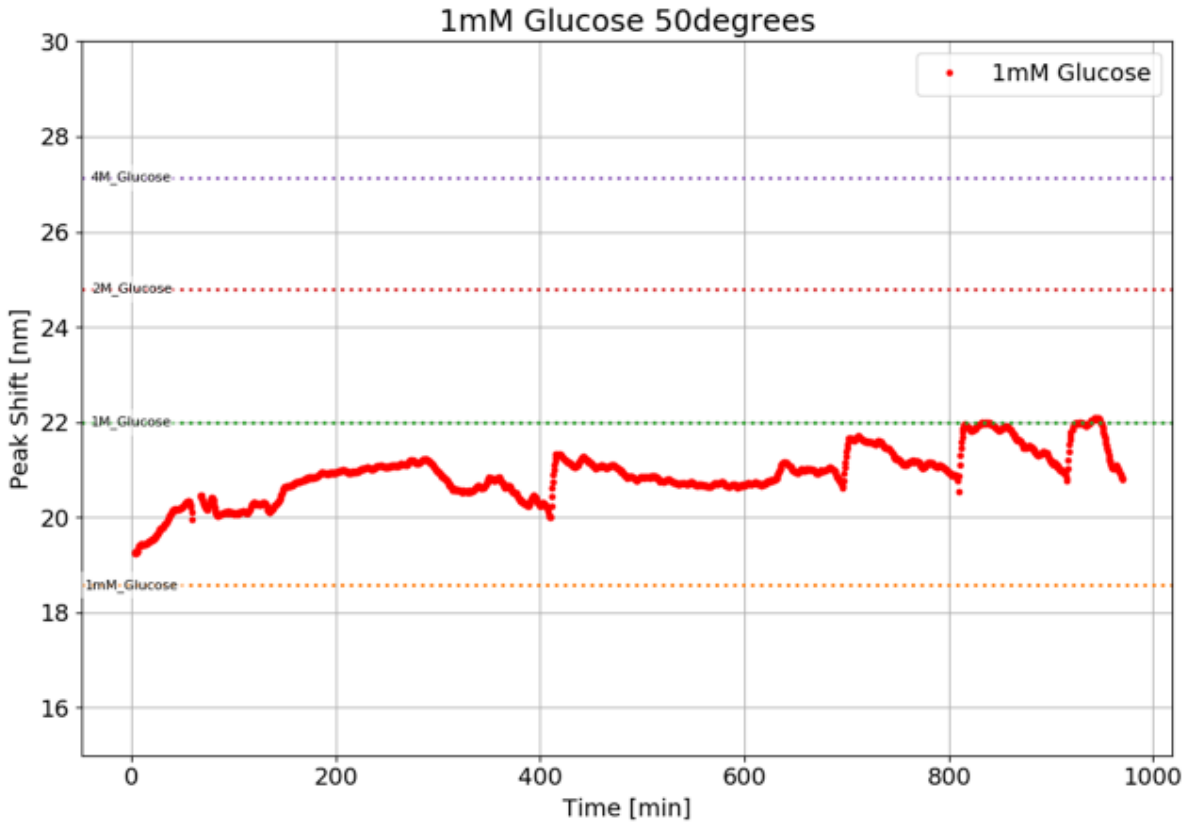

Figure 6.1: *1 millimolar glucose with "endless reservoir"*

Thermal Preconcentration of 1 millimolar glucose (red) with "endless reservoir" topped up at a rate of 300µL per hour with a microfluidic pump.

Sodium is a very important ion in the human body and typically varies in concentration in bodily fluids between 5 and 210 millimolar concentration [105–108]. Sodium concentration is highly regulated within the body, for example a high sodium concentration is related to high blood pressure and cardiovascular disease. Measuring the sodium concentration of bodily fluids is therefore an important task and is prominent among clinical laboratories [108]. Our system presents a cheaper and more portable device for the detection of minor variations in sodium concentration within bodily fluid samples.

Similarly glucose levels in bodily fluids has a clinical application for the detection of diabetes mellitus, an incurable disease resulting from an insufficiency of insulin in the body [109,110] caused by elevated blood-glucose levels. There are a plethora of clinical blood-glucose level monitoring techniques, including Raman and infrared spectroscopy [111]. However, there is a severe lack of devices that can be used daily, by patients to monitor their blood-glucose levels. Glucose levels can be monitored with other bodily fluids such as sweat, saliva and urine [112], which are compatible with our system, presenting a non-invasive method for glucose monitoring. With a portable optical system, an integration with a micro PC (such as a Raspberry Pi) and a battery supply our system would be a suitable POC device for glucose and sodium level monitoring.

6.3 Future Research

As discussed above, and throughout this thesis, our system makes an ideal platform for a cheap and simple to use point of care device. While it outperforms systems such as the pregnancy test and lowers the limit of detection of the photonic crystal sensor, our system has yet to determine the concentration of an analyte within solution from a measured concentration. In other words, our system is still a yes/no diagnostic device just like the pregnancy test. Further work is needed to determine the concentration in solution. The key to determining this could be the time in which a peak shift is achieved. Higher concentrations in solution may be quicker to a refractive index shift than lower concentrations.

The ultimate goal of this work is to achieve a thermal preconcentration of immunoglobulin G, which would allow our system to compete with protein assays. Some preliminary experiments were completed during this project, but unforeseen issues arose with our experimental setup which prevented any useful data being collected. The wash steps required for protein functionalisation require a wash solution to flow over the sensor in relatively large volumes. Using a microfluidic pump to create an "endless reservoir" and an extended region (figure 5.6) to allow for washing, creates a greater potential for solutions to leak out of the paper or to overfill the reservoir. I was not able to complete a successful surface functionalisation and anti-body binding with our system, but this was due human error and not issues with the system. Future work is needed to optimise the anti-body binding protocol with a paper channel.

Integration with a portable version of the optical setup shown figure 5.1, would allow our system to be used as a point of care device for analyte detection and, with calibration on measuring analyte concentration in solution, analyte concentration. Further work is needed to make the optical and processing components of our system portable. Using a paper-based channel gives an advantage in this instance, as the power requirement compared to a PDMS-based microfluidic system is reduced.

Appendix

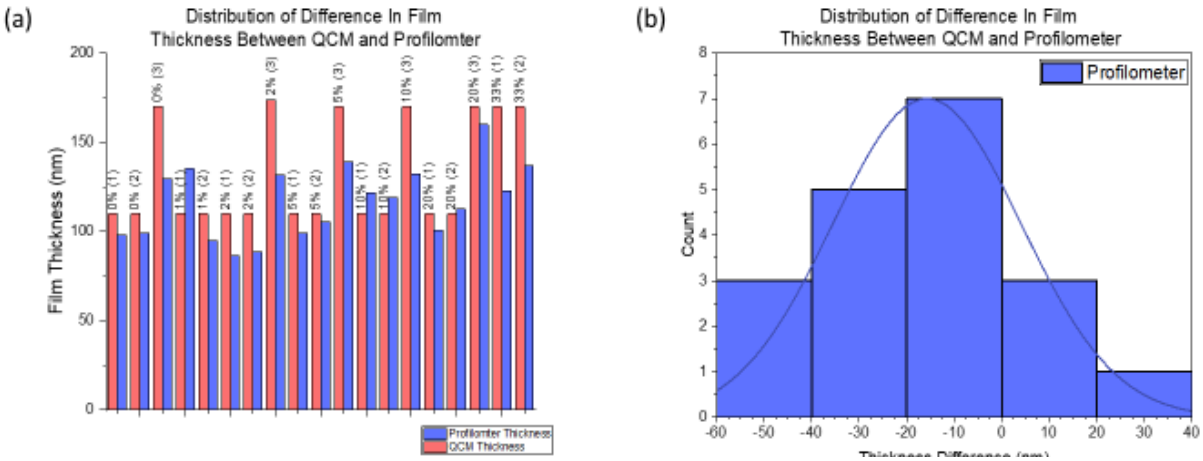

Figure A. 1: *Statistical data for hydrogenated amorphous silicon deposition*

(a) Comparison between QCM and profilometer measured film thickness for a series of hydrogen concentrations within sputtered a-Si:H films. QCM thickness, shown in red, measured during deposition. Profilometer thickness, shown in blue, measured as the step height between substrate and deposited film. Labelled percentage is the hydrogen concentration as a percentage of the total in flow. (b) Histogram showing the frequency distribution of profilometer measured film thickness with respect to the QCM values.

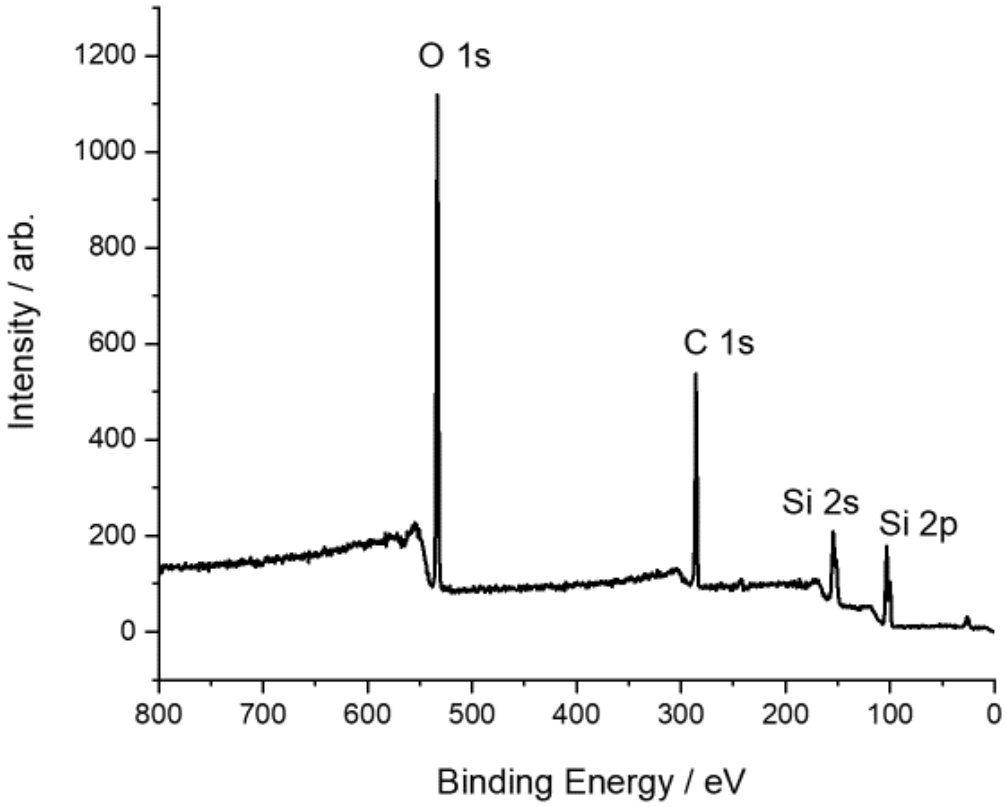

Figure A. 2: *X-ray photoelectron spectroscopy spectrum*

0% hydrogenated a-Si:H sputter-deposited film, showing one clear oxygen peak, two silicon peaks and carbon (noise).

The data was the data

Bibliography

1. Drain, P. K. *et al.* Diagnostic point-of-care tests in resource-limited settings. *The Lancet Infectious Diseases* **14**, 239–249 (2014).
2. Peeling, R. W. & Mabey, D. Point-of-care tests for diagnosing infections in the developing world. *Clinical Microbiology and Infection* **16**, 1062–1069 (2010).
3. Bhunia, A. K., Taitt, C. R. & Kim, M. S. *High Throughput Screening Strategies and Technology Platforms for Detection of Pathogens: An Introduction*. (Woodhead Publishing, 2015).
4. Almeida, M. I. G. S., Jayawardane, B. M., Kolev, S. D. & McKelvie, I. D. Developments of microfluidic paper-based analytical devices (μPADs) for water analysis: A review. *Talanta* **177**, 176–190 (2018).
5. Hansen, C. L., Skordalakes, E., Berger, J. M. & Quake, S. R. A robust and scalable microfluidic metering method that allows protein crystal growth by free interface diffusion. *Proc Natl Acad Sci U S A* **99**, 16531–16536 (2002).
6. Takayama, S. *et al.* Subcellular positioning of small molecules. *Nature* **411**, 1016 (2001).
7. Bange, A., Halsall, H. B. & Heineman, W. R. Microfluidic immunosensor systems. *Biosens Bioelectron* **20**, 2488–2503 (2005).
8. McDonald, J. C. *et al.* Fabrication of microfluidic systems in poly(dimethylsiloxane). *Electrophoresis* **21**, 27–40 (2000).
9. Gale, B. K. *et al.* A Review of Current Methods in Microfluidic Device Fabrication and Future Commercialization Prospects. *Inventions* **3**, 60 (2018).
10. Nielsen, K. *et al.* Development of a lateral flow assay for rapid detection of bovine antibody to Anaplasma marginale. *J Immunoassay Immunochem* **29**, 10–18 (2008).

11. Moreno, M. de L. *et al.* Detection of gluten immunogenic peptides in the urine of patients with coeliac disease reveals transgressions in the gluten-free diet and incomplete mucosal healing. *Gut* **66**, 250–257 (2017).
12. Carrio, A., Sampedro, C., Sanchez-Lopez, J. L., Pimienta, M. & Campoy, P. Automated Low-Cost Smartphone-Based Lateral Flow Saliva Test Reader for Drugs-of-Abuse Detection. *Sensors (Basel)* **15**, 29569–29593 (2015).
13. Schramm, E. C. *et al.* A Quantitative Lateral Flow Assay to Detect Complement Activation in Blood. *Anal Biochem* **477**, 78–85 (2015).
14. Koczula, K. M. & Gallotta, A. Lateral flow assays. *Essays Biochem* **60**, 111–120 (2016).
15. Mahadeva, S. K., Walus, K. & Stoeber, B. Paper as a Platform for Sensing Applications and Other Devices: A Review. *ACS Appl. Mater. Interfaces* **7**, 8345–8362 (2015).
16. McQuade, D. T., Pullen, A. E. & Swager, T. M. Conjugated Polymer-Based Chemical Sensors. *Chem. Rev.* **100**, 2537–2574 (2000).
17. Yuriyama, M. & Kushida, T. Sensor-Cloud Infrastructure - Physical Sensor Management with Virtualized Sensors on Cloud Computing. in *2010 13th International Conference on Network-Based Information Systems* 1–8 (2010). doi:10.1109/NBiS.2010.32.
18. Lenz, J. & Edelstein, S. Magnetic sensors and their applications. *IEEE Sensors Journal* **6**, 631–649 (2006).
19. Cooper, M. A. Optical biosensors in drug discovery. *Nature Reviews Drug Discovery* **1**, 515–528 (2002).
20. Mollenhauer, H. *et al. Adaptive Multichannel Radiation Sensors for Plant Parameter Monitoring*. (2016).
21. Huang, L., Wang, Z., Zhu, X. & Chi, L. Electrical gas sensors based on structured organic ultra-thin films and nanocrystals on solid state substrates. *Nanoscale Horiz.* **1**, 383–393 (2016).

22. Xiao, F., Wang, L. & Duan, H. Nanomaterial based electrochemical sensors for in vitro detection of small molecule metabolites. *Biotechnology Advances* **34**, 234–249 (2016).

23. Gordeliy, V. I. *et al.* Molecular basis of transmembrane signalling by sensory rhodopsin II–transducer complex. *Nature* **419**, 484–487 (2002).

24. *Optical Sensors: Industrial Environmental and Diagnostic Applications*. (Springer-Verlag, 2004).

25. Fan, X. *et al.* Sensitive optical biosensors for unlabeled targets: A review. *Analytica Chimica Acta* **620**, 8–26 (2008).

26. Triggs, G. J. Resonant Grating Surfaces for Biosensing. 142.

27. White, I. M. & Fan, X. On the performance quantification of resonant refractive index sensors. *Opt. Express* **16**, 1020–1028 (2008).

28. Hu, J., Sun, X., Agarwal, A. & Kimerling, L. C. Design guidelines for optical resonator biochemical sensors. *J. Opt. Soc. Am. B* **26**, 1032–1041 (2009).

29. Pal, S., Guillermain, E., Sriram, R., Miller, B. L. & Fauchet, P. M. Silicon photonic crystal nanocavity-coupled waveguides for error-corrected optical biosensing. *Biosens Bioelectron* **26**, 4024–4031 (2011).

30. Pal, S. *et al.* Selective virus detection in complex sample matrices with photonic crystal optical cavities. *Biosens Bioelectron* **44**, 229–234 (2013).

31. Conteduca, D., Romão, R., Martins, E. R. & Krauss, T. F. Enhanced Sensitivity With All-Dielectric Nanoholes Array For Biosensing Applications. in (2019).

32. Deegan, R. D. *et al.* Capillary flow as the cause of ring stains from dried liquid drops. *Nature* **389**, 827–829 (1997).

33. Morrow, N. R. Physics and Thermodynamics of Capillary Action in Porous Media. *Ind. Eng. Chem.* **62**, 32–56 (1970).

34. Philip, J. R. THE THEORY OF INFILTRATION: 4. SORPTIVITY AND ALGEBRAIC INFILTRATION EQUATIONS. *Soil Science* **84**, 257 (1957).
35. Yang, L., Gao, D., Zhang, Y., Tang, J. & Li, Y. Relationship between sorptivity and capillary coefficient for water absorption of cement-based materials: theory analysis and experiment. *Royal Society Open Science* **6**, 190112.
36. Hoseini, M., Bindiganavile, V. & Banthia, N. The effect of mechanical stress on permeability of concrete: A review. *Cement and Concrete Composites* **31**, 213–220 (2009).
37. Steudle, E. The Cohesion-Tension Mechanism and the Acquisition of Water by Plant Roots. *Annual Review of Plant Physiology and Plant Molecular Biology* **52**, 847–875 (2001).
38. Yunker, P. J., Still, T., Lohr, M. A. & Yodh, A. G. Suppression of the coffee-ring effect by shape-dependent capillary interactions. *Nature* **476**, 308–311 (2011).
39. Neurath, Hans., Greenstein, J. P., Putnam, F. W. & Erickson, J. A. The Chemistry of Protein Denaturation. *Chem. Rev.* **34**, 157–265 (1944).
40. Dughaish, Z. H. Lead telluride as a thermoelectric material for thermoelectric power generation. *Physica B: Condensed Matter* **322**, 205–223 (2002).
41. Weber, B. *et al.* Ohm's Law Survives to the Atomic Scale. *Science* **335**, 64 (2012).
42. TIBTECH innovations: Metal properties comparison: electric conductivity, thermal conductivity, density, melting temperature. https://www.tibtech.com/conductivite.php?lang=en_US.
43. Duracell D battery - reliable, long lasting battery. *Duracell* https://www.duracell.co.uk/products/d/.
44. Thermal Conductivity of common Materials and Gases. https://www.engineeringtoolbox.com/thermal-conductivity-d_429.html.

45. Emissivity Coefficients Materials. https://www.engineeringtoolbox.com/emissivity-coefficients-d_447.html.

46. M. Hatzakis, B. J. Canavello & J. M. Shaw. Single-Step Optical Lift-Off Process. *IBM Journal of Research and Development* **24**, 452–460 (1980).

47. Male, J. S., Grant, L., Simmons, M., Reardon, C. P. & Krauss, T. F. Thermally-Induced Pre-Concentration of Analytes in Paper Microfluidics. (2018).

48. Male, J. S., Simmons, M., Reardon, C. P. & Krauss, T. F. Increased Biological Sensitivity and Throughput through Application of Lateral Flow Device Integrated Microheaters. (2018).

49. endeavourmag. The Growing Popularity of Vaping. *Littlegate Publishing* https://www.littlegatepublishing.com/2017/11/the-growing-popularity-of-vaping/ (2017).

50. E-cigarettes: How they work, benefits, and risks. *Medical News Today* https://www.medicalnewstoday.com/articles/216550.php.

51. Zhou, D. W. Heat transfer enhancement of copper nanofluid with acoustic cavitation. *International Journal of Heat and Mass Transfer* **47**, 3109–3117 (2004).

52. Zhao, M.-C., Yang, K. & Shan, Y.-Y. Comparison on strength and toughness behaviors of microalloyed pipeline steels with acicular ferrite and ultrafine ferrite. *Materials Letters* **57**, 1496–1500 (2003).

53. Seo, G. H., Jeun, G. & Kim, S. J. Enhanced pool boiling critical heat flux with a FeCrAl layer fabricated by DC sputtering. *International Journal of Heat and Mass Transfer* **102**, 1293–1307 (2016).

54. Pierce, D. T. & Spicer, W. E. Electronic Structure of Amorphous Si from Photoemission and Optical Studies. *Phys. Rev. B* **5**, 3017–3029 (1972).

55. Philipp, H. R. Optical Properties of Silicon Nitride. *J. Electrochem. Soc.* **120**, 295–300 (1973).

56. Eranna, G. *Crystal Growth and Evaluation of Silicon for VLSI and ULSI*. (CRC Press, 2014).

57. Mavračić, J., Mocanu, F. C., Deringer, V. L., Csányi, G. & Elliott, S. R. Similarity Between Amorphous and Crystalline Phases: The Case of TiO2. *J. Phys. Chem. Lett.* **9**, 2985–2990 (2018).

58. Zhou, L. *et al.* Defect-free Fabrication for Single Crystal Silicon Substrate by Chemo-Mechanical Grinding. *CIRP Annals* **55**, 313–316 (2006).

59. Street, R. A. *Hydrogenated Amorphous Silicon*. (Cambridge University Press, 2005).

60. de Sousa, R. Dangling-bond spin relaxation and magnetic $1/f$ noise from the amorphous-semiconductor/oxide interface: Theory. *Phys. Rev. B* **76**, 245306 (2007).

61. Franco Gaspari ED1 - Padmanabhan Predeep. Optoelectronic Properties of Amorphous Silicon the Role of Hydrogen: from Experiment to Modeling. in *Optoelectronics* Ch. 1 (IntechOpen, 2011). doi:10.5772/18255.

62. Schuster, C. S. *Diffractive Optics for Thin-Film Silicon Solar Cells*. (Springer International Publishing, 2017). doi:10.1007/978-3-319-44278-5.

63. Swanepoel, R. Determination of the thickness and optical constants of amorphous silicon. *J. Phys. E: Sci. Instrum.* **16**, 1214–1222 (1983).

64. DeVoe, H. Optical Properties of Molecular Aggregates. II. Classical Theory of the Refraction, Absorption, and Optical Activity of Solutions and Crystals. *J. Chem. Phys.* **43**, 3199–3208 (1965).

65. Choy, K. L. Chemical vapour deposition of coatings. *Progress in Materials Science* **48**, 57–170 (2003).

66. Mahan, J. E. *Physical Vapor Deposition of Thin Films*. (2000).

67. Stoffel, A., Kovács, A., Kronast, W. & Müller, B. LPCVD against PECVD for micromechanical applications. *Journal of Micromechanics and Microengineering* **6**, 1–13 (1996).

68. Chandra, H., George, M. A. & Madocks, J. Low temperature plasma chemical vapor deposition (PCVD) of fluorinated tin-oxide transparent conducting oxide. in *2009 34th IEEE Photovoltaic Specialists Conference (PVSC)* 001519–001522 (2009). doi:10.1109/PVSC.2009.5411348.

69. Emeléus, H. J. & Stewart, K. 281. The oxidation of the silicon hydrides. Part I. *J. Chem. Soc*. 1182–1189 (1935) doi:10.1039/JR9350001182.

70. Kelly, P. J. & Arnell, R. D. Magnetron sputtering: a review of recent developments and applications. *Vacuum* **56**, 159–172 (2000).

71. Safi, I. Recent aspects concerning DC reactive magnetron sputtering of thin films: a review. *Surface and Coatings Technology* **127**, 203–218 (2000).

72. Karthikeyan, S., Hill, A. E., Cowpe, J. S. & Pilkington, R. D. The influence of operating parameters on pulsed D.C. magnetron sputtering plasma. *Vacuum* **85**, 634–638 (2010).

73. Bruckenstein, S. & Shay, M. Experimental aspects of use of the quartz crystal microbalance in solution. *Electrochimica Acta* **30**, 1295–1300 (1985).

74. Huang, X., Bai, Q., Hu, J. & Hou, D. A Practical Model of Quartz Crystal Microbalance in Actual Applications. *Sensors (Basel)* **17**, 1785 (2017).

75. Duncan, W. M. & Henck, S. A. Insitu spectral ellipsometry for real-time measurement and control. *Applied Surface Science* **63**, 9–16 (1993).

76. Li, J. & Wu, S.-T. Two-coefficient Cauchy model for low birefringence liquid crystals. *Journal of Applied Physics* **96**, 170–174 (2004).

77. Toll, J. S. Causality and the Dispersion Relation: Logical Foundations. *Phys. Rev.* **104**, 1760–1770 (1956).

78. Biesinger, M. C., Brown, C., Mycroft, J. R., Davidson, R. D. & McIntyre, N. S. X-ray photoelectron spectroscopy studies of chromium compounds. *Surface and Interface Analysis* **36**, 1550–1563 (2004).

79. Malitson, I. H. Interspecimen Comparison of the Refractive Index of Fused Silica$\ast$,†. *J. Opt. Soc. Am.* **55**, 1205–1209 (1965).

80. Hoffman, D. W. & Thornton, J. A. Internal stresses in Cr, Mo, Ta, and Pt films deposited by sputtering from a planar magnetron source. *Journal of Vacuum Science and Technology* **20**, 355–358 (1982).

81. Lin, B. *et al.* A label-free optical technique for detecting small molecule interactions. *Biosensors and Bioelectronics* **17**, 827–834 (2002).

82. Cunningham, B., Li, P., Lin, B. & Pepper, J. Colorimetric resonant reflection as a direct biochemical assay technique. *Sensors and Actuators B: Chemical* **81**, 316–328 (2002).

83. Cunningham, B. *et al.* A plastic colorimetric resonant optical biosensor for multiparallel detection of label-free biochemical interactions. *Sensors and Actuators B: Chemical* **85**, 219–226 (2002).

84. Cunningham, B. T. *et al.* Label-free assays on the BIND system. *J Biomol Screen* **9**, 481–490 (2004).

85. Chou, S. Y., Krauss, P. R. & Renstrom, P. J. Nanoimprint lithography. *Journal of Vacuum Science & Technology B: Microelectronics and Nanometer Structures Processing, Measurement, and Phenomena* **14**, 4129–4133 (1996).

86. *Photonic crystals: molding the flow of light*. (Princeton University Press, 2008).

87. Mutlu, M., Akosman, A., Kurt, G., Gokkavas, M. & Ozbay, E. Experimental realization of a high-contrast grating based broadband quarter-wave plate. *Optics express* **20**, 27966–73 (2012).

88. Snyder, A. W. & Love, J. Introduction to Part I. in *Optical Waveguide Theory* 3–5 (Springer US, 1983). doi:10.1007/978-1-4613-2813-1.

89. Pitruzzello, G. & Krauss, T. F. Photonic crystal resonances for sensing and imaging. *J. Opt.* **20**, 073004 (2018).

90. Germany, A. G.-S. ALLRESIST GmbH - Strausberg, Germany. *Allresist EN* https://www.allresist.com/csar-62-ar-p-6200/ (2014).

91. Germany, A. G.-S. ALLRESIST GmbH - Strausberg, Germany. *Allresist EN* https://www.allresist.com/ar-pc-5090-5091-electra-92/ (2016).

92. A. A. Tseng, Kuan Chen, C. D. Chen & K. J. Ma. Electron beam lithography in nanoscale fabrication: recent development. *IEEE Transactions on Electronics Packaging Manufacturing* **26**, 141–149 (2003).

93. MICROPOSIT™ REMOVER 1165. *Semiconductor Technologies* 3.

94. Goldstein, J. I. *et al.* Chapter 1. Electron Beam - Specimen Interactions: Interaction Volume. in *Scanning Electron Microscopy and X-Ray Microanalysis* (Springer-Verlag, 2018). doi:10.1007/978-1-4939-6676-9.

95. Yu, P. *et al.* Fano resonances in ultracompact waveguide Fabry-Perot resonator side-coupled lossy nanobeam cavities. *Appl. Phys. Lett.* **103**, 091104 (2013).

96. Mellon, E. A. *et al.* Sodium MR Imaging Detection of Mild Alzheimer Disease: Preliminary Study. *AJNR Am J Neuroradiol* **30**, 978–984 (2009).

97. Jamnongwong, M., Loubiere, K., Dietrich, N. & Hébrard, G. Experimental study of oxygen diffusion coefficients in clean water containing salt, glucose or surfactant: Consequences on the liquid-side mass transfer coefficients. *Chemical Engineering Journal* **165**, 758–768 (2010).

98. Temperature dependence analysis of the thermo-optic effect in silicon by single and double oscillator models: Journal of Applied Physics: Vol 88, No 12. https://aip.scitation.org/doi/10.1063/1.1328062.

99. Komma, J., Schwarz, C., Hofmann, G., Heinert, D. & Nawrodt, R. Thermo-optic coefficient of silicon at 1550 nm and cryogenic temperatures. *Appl. Phys. Lett.* **101**, 041905 (2012).

100. Cocorullo, G., Della Corte, F. G., Rendina, I. & Sarro, P. M. Thermo-optic effect exploitation in silicon microstructures. *Sensors and Actuators A: Physical* **71**, 19–26 (1998).

101. Iodice, M., Mazzi, G. & Sirleto, L. Thermo-optical static and dynamic analysis of a digital optical switch based on amorphous silicon waveguide. *Opt. Express* **14**, 5266 (2006).

102. Zhang, Z. *et al.* A new material platform of Si photonics for implementing architecture of dense wavelength division multiplexing on Si bulk wafer. *Science and Technology of Advanced Materials* **18**, 283–293 (2017).

103. Wild, B. *et al.* Temperature tuning of the optical properties of planar photonic crystal microcavities. *Appl. Phys. Lett.* **84**, 846–848 (2004).

104. Thiery, J. Water Transfers in Sub-Micron Porous Media during Drying and Imbibition Transferts d'eau en milieux nano-poreux durant le séchage et l'imbibition. 166.

105. Ver Heyen, K. *et al.* Synthesis and characterisation of new fluorescent Na+ and K+ indicators. *Tetrahedron* **55**, 5207–5226 (1999).

106. Metzger, E., Ammann, D., Asper, R. & Simon, W. Ion selective liquid membrane electrode for the assay of lithium in blood serum. *Anal. Chem.* **58**, 132–135 (1986).

107. McCarron, D. A., Kazaks, A. G., Geerling, J. C., Stern, J. S. & Graudal, N. A. Response to 'Salt: the dying echoes of the food industry'. *Am. J. Hypertens.* **27**, 282–284 (2014).

108. Gao, G. *et al.* Fluorescent sensors for sodium ions. *Anal. Methods* **9**, 5570–5579 (2017).

109. Sjöqvist, F., Bergman, U., Dahl, M.-L., Gustafsson, L. L. & Hensjö, L.-O. Drug and Therapeutics committees:a Swedish experience. in (2002).

110. American Diabetes Association. Diagnosis and classification of diabetes mellitus. *Diabetes Care* **27 Suppl 1**, S5–S10 (2004).

111. Yadav, J., Rani, A., Singh, V. & Murari, B. M. Prospects and limitations of non-invasive blood glucose monitoring using near-infrared spectroscopy. *Biomedical Signal Processing and Control* **18**, 214–227 (2015).

112. Bruen, D., Delaney, C., Florea, L. & Diamond, D. Glucose Sensing for Diabetes Monitoring: Recent Developments. *Sensors (Basel)* **17**, (2017).